BEAM STEERING USING MICROLENS ARRAYS

by

Ahmet Ata Akatay

A Thesis Submitted to the
Graduate School of Engineering
in Partial Fulfillment of the Requirements for
the Degree of

Master of Science
in
Electrical and Computer Engineering

Koc University

December 2006

Koc University

Graduate School of Sciences and Engineering

This is to certify that I have examined this copy of a master's thesis by

Ahmet Ata Akatay

and have found that it is complete and satisfactory in all respects,

and that any and all revisions required by the final

examining committee have been made.

Committee Members:

____

Hakan Urey, Ph. D. (Advisor)

____

Irsadi Aksun, Ph. D.

____

Alper Kiraz, Ph. D.

Date: ________________________

ABSTRACT

Laser scanners are enabling key technologies and have wide spread applications in displays, imaging/detection systems and information technologies. The most common beam steering systems operate by reflection from a torsionally scanning mirror, or refraction at a displaced lens system, or by phase modulation. In this work, a new laser scanning system based on lateral displacements of microlens arrays (MLA) is designed and demonstrated. In the system, the beam is steered by refraction at multiple microlenses. The main advantages of the proposed scheme are the compactness and the high-resolution offered by small deflections of the mechanical actuator. MLA scanners were proposed in the literature; however, only discrete scan angles were addressable due to diffraction effects and the resolution of the scheme was limited. One of the main contributions of this thesis is the solution offered for the discrete addressing problem by way of introducing an additional moving microlens or linear phase modulator into the system, identified as a prescan lens.

A ray tracing based optimization scheme for design of telescopic array systems is developed. The scheme considers both the aberrations and the diffraction of beamlets array at the far-field. Ray tracing modalities of the commercial optical design tool, ZEMAX^{TM}, combined with a physical optics propagator; and full MLA scanner system simulation is demonstrated. The optical system utilizing aspherical MLAs is optimized and high resolution (>1500×1500 with a 2 mm clear aperture) diffraction limited beam steering is simulated.

In addition, different fabrication methods for 100% fill-factor MLAs are experimentally evaluated. Operation of the beam steering system is demonstrated using electromagnetic stages at modest scan speeds. Resolution of 180 is obtained using slow spherical MLAs. If MLAs are integrated with micro-electro-mechanical (MEMS) moving stages, high speed

scanning and data acquisition is possible. The proposed scheme is particularly well-suited for forward-looking endoscopic imaging applications, where the optics and the actuator have to fit in a small tube of diameter 5mm, scanning laser-Doppler-vibrometry, and for applications where a large clear aperture and fast actuation is needed such as in infrared target detection and tracking applications.

Keywords: Microoptics, beam steering, endoscopic imaging, diffraction, optical design, Fourier optics, microfabrication

ÖZET

Lazer tarayıcılar, ekran, görüntüleme ve bilgi sistemleri teknolojileri gibi bir çok uygulamaları olan kritik teknolojilerdir. Çoğu lazer tarayıcılar, yansıma, kırılma veya faz değişikliği oluşturarak çalışır. Bu çalışmada, mikrolens dizinlerinin (MLD) yatay hareketleriyle çalışan yeni bir lazer tarama sistemi tasarlanmış ve gösterilmiştir. Bu sistemde ışınlar bir çok mikrolens tarafından kırılarak gezdirilmektedir. Öne sürülmüş sistemin temel avantajları, ufak sistem yapısı ve ufak mekanik hareketlerle yüksek piksel sayısı elde edebilmesidir. MLD ile ışın gezdirilmesi daha önce önerilmiştir, fakat, girişim etkilerinden dolayı kesikli tarama yapılabilmesinden dolayı piksel sayısı sınırlı kalmıştır. Bu tezin temel katkılardan biri, kesikli adresleme sorununa, ön-tarayıcı lens diye adlandırılan ek hareketli bir lensin eklenmesiyle bulduğu çözümdür.

Bu yeni tarama sisteminin, optik tasarımı ve performansının eniyilenmesi için, bir modelleme ve simulasyon metodu geliştirilmiştir. Metod, fiziksel optik simulasyon metodlarını ve ticari bir ışın simulatörü ZEMAX^{TM} kullanmaktadır. Metod, sistemin hem sapınç (aberration), hem de girişim performanslarını göz önüne alarak, ZEMAX'in eniyileme işlevini kullanarak sistem performansını eniyiler.

Ek olarak, %100 dolu (fill-factor) MLD'lerin farklı üretim teknikleri deneysel olarak çalışıldı. Işın tarama sisteminin çalışma tekniği, elektromagnetik etkilerle hareket eden platformlar kullanılarak düşük hızlarda gösterildi. Eğer MLD'ler mikro-elektro-mekanik hareketli sistemlerle entegre edilirse, yüksek tarama hızları ve bilgi aktarımı elde edilebilir. Önerilen sistem, endoskobik görüntüleme uygulamalarına, taramalı lazer Doppler titreşim ölçer cihazlarına ve kızılötesi hedef tespiti/takibi gibi büyük ışın genişliği gereken tarama uygulamalarına özellikle uygun görülmektedir.

Anahtar Kelimeler: Mikro-optik, ışın tarama, endoskobik görüntüleme, girişim, optik tasarim, Fourier optik, mikrofabrikasyon

ACKNOWLEDGEMENTS

Above all, I would like to express my sincere appreciation to my thesis advisor Prof. Hakan Ürey for his belief in me. Introducing me to micro-optics and microsystems, the experience and knowledge he offered me is beyond from this thesis. Together with him I would like to thank Prof. Mo Taghizadeh from Heriot-Watt University, Edinburgh, allowing me to spend 2 months with his research group for fabrication microlens arrays. He was very helpful and motivating.

I also would like to thank Prof. Irsadi Aksun and Dr. Alper Kiraz for taking part in my thesis jury.

The most enjoyable part of being a member of OML was to work with Arda, Çağlar, Fatih and Serhan. This work would not be complete without their friendship and support. I want to particularly thank to Çağlar for being a helpful projectmate throughout the project.

Many thanks go to Andrew, Neil, Himanshu, and Martin for both helping me in cleanroom and helping me to get used to Edinburgh. Particularly, I would like to thank Neil for spending long hours in the cleanroom with me. I also want to acknowledge Mary for her help during my stay in Edinburgh.

It is certain that this thesis would be impossible without the emotional support and understanding from my family. Especially I owe much thanks to my brother Burak who let me access his workstation remotely for carrying out part of the simulations.

TABLE OF CONTENTS

LIST OF TABLES IX

LIST OF FIGURES X

NOMENCLATURE XIV

CHAPTER 1 1

INTRODUCTION 1

1.1. Literature review 2
1.1.1. Beam steering using microlens arrays (MLAs) 2

CHAPTER 2 5

BEAM STEERING USING MLAS 5

2.1. Introduction 5
2.2. Continuous scanning 5
2.3. Analytical formulation 9
2.3.1. Fourier optics analysis 9
2.3.2. Beam propagation through the three microlens channel 12
2.3.3. Lens displacement 17
2.3.4. Oblique beam incidence 18
2.3.5. Point spread function (PSF) of the system 19
2.4. Numerical demonstration 23
2.4.1. Far-Field Propagation (FFP) 25
2.4.2. Limits of the Fresnel Propagation 28
2.4.3. Plane Wave Propagation (PWP) 29
2.4.4. Simulation Results 31
2.5. Experimental verification 33

CHAPTER 3 35

OPTICAL SYSTEM DESIGN 35

3.1. Introduction 35
3.2. Resolution analysis 36
3.3. Array fill-factor and diffraction analysis 38
3.4. Optimization of the optical system 45

3.4.1. The PSF of the aberrated system ... 45
3.4.2. Optical performance analysis ... 47
3.4.3. Simulation and optimization of the system ... 48
3.5. The experimental setup ... 52
3.6. Microlens array fabrication ... 59
3.6.1. Isotropic etching method ... 60
3.6.2. Diffractive lens fabrication method ... 63
3.6.3. Reflow method ... 64
3.6.4. Hybrid method ... 67
3.6.5. Laser writing method ... 68
CHAPTER 4 ... 71
SYSTEM IMPLEMENTATION AND OPERATION ... 71
4.1. Continuous addressing ... 71
4.1.1. PSL implementation ... 71
4.1.2. Liquid crystal (LC) implementation ... 73
4.2. Monochromatic imaging ... 75
4.3. Temporally incoherent imaging ... 79
4.4. Spatially incoherent imaging ... 84
CHAPTER 5 ... 87
COMPARATIVE ANALYSIS AND APPLICATIONS OF MLA SCANNERS ... 87
5.1. Comparative analysis of MLA scanners ... 87
5.1.1. Scanning by liquid crystal (LC) phased arrays ... 89
5.1.2. Continuous Line Addressing with MLA Scanners ... 93
5.1.3. MLA Scanning System Comparison with Phased-Array and Mechanical Scanners 94
5.2. MLA scanner applications ... 98
5.2.1. Endoscopic imaging ... 98
5.2.2. Infrared countermeasure (IRCM) ... 101
5.2.3. Scanning laser Doppler vibrometer (SLDV) ... 102
CHAPTER 6 ... 104
CONCLUSIONS ... 104
REFERENCES: ... 106

LIST OF TABLES

Table 2.1: The numerical simulation parameters and system geometry values 25
Table 3.1: MLA beam steering system parameters and the system resolution.*................. 37
Table 6.1: Comparison of the proposed system with a recent endoscope technology developed by Olympus 105

LIST OF FIGURES

Figure 1.1: Three lens system for beam steering [4] 3
Figure 1.2: Microlens array beam steering system using three MLAs................................ 4
Figure 1.3: Representation of the lateral MEMS actuation for MLA beam scanners 4

Figure 2.1: System geometry and steering of light by displacements of the PSL and MMLA. D: clear aperture size; d: microlens diameter; f_{PSL}: PSL focal length; f_{MLA}: MLA focal length; and r_1 and r_2 are PSL and MMLA displacements.......................... 6
Figure 2.2: Propagation of the beamlets through the three-microlens system, represented for when (a) L1 is displaced by r_1 (b) the incident beam is tilted with angle $-\alpha$, and (c) combination of (a) and (b) 7
Figure 2.3: Physical optics view of the 3-MLA block system after the PSL. Scan angle and OPD between beam segments is marked after each element. (Dummy phase shifters have no net effect in the system).. 8
Figure 2.4: Representation of the Huygens-Fresnel principle showing integration of the beams emanating from the aperture plane and incident on the output plane.............. 11
Figure 2.5: Representation of propagation through the three microlens system. Propagation through the system is represented as two consecutive Fourier operations. 13
Figure 2.6: Representation of the periodic and envelope Sinc functions which forms the PSF 21
Figure 2.7: Contributions of the PSL and MMLA to the scan angle and inter-channel OPD at the output.. 21
Figure 2.8: Simulation of the system using different simulation methods. 23
Figure 2.9: Simulated PSF for different amounts of the PSL and the MMLA displacements (r_1 and r_2) and the resultant beam tilt angles α and β. (a), (c), and (d) illustrate constructive beam interference (phase condition is met) and (b) illustrate destructive interference (phase condition is not met)... 32
Figure 2.10: Experimental results for the MMLA and the PSL's motion. (a) All lenses on-axis, (b) Only the MMLA is moved to steer beam by half diffraction angle (phase condition not met); (c) Both the PSL and the MMLA is moved to steer the beam by half diffraction angle (phase condition met);.. 34

Figure 3.1: Simulated laser beam steering system for diffractive performance evaluation (MLAs are identical and the focusing lens is an ideal Fourier lens) 38
Figure 3.2: Lens Phase functions and corresponding PSF figures of refractive lenses with (i) no-optical elements (ii) circular shaped MLAs (%78 fill-factor), (iii) perfect fill-factor (%100), (iv) spaced (%93 fill-factor), (v) hybrid-diffractive (%100) [f : 6]..... 40

Figure 3.3: Imaging performances of the lenses are compared 42
Figure 3.4: Sections of an f / 6 lens designed in 16-8-4-2 phase levels by considering 1 m resolution limited fabrication process 43
Figure 3.5: Diffraction efficiency vs. f# for circular 16-phase-level diffractive lenses....... 43
Figure 3.6: Wavelength depended performances of fully- and hybrid-diffractive MLAs in beam steering system 44
Figure 3.7: Illustration of the PSF formulated by periodical Sinc functions (I_2) multiplied by an envelope function (I_1).. 46
Figure 3.8: 3D schematic view of the simulated system utilizing f/2 MLAs. 49
Figure 3.9: Wavefront aberrations plotted in x and y directions for the systems utilizing 100 µm pitched (a) aspherical f/2 (b) aspherical f/5 (c) spherical f/2 (d) spherical f/5 MLAs. 50
Figure 3.10: PSF cross-sections of the systems for (a) aspherical f/2 at the center position (b) aspherical f/2 at the max. scan angle position (c) spherical f/2 at the center position (d) spherical f/2 at the center position ($\theta_d=\lambda/d$) 51
Figure 3.11: MTF plots for the systems of various configurations.................................... 52
Figure 3.12: Profile of the MLAs used in the experiments. Plot of surface profile compared with the spherical profile and 3-D surface profile graph 54
Figure 3.13: MLA laser scanning setup 55
Figure 3.14: The CD-ROM optical pick-up assembly that is modified and used in the setup. 55
Figure 3.15: Simulated reference pattern used for alignment of the two MLAs which constitute the DMLA, i.e., far-field pattern after the DMLA. The sharpness and distribution of the diffraction orders (i.e. spots) are measures for evaluation of 6-axis alignment of two identical MLAs separated at a focal distance 56
Figure 3.16: Experimental results of the line scans. (a) The MMLA motion only produces discrete addressing; (b) The PSL and the MMLA move synchronously and phase condition is met at all times and continuous addressing is achieved (c) PSFs at five consecutive diffraction orders.. 57
Figure 3.17: PSFs at different scan positions. Illustrates resolution of the system. Different magnitudes of the peaks are due to sinusoidally varying scanning speed across the scan line 58
Figure 3.18: Fabrication process of the silicon mold structure... 61
Figure 3.19: Process flow of casting from the mold structure 62
Figure 3.20: Photoresist masked gold plated silicon structure for etching of silicon though an array of holes on a masking gold layer 62
Figure 3.21: Design of multi-level diffractive lenses [39]... 64
Figure 3.22: Two mask fabrication process of a 4-level diffractive lens............................ 64
Figure 3.23: Process flow for reflow fabrication method 66

Figure 3.24: Profile of the reflowed lenses compared to the perfect spherical profile........ 66
Figure 3.25: Microscope image of the reflowed square-shaped MLAs and focused spot image of that MLA... 67
Figure 3.26: Fabrication of the diffractive lenses and hybrid lenses 68
Figure 3.27:Through focus plot of the hybrid lens. Demonstrates focal distance match of diffractive and refractive lenses 68
Figure 3.28: Scanning of the laser spot across the PR spinned substrate [45].................... 69
Figure 3.29: Maskless laser scanning writing setup for fabrication of MLAs.................... 70

Figure 4.1: Driving scheme for continuous addressing. Plots show PSL and MMLA displacement values in terms of introduced steering angles α and β. 72
Figure 4.2: Actuation of the PSL and MMLA for scanning a full line............................... 73
Figure 4.3: Driving scheme for continuous addressing. Plots show LC implemented PSL and MMLA displacement values in terms of introduced steering angles α and β. 74
Figure 4.4: The resulted scan angle θ when the actuation given in Figure 4.3 is applied ... 75
Figure 4.5: 2-D spot of the system for $\phi_{im,x}\neq0$, $\phi_{im,y}=0$ 77
Figure 4.6 Illustration of the Sinc functions used for PSF analysis.................................... 78
Figure 4.7 Representation of diffraction lobes appear in the PSF 78
Figure 4.8: Modeling of the narrowband imaging system ($m_{im}\Delta\lambda_{im} << \lambda_{im}$)..................... 83
Figure 4.9: Positions of spectral components on the imaging plane. Illustrates folding of the spectrum according to (4.5) ($\lambda_{sc}=1.2\lambda_{im}$, $m_{sc}=20$).. 84
Figure 4.10: PSF_{im} of the imaging system for (a) spatially and temporally coherent sources (i.e., lasers); (b) spatially coherent; temporally incoherent (narrowband) sources i.e., laser diodes); (c) spatially incoherent (extended) and temporally coherent sources (e.g., filtered LED or narrowband fluorescence); (d) - (e) on-axis and off-axis fluorescence or LED ($m_{im}\Delta\lambda_{im} << \lambda_{im}$) 86

Figure 5.1: Illustrated scanning by an LC scanner [63].. 88
Figure 5.2: Various types of mechanical scanners [55].. 88
Figure 5.3: Multi-level diffraction grating approximation to a linear phase function programmed on the LC element pixels... 90
Figure 5.4: Illustrated comparison of the desired phase function and the LC phase function which suffers fringing fields at the reset position [63] 91
Figure 5.5: Illustration of blazed angle beam steering.. 92
Figure 5.6: Phase profile for two steering angles. Illustrates that the phase profile can be obtained by superimposing a blazed and an offset phase function............................. 92
Figure 5.7: Schematic representation of the continuous beam steering using LC phase shifters [9] 93

Figure 5.8: Schematic representation of the continuous beam steering using a scanning mirror after the MLA scanning system [69] 94
Figure 5.9: Lateral sliding and torsional vibration modes of a flexure mounted scanner [72] 95
Figure 5.10: Representation of lateral MEMS actuation for MLA beam scanners 96
Figure 5.11: A torsional MEMS actuation for micromirror scanner [70] 96
Figure 5.12: Deformation of micromirror scanner and the degration of the PSF at large scan angles due to large acceleration forces at the extremities of the scan. 97
Figure 5.13: Schematic representation of an endoscobic system where multi-mode fibers employed [77] 100
Figure 5.14: Endoscopic imaging system using multi-mode fiber nearby the scanning elements for collection of light [77] 100
Figure 5.15: IRCM system for detection and jamming of missile [79] 102
Figure 5.16: The scan head of an SLDV system contains an LDV sensor, a live color video-camera and xy deflection mirrors. [80] 103
Figure 5.17: The deflection mirrors can automatically direct the laser beam to the desired positions on a user-defined area. [80] 103

NOMENCLATURE

n	the refractive index
$f_{\#}$	lens f-number
σ	RMS wavefront error
λ_{im}	wavelength of the imaged source
λ_{sc}	wavelength of scanning
k	wave-vector
$A(\lambda)$	spectral distribution
$U(x)$	field distribution
OPD	optical path length difference
MTF	modulation transfer function
PSF	Point spread function
V	the Strehl ratio
$\mathcal{F}$	Fourier transform operator
$\mathcal{V}$	Scaling operator
f_s	data sampling frequency
MLA	Microlens array
PSL	Pre-scan lens
MMLA	Moving Microlens array
DMLA	Double Microlens array
D	beam diameter
d	Microlens diameter
N	# of microlenses in 1D
f_{MLA}, f_{PSL}	focal length of Microlens array

θ	system scan angle
α, β	scan angles of PSL and MMLA
r_1, r_2	amount of displacements of PSL and MMLA
δ	Nyquist sampling distance
δx	sampling distance
Δx	sampled field size
$\Delta\xi$	extension in spatial frequency

CHAPTER 1

INTRODUCTION

The field of MOEMS (Micro-Opto-Electro-Mechanical Systems) is a fast growing field with many applications in biomedical, telecommunications and defense industries. Among many novel MEMS devices, MEMS scanners are used to scan an optical beam in display, imaging, tracking and switching systems. [1] Compact, high resolution and fast beam scanners are especially of demand in the listed application areas. In this thesis, a high resolution and compact beam scanner system is demonstrated. Operation of the system is based on lateral displacement of a microlens array (MLA). This work suggests and demonstrates solutions to some of the diffraction problems appearing in the MLA scanning systems. Design considerations of MLA scanning system are discussed along with suggestions to improve the system performance by considering diffraction and aberration in the system.

This chapter includes brief literature review on MLA laser beam scanners. Chapter 2 introduces a novel solution to the discrete addressing problem in MLA scanning systems and includes analytical formulation, numerical demonstration and experimental verification for continuous scanning with the MLA scanning system. Chapter 3 studies optical system design by mainly focusing on diffraction and aberration performance of the system. Additionally, MLA fabrication methods are discussed, experimental results are presented in that chapter. Chapter 4, discusses implementation of the system and presents actuation schemes for displacement of optical elements. In that chapter, propagation of a beam is modeled by considering different cases regarding spatial and temporal coherence of the source. Chapter 5 compares MLA scanner systems with the most common beam scanner systems such as, micromirror [2] and LC scanners [3], and proposes three applications for

MLA scanner systems namely: endoscopic imaging, infrared countermeasure systems and scanning laser Doppler vibrometry. The conclusion chapter briefly overviews, highlights prospects of and future work in MLA scanners.

1.1. Literature review

1.1.1. Beam steering using microlens arrays (MLAs)

MLAs beam scanners are reported previously as high resolution agile beam scanners.[4],[5] However, immature fabrication techniques for micro-optical elements, preclude the applications MLA scanners. Nowadays, recent advancements in micro-fabrication technologies such as direct laser writing fabrication [6] paves the way of laser beam steering applications using displaced microlens arrays (MLAs).

Scanning of microlens arrays by displacement can be understood by considering scanning by displacement of one of the two lenses separated by two focal lengths ($2f_{MLA}$). An additional field lens [7] can be placed in between the two lenses to tilt the beam and fill the aperture of last lens as illustrated in Figure 1.1. The three-lens system can be repeated in 2-D to form three-MLA structure. In such a system, the steering angle is depended on the MLA displacement and the focal length of a single microlens as it is in three-microlens system; and the maximum steering angle is independent from the number of lenses in the array. So, by increasing the number of microlenses, large beams can be scanned with small displacements. The system is much lighter compare to three-lens scanning systems [8].

The system is sketched in Figure 1.2. The first MLA is referred as moving-MLA (MMLA); and second and third MLAs are combined and notated as double-MLA (DMLA). Note that the distance between the 1st and 2nd MLA is adjusted to be $n \cdot f_{MLA}$ to account for the refractive index *n*, of the glass material. The diffraction resulted from the periodic structure of the MLA system limits the number of addressable points. Only some angular

positions can be addressed, where constructive interference conditions are satisfied. In literature a solution for that problem is suggested, however the suggested system requires an imaging system to be added to the MLA scanning system and displacement of bulky DMLA instead of light MMLA.[9]

Laser spot in the image plane is constructed by interference of beamlets output from the microlenses in DMLA. In general, the constructive interference conditions are satisfied only for a single wavelength at a time, i.e., the system is dispersive. Hence the system needs to be operated monochromatic. However, dispersive nature of the system can be utilized for spectroscopic analysis, i.e., analysis of imaged beam spectra, as discussed in the application chapter.

In this study, discrete addressing problem of MLA scanning system is studied and a solution is suggested. The solution suggests using a pre-scanning lens (PSL) to tilt the beam before the MLA scanning system. (Figure 1.2) The analysis in Chapter 2 demonstrates and verifies tilting the beam before the MLA system can be used for continuous scanning, i.e., overcoming the discrete addressing problem.

In literature comb-driven MEMS designs are used for lateral displacement of micro-optical elements.[10] The MLA scanning system can be implemented using MEMS actuators as illustrated in Figure 1.3. MLAs can be integrated or fabricated on to the MEMS actuators. [11]

In literature MLA scanners are suggested to be used in applications such as: detection and tracking systems, [8] telescope applications, [12] etc. In addition to these applications, biomedical imaging applications are discussed in the Chapter 4.

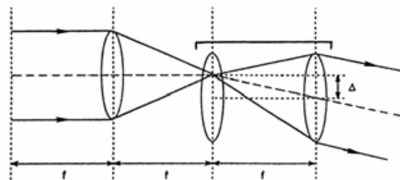

Figure 1.1: Three lens system for beam steering [4]

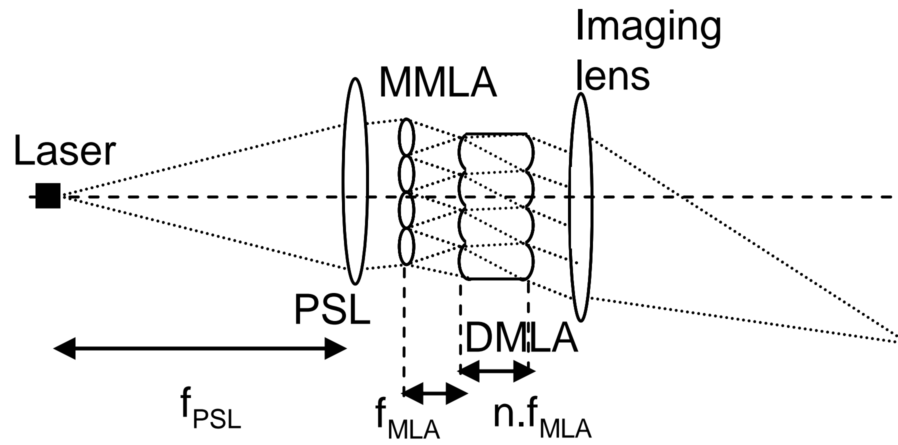

Figure 1.2: Microlens array beam steering system using three MLAs

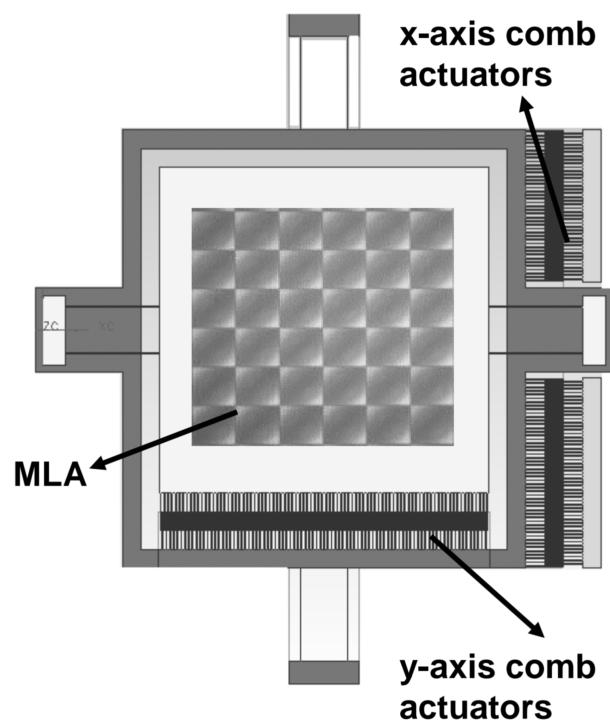

Figure 1.3: Representation of the lateral MEMS actuation for MLA beam scanners

CHAPTER 2

BEAM STEERING USING MLAS

2.1. Introduction

As discussed in the first chapter beam scanning by two MLAs separated by two-focal lengths offer a number of important advantages such as large scan angles obtained at smaller deflections (i.e. half the diameter of a microlens), and better aberration performance due to smaller lenses. One major problem with the MLA scanning system is the discrete angular addressability due to the periodic nature of the MLA.[13] In this chapter, a novel method for laser beam steering to arbitrary positions by overcoming the inherent diffraction problems is discussed.[14] In Sec. 2.2 scan angle and phase conditions for arbitrary scanning is explained using diffraction related phase conditions with certain assumptions based on Fourier optics theory. In Sec. 2.3, a mathematical proof is given for the scan angle and phase conditions given in Sec. 2.2 using the Fresnel diffraction integral.

2.2. Continuous scanning

A novel solution to the discrete addressability problem is tilting the beam before the MMLA by displacing the PSL. Figure 2.5 illustrates the physical optics view and the operation of the system. The lateral displacements of the PSL and the MMLA results in independent contributions to the beam scan angle given by:

$$\alpha = -r_1 / f_{PSL}; \qquad \beta = r_2 / f_{MLA}; \qquad \theta = \alpha + \beta \tag{2.1}$$

where the lens dimensions and deflections are as defined in the figure. The system is assumed linear and the total scan angle θ is calculated using superposition. A proof with

physical intuition for the linearity is given below, a more rigorous mathematical proof is given in section 2.3.

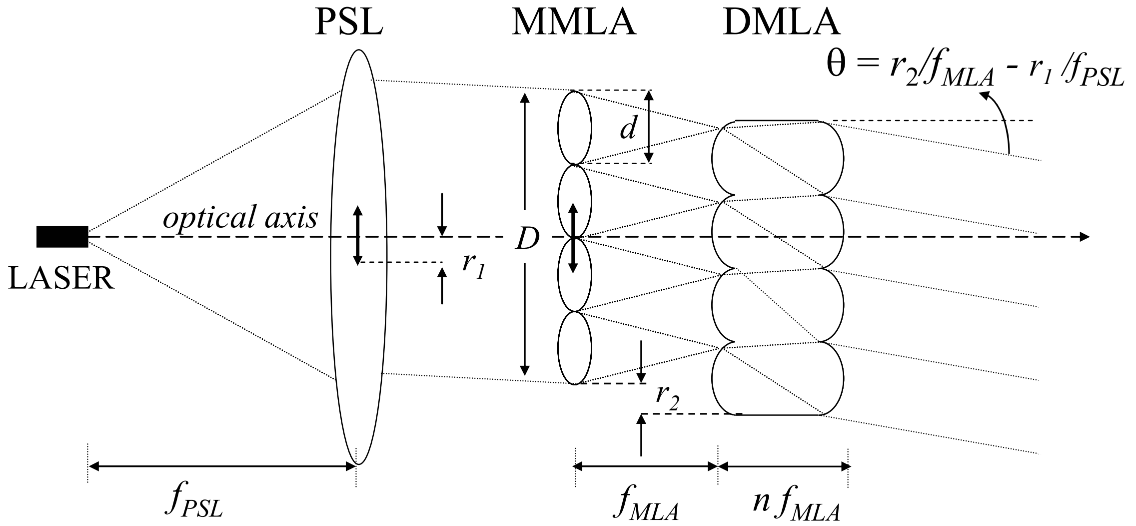

Figure 2.1: System geometry and steering of light by displacements of the PSL and MMLA. D: clear aperture size; d: microlens diameter; f_{PSL}: PSL focal length; f_{MLA}: MLA focal length; and r_1 and r_2 are PSL and MMLA displacements.

In order to analyze the PSL's contribution, the three-MLA block can be modeled as a parallel channelized processor, where each channel consists of three identical lenses with one focal distance separation. Figure 2.2.a illustrates the propagation of a plane-wave through the three-microlens system where L_1 coordinate axis is shifted. The beam is focused by L_1, tilted by L_2 and collimated by L_3 and the output is a plane wave tilted at an angle β. The figure 2.2.b illustrates the case of a plane-wave incident at an angle $-\alpha$, on L1 and no displacement in the system. In that case, the exiting wavefront is another plane wave at angle $(+\alpha)$, which is effectively rotated by $+2\alpha$ after propagation through the three-microlens system.

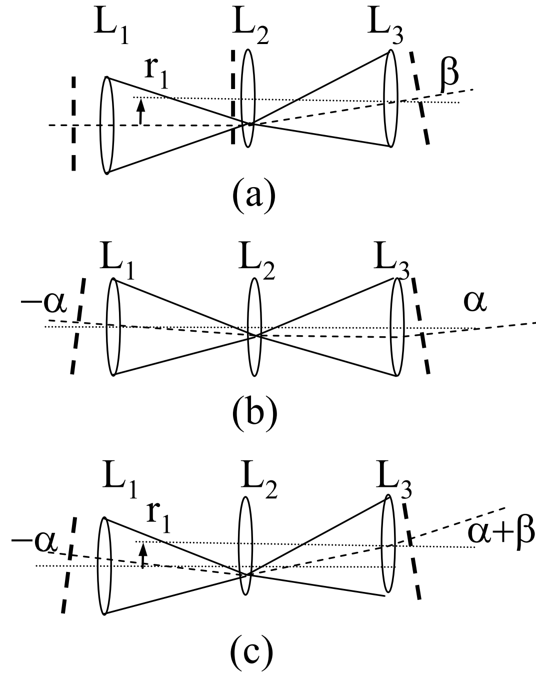

Figure 2.2: Propagation of the beamlets through the three-microlens system, represented for when (a) L1 is displaced by r_1 (b) the incident beam is tilted with angle $-\alpha$, and (c) combination of (a) and (b)

The analysis of the three-microlens system can be extended to the analysis of the three MLA system. To make the incident wavefront identical for each microlens channel, we play a trick and introduce constant phase shifters before and after each MLA channel. This takes care of the phase differences between MLA channels for the case of oblique beam incidence. The dummy phase shifter is a stair-like phase function that is first added before the microlenses and then subtracted after the microlenses. Thereby, it is ensured that each three-microlens channel has the same input and output. In Figure 2.3, two parameters of the beam are illustrated after the each element in the system: the beam tilt angle θ and the optical path length difference (OPD) between the beam segments in two neighboring channels. As illustrated in the figure, the dummy phase function forms a step function (ϕ)

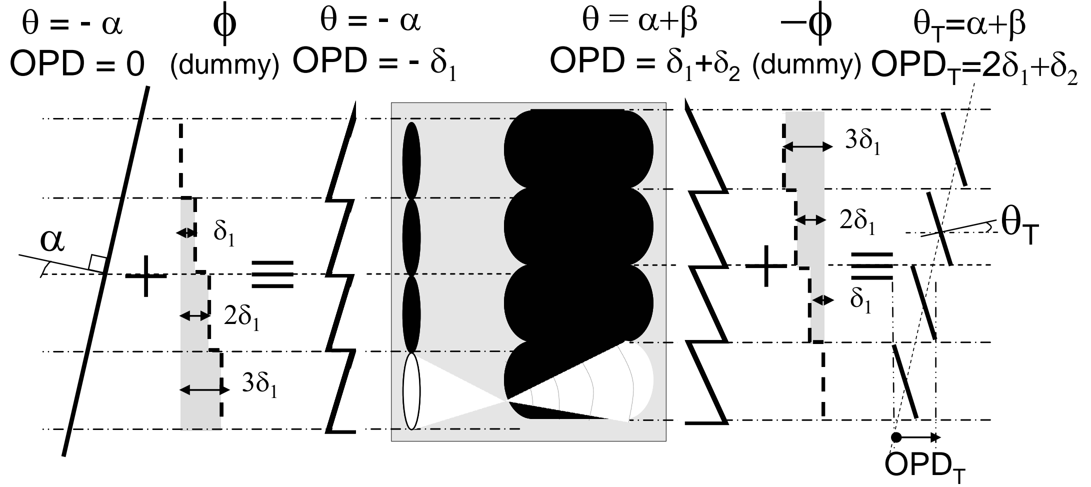

Figure 2.3: Physical optics view of the 3-MLA block system after the PSL. Scan angle and OPD between beam segments is marked after each element. (Dummy phase shifters have no net effect in the system)

with step heights of $\delta_1=\alpha d$, which correspond to the OPD between the neighboring channels. Thus, the contribution of the PSL's displacement to θ and OPD can be calculated as α and $2\delta_1$, respectively. For the case of normal plane wave incidence, the MMLA contribution to θ and OPD can be calculated as β and $\delta_2=\beta d$ respectively. The total scan angle θ_T of the beam and the inter-channel phase difference between wave OPD_T are expressed as the sum of independent contributions of the PSL and the MMLA:

$$\theta_T = \alpha + \beta \tag{2.2}$$

$$OPD_T = 2\delta_1 + \delta_2 = (2\alpha + \beta)d \tag{2.3}$$

Constructive interference between wavefront segments at the focal position is required. Therefore, the OPD_T in (2.3) should satisfy the following condition for all α and β:

$$OPD \equiv n\lambda\,, \quad \text{where} \quad n=0, \pm1, \pm2 \ldots \tag{2.4}$$

As a last word before starting with the physical optics analysis of the system, the arbitrary scan angles, θ_T, with constructive interference can be obtained by choosing r_1 and r_2 according to the above conditions and can be expressed as:

$$r_1 = (\theta_T - n\lambda / d) f_{PSL} \quad ; \quad r_2 = (\theta_T + r_1 / f_{PSL}) f_{MLA} \tag{2.5}$$

where n is an integer and chosen such that $|r_1|$ is smallest to minimize the required PSL motion. For each scan angle in the range, there is a solution with a PSL deflection smaller than $\lambda f_{PSL}/2d$.

2.3. Analytical formulation

In the previous section, arbitrary scan angle conditions for displacement values of the PSL and MMLA are derived intuitively using optical beam interference arguments. The preceding arguments have been heuristic, and in fact have certain hidden assumptions and approximations. In this section a more rigorous approach is followed and analytical formulations are presented, using Fourier optics beam propagation methods. An analytical expression for point spread function (PSF) of the system is derived and the phase conditions given in the previous section is verified using the PSF function.

2.3.1. Fourier optics analysis

Throughout this work, in the physical optics analysis only waves that are traveling nearly parallel to the z axis are considered and scalar modeling of the system assumed to be valid. Figure 2.4 illustrates electromagnetic wave propagation from a point P_0 to P_1 at coordinates $(x_0,y_0,0)$ and (x_z,y_z,z), respectively. Paraxial approximation requires $z^2 >> (x_z-x_0)^2+(y_z-y_0)^2$, i.e., θ is small or the aperture size is greatly smaller than the propagation distance z). In that case, the Huygens-Fresnel principle can be used for the formulation of propagation of a field between two planes. The Huygens-Fresnel principle states that each point on a wavefront can be considered as a point source and beam propagation can be

considered as a superposition of the fields resulted with the propagation of these secondary point sources and can be formulated as [15]:

$$U_z(x_z, y_z) = C\int_{-\infty}^{+\infty}\int_{-\infty}^{+\infty} U_0(x_0, y_0)\frac{\exp(ikr)}{r}dx_0 dy_0 \qquad (2.6)$$

where C is a constant, $k=2\pi/\lambda$ is the wave-vector, and $r^2 = z^2+(x_z-x_0)^2+(y_z-y_0)^2$. The term $U_0(x_0, y_0)$ represents the field transmitted from the point P_0 positioned at x_0, y_0. This term is multiplied by the spherical beam phase function, $\frac{\exp(jkr)}{r}$, and yields the contribution of the field at the output plane, emanating from the point P_0. When integrated in the aperture plane over x and y, all contributions of point sources are superimposed and yield the resultant field at the point P_1. The spherical function $\frac{\exp(jkr)}{r}$ can be approximated as $\exp(j\frac{k}{2z}(x^2+y^2))$ using the binomial approximation. Then, the Huygen's principle can be expressed as a convolution and the Fresnel equation can be obtained in convolution form:

$$U(x_z, y_z) = C \times U(x_0, y_0) * e^{j\frac{k}{2z}(x_0{}^2+y_0{}^2)} \qquad (2.7)$$

where C is a constant. Using the C expression in the reference [15], the Fresnel equation can be expressed as:

$$U(x_z, y_z) = \frac{e^{jkz}}{j\lambda z}\int_{-\infty}^{+\infty}\int_{-\infty}^{+\infty} U(x_0, y_0)e^{j\frac{k}{2z}((x_z-x_0)^2+(y_z-y_0)^2)}dx_0 dy_0 \qquad (2.8)$$

When the square terms are factored out another form of the Fresnel equation can be obtained:

$$U_z(x_z,y_z)=\frac{e^{jkz}}{j\lambda z}e^{j\frac{k}{2z}(x_z{}^2+y_z{}^2)}\times\int_{-\infty}^{+\infty}\int_{-\infty}^{+\infty}U(x_0,y_0)e^{j\frac{k}{2z}(x_0{}^2+y_0{}^2)}e^{-j\frac{k}{z}(x_0x_z+y_0y_z)}dx_0dy_0 \tag{2.9}$$

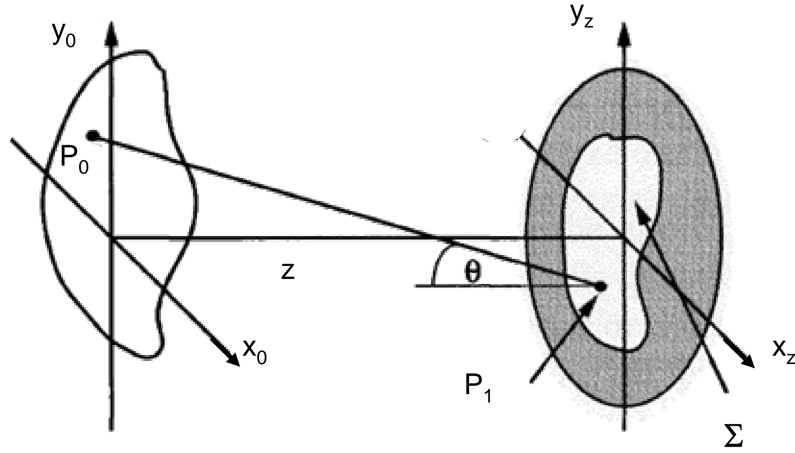

Figure 2.4: Representation of the Huygens-Fresnel principle showing integration of the beams emanating from the aperture plane and incident on the output plane

In the rest of this work, in order to simplify the analysis, without loss of generality, 1-D formulation is used. Furthermore, since the main interest in this work is the field distribution not the amplitude of the fields, the constant terms preceding the integral is not considered. In 1-D form, the Huygens-Fresnel diffraction integral is given by:

$$U_z(x_z)=e^{j\frac{k}{2z}(x_z{}^2)}\int_{-\infty}^{+\infty}U_0(x_0)e^{j\frac{k}{2z}x_0{}^2}e^{-j\frac{k}{z}(x_0x_z)}dx_0 \tag{2.10}$$

For an elaborate discussion and derivation of the above integral equation from Kirchhoff and Rayleigh-Sommerfeld theories reader is suggested to refer Goodman's textbook titled Introduction to Fourier Optics.[16] In the following analysis, the propagation through the system is modeled using the Fresnel propagation equation.

Simplifications to the analysis is followed by formulation of the system using merely Fourier transform operations and coordinate scaling. The Fourier transform operation can be defined as:

$$A(f_x) = \mathcal{F}\left[U(x)\right] = \int_{-\infty}^{+\infty} U(x)\, e^{-j2\pi x f_x}\, dx \tag{2.11}$$

Similarly the inverse Fourier operation is defined:

$$U(x) = \mathcal{F}^{-1}\left[A(f_x)\right] = \int_{-\infty}^{+\infty} A(f_x)\, e^{+j2\pi x f_x}\, df_x \tag{2.12}$$

2.3.2. Beam propagation through the three microlens channel

The propagation through the system of three-MLAs can be modeled as propagation of segmented beams through identical parallel channels of microlenses, as discussed in section 2.1. Each channel is composed of three microlenses at one-focal length distance and beam scanning is achieved by lateral translation of the first microlens.

The three-microlens system can be analyzed in two parts as illustrated in Figure 2.5. Direct elementary Fourier optics analysis would reveal that, each part would be recognized as an optical Fourier transform module where the combination is an imaging system with a magnification of -1. The analysis below is a derivation of this well-known fact following the Huygens-Fresnel diffraction integral.[16] The results are then modified for the cases of oblique beam incidence and MLA in-plane shifts.

In the first part, the propagation to the front of the 2nd microlens can be analyzed. Assuming a plane wave incidence, propagation to the back focal plane is equivalent to the Fourier transformation of the apertured input beam.

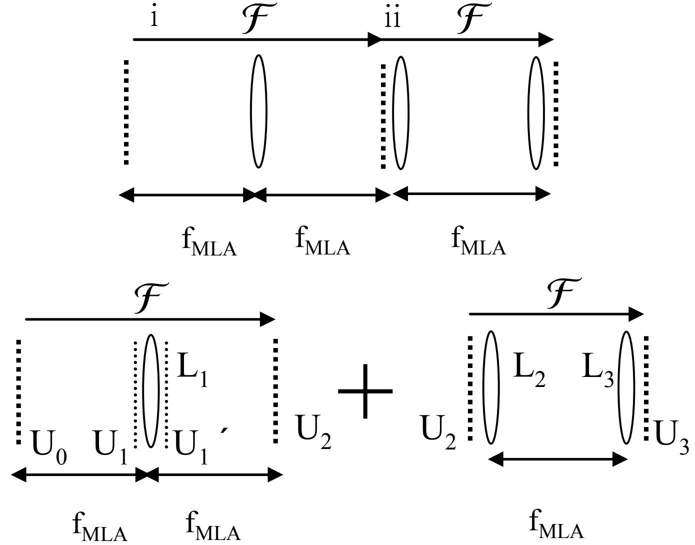

Figure 2.5: Representation of propagation through the three microlens system. Propagation through the system is represented as two consecutive Fourier operations.

The initial field is an apertured plane wave, which can be defined by a binary transmission function *t*(x):

$$U_1(x) = t(x) \tag{2.13}$$

Throughout this work, paraxial approximation and thin lens representation of the lens phase function is assumed. With the assumption the lens function can be approximated by a quadratic phase factor. Then, the field after the first lens is equal to the initial field multiplied by the lens phase function

$$U_1'(x_1) = U_1(x_1)\exp\left[-j\frac{k}{2f_{MLA}}x_1^{\,2}\right] \tag{2.14}$$

This field can be propagated by a distance f_{MLA} to the back focal plane of the lens using the Fresnel equation given in (2.10). The quadratic terms inside the integral cancels each other and the field at the focal plane noted by U_2 becomes:

$$U_2(x_2) = e^{j\frac{k}{2f_{MLA}}x_2^2} \int_{-\infty}^{+\infty} U_1(x_1) e^{-j\frac{k}{f_{MLA}}x_1x_2} dx_1 \qquad (2.15)$$

Note that the integral term in (2.15), is equivalent to a scaled Fourier operation using the substitution $f_x = x_2/\lambda f_{MLA}$. Let, $F_1(f_x)$ represent the scaled Fourier transforms of the beam incident on the lens $U_1(x)$, such that:

$$F_1(f_x) = \mathcal{V}[\frac{1}{\lambda f_{MLA}}]\{\mathcal{F}(U_1(x_1))\}, \qquad (2.16)$$

where the function $\mathcal{V}$ denotes scaling of the coordinate axis and the function is defined such that $\mathcal{V}[b]\{U(x)\} = U(bx)$.

So, (2.15) can be expressed using $F_1(f_x)$:

$$U_2(x_2) = e^{j\frac{k}{2f_{MLA}}x_2^2} F_1(f_x), \quad (f_x = x_2/\lambda f_{MLA}) \qquad (2.17)$$

Further simplification of the analysis is possible by eliminating the spherical phase multiplication prior to the integral. For that purpose, without loss of generality the beam, instead of U_1, U_0 -which is at a distance d in front of the L_1 (Figure 2.5), is used as the initial field for the convenience of the analysis. $F_0(f_x)$ can be defined like $F_1(f_x)$ is defined in (2.16). The relation between $F_0(f_x)$ and $F_1(f_x)$ can be established using Fourier optics plane wave propagation method [19]:

$$F_1(f_x) = F_0(f_x) \ \exp\left[-j\pi\lambda d f_x^2\right] \qquad (2.18)$$

where d is the distance between two propagation planes. That way, the equation can be expressed as a Fourier integral. Substituting (2.18) into (2.17) results:

$$U_2(x_2) = e^{j\frac{k}{2f_{MLA}}(1-\frac{d}{f_{MLA}})x_2^2} F_0(f_x) \qquad (2.19)$$

As can be seen, when distance d is equal to focal length f_{MLA}, U_2 is equal to the Fourier transform of the input beam:

$$U_2(x_2) = \mathrm{F}_0(f_x) = \mathcal{V}[\frac{1}{\lambda f_{MLA}}]\{\mathcal{F}(U_0(x_0))\} \tag{2.20}$$

The second part of the system in Figure 2.5 is composed of two lenses separated by a focal distance. The propagator for that part of the system should include a spherical phase factor multiplication for propagation through L_2, free space propagation by a distance f_{MLA} and another spherical phase factor multiplication for propagation through L_3. In order to simplify the analysis by eliminating the spherical phase multiplications, free space propagation equation (2.10) can be expressed as a scaled Fourier transform operation with preceding and succeeding spherical phase multiplications and a coordinate scaling operation. Note that in this step $f_x = x_3/\lambda f_{MLA}$ is used for replacing the integral with a Fourier operation:

$$U_3(x_3) = e^{j\frac{k}{2f_{MLA}}x_3^2} \int_{-\infty}^{+\infty} U_2(x_2) e^{j\frac{k}{2f_{MLA}}x_2^2} e^{-j\frac{k}{f_{MLA}}(x_2 x_3)} dx_2 \tag{2.21}$$

$$= e^{j\frac{k}{2f_{MLA}}x_3^2} \mathcal{V}[\frac{1}{\lambda f_{MLA}}]\left\{\mathcal{F}[U_2(x_2)\, e^{j\frac{k}{2f_{MLA}}x_2^2}]\right\} \tag{2.22}$$

Where x_2 is the coordinate of the initial plane and the x_3 is the coordinate of the final plane after the propagation. The field distribution in front and behind of the L_2 are noted as U_2 and U_2' (Figure 2.5), respectively and the relation between the two is:

$$U_2'(x_2) = U_2(x_2)\exp\left[-j\frac{k}{2f_{MLA}}x_2^2\right] \tag{2.23}$$

Using (2.10), U_3 can be expressed as:

$$U_3(x_3) = e^{j\frac{k}{2f_{MLA}}x_3^2} \int_{-\infty}^{+\infty} U_2'(x_2) e^{j\frac{k}{2f_{MLA}}x_2^2} e^{-j\frac{k}{f_{MLA}}x_2 x_3} dx_2 \tag{2.24}$$

Substituting (2.23) simplifies the above equation to:

$$U_3(x_3) = e^{j\frac{k}{2f_{MLA}}x_3^2} \int_{-\infty}^{+\infty} U_2(x_2) e^{-j\frac{k}{f_{MLA}}x_2 x_3} dx_2 \tag{2.25}$$

And after propagation through the third microlens the field distribution at the output of the lens system U_{out} *(=* U_3'*)* is obtained to be:

$$U_{out}(x_3) = U_3'(x_3) = e^{-j\frac{k}{2f_{MLA}}x_3^2} U_3(x_3) \tag{2.26}$$

$$= \int_{-\infty}^{+\infty} U_2(x_2) e^{-j\frac{k}{f_{MLA}}x_2 x_3} dx_2 \tag{2.27}$$

And can be expressed by a scaled Fourier transform operation:

$$U_{out}(x_3) = U_3(x_3) = \mathcal{V}[\frac{1}{\lambda f_{MLA}}]\{\mathcal{F}[U_2(x_2)]\} \tag{2.28}$$

Substituting (2.20) into the (2.28) yields:

$$U_{out}(x_3) = U_3(x_3) = \mathcal{V}[\frac{1}{\lambda f_{MLA}}]\left\{\mathcal{F}\left(\mathcal{V}[\frac{1}{\lambda f_{MLA}}]\{\mathcal{F}(U_0(x_1))\}\right)\right\} \tag{2.29}$$

$$= \int_{-\infty}^{+\infty}\left(\int_{-\infty}^{+\infty} U_0(x_1) e^{-j\frac{2\pi}{\lambda f_{MLA}}x_1 x_2} dx_1\right) e^{-j\frac{2\pi}{\lambda f_{MLA}}x_2 x_3} dx_2 \tag{2.30}$$

Substitution of $x_2' = x_2 / \lambda f_{MLA}$ in place of x_2, simplifies the scaling terms and noting that constant multiplier terms are not considered, (2.30) results to:

$$U_{out}(x_3) = \int_{-\infty}^{+\infty}\left(\int_{-\infty}^{+\infty} U_0(x_1)\exp(-j2\pi x_1 x_2')dx_1\right)\exp(-j2\pi x_2' x_3)dx_2' \tag{2.31}$$

$$= \mathcal{F}(\mathcal{F}(U_0(x)) \tag{2.32}$$

One could rewrite (2.32) as:

$$U_{out}(-x_3) = \int_{-\infty}^{+\infty}\left(\int_{-\infty}^{+\infty} U_0(x_1)\exp(-j2\pi x_1 x_2')dx_1\right)\exp(+j2\pi x_2' x_3)dx_2' \tag{2.33}$$

$$U_{out}(-x) = \mathcal{F}^{-1}(\mathcal{F}(U_0(x)) \tag{2.34}$$

$$U_{out}(-x) = U_0(x) \tag{2.35}$$

After changing the sign of the functions, the output field is found to be:

$$U_{out}(x) = U_0(-x) \tag{2.36}$$

In summary, the system consists of two consecutive Fourier operations, which is equivalent to imaging with magnification of -1. Tilted beam incidence and coordinate shift cases are investigated in the following subsections.

2.3.3. Lens displacement

The scanning of the beam by displacement of L_1 by an amount r_2 can be analyzed as a coordinate shift in the optical axis. The shifting of L_1 can be considered as a shift of optical axis all through the first step propagation, including the free space propagation from U_0 to L_1 and L_1 to the front of L_2 (Figure 2.5). So the coordinate shift can be formulated as a shift between two propagation steps which are formulated by two consecutive Fourier transform operations. Hence, the field after the first step propagation is shifted so that : $U_2(x_2) \rightarrow U_2(x_2 - r_2)$. By defining another position variable such that: $x_2' = x_2 - r_2$, and substituting $U_2(x_2 - r_2)$ into (2.26):

$$U_{out}(x_3) = \int_{-\infty}^{+\infty} U_2(x_2 - r_2) e^{-j\frac{k}{f_{MLA}}(x_2)x_3} dx_2 \tag{2.37}$$

$$= \int_{-\infty}^{+\infty} U_2(x_2') e^{-j\frac{k}{f_{MLA}}(x_2'+r_2)x_3} dx_2' \tag{2.38}$$

$$= e^{-jk\frac{r_2}{f_{MLA}}x_3} \int_{-\infty}^{+\infty} U_2(x_2') e^{-j\frac{k}{f_{MLA}}x_2' x_3} dx_2' \tag{2.39}$$

Using (2.26) and (2.36), (2.39) can be rewritten as:

$$U_{out}(x_3) = e^{-jk\frac{r_2}{f_{MLA}}x_3} U_0(-x) \tag{2.40}$$

$$= e^{-jkx_3 \sin\theta} U_0(-x), \quad (\theta = \sin^{-1}(r_2/f_{MLA})) \tag{2.41}$$

The preceding linear phase function is a representation of beam tilting at an angle of $\theta=\sin^{-1}(r_0/f_{MLA})$. So displacement of L_1 results in tilting of the beam at the output.

2.3.4. Oblique beam incidence

In the analysis of oblique beam incidence at an angle α, the incident beam can be expressed as a linear phase function:

$$U_0(x) = \exp\left[-jk(x \cdot \sin\alpha)\right] \tag{2.42}$$

Then using (2.36) the output field becomes:

$$U_{out}(x) = U_0(-x) = \exp\left[-jk(-x \cdot \sin\alpha)\right] \tag{2.43}$$

$$= \exp\left[-jk(x \cdot \sin(-\alpha))\right] \tag{2.44}$$

As seen in the equation the initial tilt angle α changes sign and the beam is tilted in the reverse direction at the output at an angle $-\alpha$.

Displacement of L_1 and oblique incidence, contributes to the beam's tilting at the output and these independent contributions can be superimposed since the Fourier transformation is a linear operation. Considering both, lens displacement and oblique beam incidence, the field at the output of the microlens system becomes:

$$U_{out}(x) = e^{-jkx\sin\theta} U_0(-x) \tag{2.45}$$

$$= \exp(-jkx\sin\theta) \times \exp\left[-jk(x \cdot \sin(-\alpha))\right] \tag{2.46}$$

$$= \exp\left[-jk(x(\sin\theta + \sin(-\alpha))\right] \tag{2.47}$$

Notice that, the representation in the Figure 2.2 can be verified using the equation (2.47)

2.3.5. Point spread function (PSF) of the system

In this section analytical formulation of the PSF and resolution of the MLA based beam steering system is developed. Firstly, PSF formulation for the case of MLA displacement is developed and than a formulation for oblique beam incidence case follows.

As studied in the previous section, displacement of the L_1 tilts the beam at the output of microlens system. Likewise in the MLA system, displacement of the MMLA tilts the beam segments behind the MLA2. As the channels are identical and the initial beam is uniform, output beams from each channel are identical. Considering the one-dimensional case, the beam phase profile after the MLA system would be like that of a blazed grating as shown in the Figure 2.3. Transmission equation can be expressed as a convolution of a comb function and output from a single channel:

$$t(x) = \left[\exp\left(-i2\pi r_2 x/\lambda f_{MLA}\right)\mathrm{rect}\left(x/a\right)\right] \tag{2.48}$$

$$*\left[\left(1/d\right)\mathrm{comb}\left(x/d\right)\mathrm{rect}\left(x/Nd\right)\right] \tag{2.49}$$

where the comb(x/d) function represent a train of Dirac-delta functions extending to infinity with spacing d and the rect(x/D) function represents a rectangular window function with width of *D*.

The above transmission function also determines the near-field distribution of the beam after the MLA system. When this field is propagated to the back focal plane of another Fourier transform lens acting on all the microlenses, the resulting intensity profile is found to be:

$$I(\theta) = \left(Nad\right)^2 \left[\begin{array}{c} \underbrace{\mathrm{sinc}\left[\left(a/\lambda\right)\left(\sin\theta - r_2/f_{MLA}\right)\right]}_{I_1} \times \\ \underbrace{\left[\mathrm{comb}\left(d\sin\theta/\lambda\right) * \mathrm{sinc}\left(Nd\sin\theta/\lambda\right)\right]}_{I_2} \end{array}\right]^2 \tag{2.50}$$

Figure 2.6 sketches the PSF and illustrates the envelope and periodic Sinc functions denoted by I_1 and I_2, respectively. The PSF is plotted as a function of displacements r_1 and r_2. As the MMLA is decentered, I_2 remains intact, but I_1 begins to shift, so that intensity of the 0th diffraction order begins to decrease while the 1st diffraction order intensity increases. At a certain point, the intensities of the two orders become equal and the spot on the diffraction plane is equally split into two. Further displacement of the MMLA strengthens the 1st diffraction order and when $r_2 = f_{MMLA}\lambda / d$, the diffraction profile is a single spot located at the 1st order. Due to the periodic profile of I_2, intermediate angles between the diffraction orders can not be addressed by mere deflection of the MMLA.

The periodic Sinc function (I_2), is modified by an envelope function denoted as I_1. The period of the Sinc functions is determined by the comb function in the $\sin\theta$ angular coordinate system. The displacement of the MLA is equivalent to a shift of the Sinc envelope in $\sin\theta$ coordinate system, thus results in steering of the beam in the image plane.

One should also consider the oblique beam incidence for a complete formulation of the system. Two adjustments to the equation (2.50) are needed to formulate the oblique incidence case. The initial beam is incident at an angle α. since each microlens channel reverses the direction of the tilt, each beam segment at the channel output is tilted with respect to the incidence angle by $\sin^{-1}(2\sin\alpha)$, which is approximately equal to 2α in paraxial regime. This can be formulated as follows:

$$\begin{aligned} t(x) = &\left[\exp\left(-ikx(2\sin\alpha + \sin\beta)\right)\mathrm{rect}\left(x/a\right)\right] \\ &*\left[\left(1/d\right)\mathrm{comb}\left(x/d\right)\mathrm{rect}\left(x/Nd\right)\right] \\ &\times\exp(ikx\sin\alpha) \end{aligned} \tag{2.51}$$

where $\beta = r_2/f_{MLA}$.

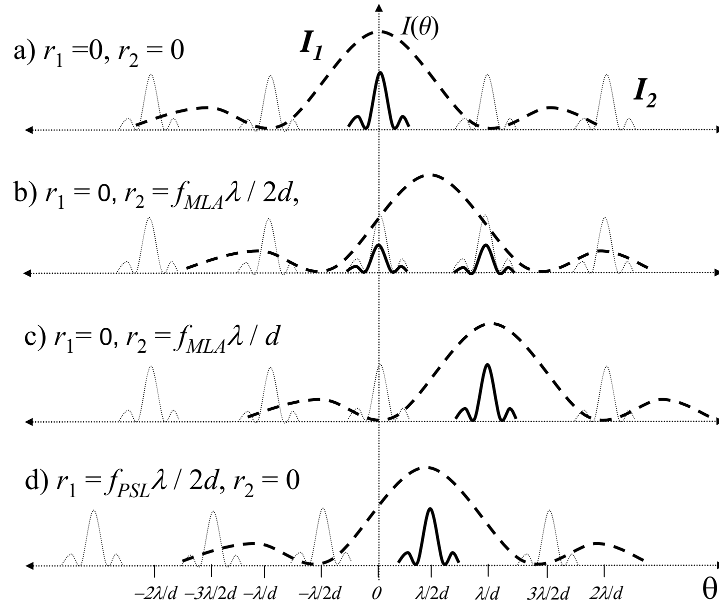

Figure 2.6: Representation of the periodic and envelope Sinc functions which forms the PSF

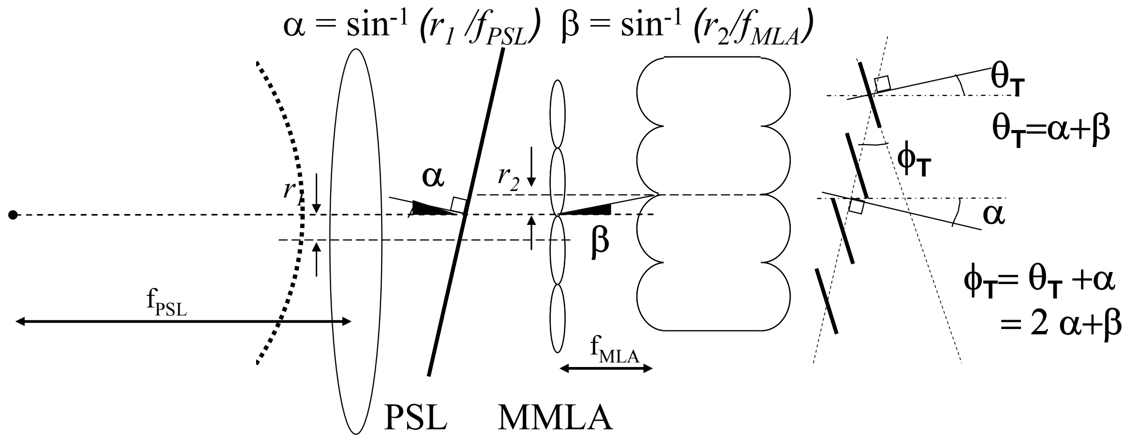

Figure 2.7: Contributions of the PSL and MMLA to the scan angle and inter-channel OPD at the output

When this field is propagated to the far-field where the beam is focused in the image plane, the field becomes:

$$I(\theta)=(Nad)^2\,\text{sinc}^2\left[(a/\lambda)(\sin\theta-\sin\beta-\sin\alpha)\right] \times\left[\text{comb}\left(d(\sin\theta+\sin\alpha)/\lambda\right)*\text{sinc}\left(Nd(\sin\theta+\sin\alpha)/\lambda\right)\right]^2 \quad (2.52)$$

As seen in the above equation, the effect of pre-tilting the beam is shifting of the coordinate axis and $\sin\alpha$ term appears together with the $\sin\theta$ term. Both in (2.50) and (2.52), the two main terms can be described as a wide Sinc envelope function and a periodic array of narrow Sinc functions. Coordinate shifts appear to be in the same amount, but in the reverse directions for periodic and envelope Sinc functions. The coordinate shifts in the image plane intensity are equivalent to the scanning of the beam, and so it may be concluded that when the incident beam is tilted by $-\alpha$, the segments of the output beam are tilted by $+\alpha$. On the other hand, the overall beam direction $-\alpha$, which can be defined by the inter-channel phase differences as shown in the Figure 2.7, is preserved after the propagation through MLAs. Note that, OPD shown in Figure 2.3 is related to the quantity ϕ_T in Figure 2.7 as ϕ_T=OPD/d.

The phase condition required for continuous scanning as discussed in Section 2.2 can be verified using equation (2.52) by setting the argument of the comb function to be an integer so the value of the comb-function is nonzero. The condition is given by:

$$\sin\theta+\sin\alpha\equiv n\lambda/d \quad (2.53)$$

The total beam scan angle is determined by the first Sinc term. The center of the PSF can be found by setting the argument of the Sinc envelope function to zero:

$$\sin\theta=\sin\beta+\sin\alpha \quad (2.54)$$

and using the paraxial approximation, the following results of Section 2.2 can be verified:

$$2\alpha+\beta\equiv n\lambda/d \;\text{ (phase condition)} \quad (2.55)$$

$$\theta=\alpha+\beta \;\text{ (scan angle)} \quad (2.56)$$

2.4. Numerical demonstration

In the previous section analytical methods are developed for analysis of propagation of a beam through the system. Analytical methods are very helpful for understanding the mechanisms of the system and getting quick solutions to specific problems. However, in most problems analytical formulation can be developed only for particular cases (e.g., particular system geometries) and for some problems it is not possible; whereas, numerical methods can be implemented for the analysis of larger range of problems. Coming back to the analysis of MLA system, analysis of the system employing lenses of different shapes and profiles would let understanding of the ways to improve the system performance. Developing an analytical formulation for each variation of the system might get painful; however, numerical simulation is straightforward. Hence, in this section, a numerical implementation of propagation through the system is discussed; and the phase condition given in section 2.2 is simulated.

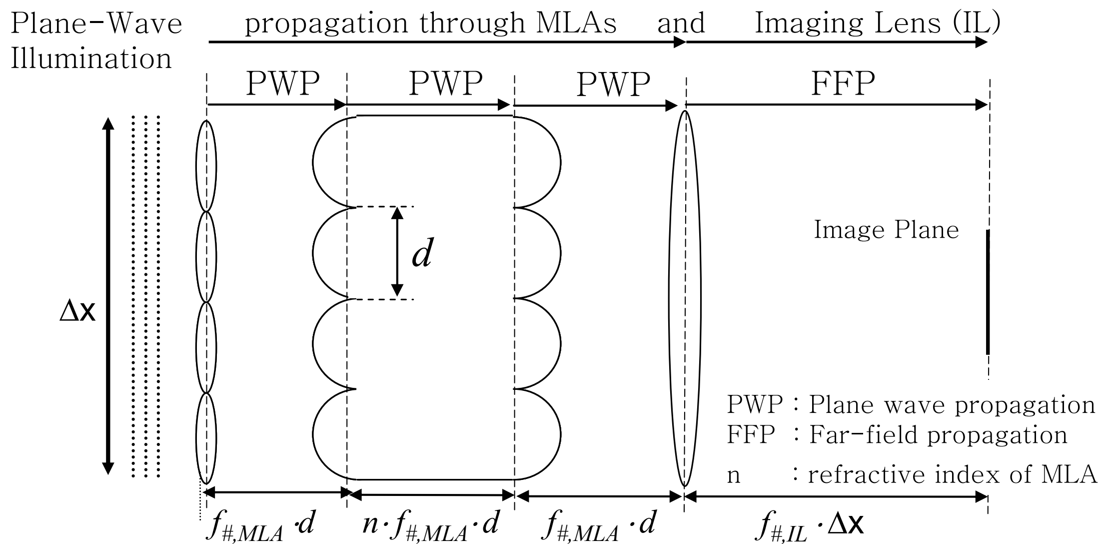

Figure 2.8: Simulation of the system using different simulation methods.

A number of free space beam propagation methods are evaluated for simulation of different stages of the optical train. All methods are valid approximations to the Fresnel equation given in equation (2.8). Since the numerical implementation requires sampling of the integral and representation of the field by limited number of sample points (N), which is limited by physical memory of the computer, care is needed to avoid sampling errors.

In the simulation of the system, the plane wave illumination is considered. The propagation through the system can be separated in to two steps. In the first step, the plane wave incident on the first MLA is propagated through the MLA2 and MLA3. In the second step, a nearly collimated beam is incident on the imaging lens, and propagated to the image plane, where it forms a focused spot, which is the PSF of the system. Simulation of different system geometries in the two propagation steps requires implementation of different numerical methods to minimize the numerical errors (i.e., sampling errors). In the rest of this section, various propagation methods are evaluated in terms of their accuracy in numerical implementation; and two methods implemented for simulation of the system as illustrated in Figure 2.8.

For each propagation method the beam is analyzed for propagation from $\hat{z}=0$ plane to the $\hat{z}=z$ plane. The field is defined to have size Δx_0 and Δx_z, where the subscripts denote the $\hat{z}$ position of the plane. The field is sampled at the following points:

$$\begin{aligned} x_0 &= m\cdot\delta x_0, \quad m=1..N \\ x_z &= m'\cdot\delta x_z, \ m'=1..N \end{aligned} \tag{2.57}$$

where N is an exact power of 2. The sampling periods are defined as:

$$\delta x_0 = \Delta x_0 / N, \quad \delta x_z = \Delta x_z / N \tag{2.58}$$

Nyquist theorem states, sampling frequency, f_s, should be bigger than twice the frequency bandwidth, $\Delta\xi_0$, of the system, such that $f_s > 2\Delta\xi_0$. In other words, sampling period, δ, should be half the size of the object's finest detail, δx_0:

$$\delta = \delta x_0 / 2$$
$$\delta x_0 = \Delta x_0 / N = 1/\Delta \xi_0 = 1/\Delta \xi_z \quad (2.59)$$

The numerical simulation parameters and system geometry values used for definition of the simulation system is given in Table 2.1:

# of sample points:	$N\times N = 2048\times 2048$
Extend of the beam in the initial plane of propagation:	$\Delta x_0 = 2$mm
Diameter of a microlens:	d= 100μm
Number of lenses in 1-D:	$n=\Delta x_0/d = 20$
Wavelength of operation:	$\lambda = 0.635$ μm

Table 2.1: The numerical simulation parameters and system geometry values

The propagation algorithms are coded in MATLAB and C++ environments. In both environments, the propagation methods are implemented using available Fast Fourier Transform (FFT) functions. Since C++ code is compiled to an executable file which uses basic system commands, it works faster and can handle larger data. The finer the system is sampled, the more accurate results can be obtained and the faster varying phase functions can be simulated. Matrix functions are easier in MATLAB, however, due to computational superiority, C++ preferred in this study for numerical simulations

Turning back to the propagation methods, the second step is implemented by a single Fourier transformation and the analysis is relatively straightforward compared to the first step. Let's begin with the second propagation step.

2.4.1. Far-Field Propagation (FFP)

In the second step, the beam is propagated to the image plane starting from the back of the MLA3. After the MLA3, the beam is focused to the image plane by an imaging lens (IL), and numerical implementation can be done by a single Fourier transform operation. The field amplitude after the MLA3, $U_3(x_1)$, is propagated through the imaging lens, the

field after the imaging lens can be found by a multiplication with the thin lens phase function in paraxial approximation:

$$U_3'(x_3) = U_3(x_3)\exp\left[-j\frac{k}{2f}x_3^{\ 2}\right] \tag{2.60}$$

The same formulation for propagation through the lenses is used throughout this work. When this field is substituted into the Fresnel equation given in (2.10):

$$U_{im}(x_{im}) = e^{j\frac{k}{2z}x_{im}^2}\int_{-\infty}^{+\infty} U_2'(x_3)e^{j\frac{k}{2z}x_3^2}e^{-j\frac{k}{z}x_3x_{im}}dx_3 \tag{2.61}$$

Note that, multiplicative constant terms are not considered in the analysis. Since the beam is propagated by a focal distance (i.e., z=*f*), the quadratic exponential cancels with the one in (2.60):

$$U_{im}(x_{im}) = e^{j\frac{k}{2f}x_{im}^2}\int_{-\infty}^{+\infty} U_3(x_3)e^{-j\frac{k}{f}x_3x_{im}}dx_3 \tag{2.62}$$

The integral is equivalent to a Fourier transform operation:

$$U_{im}(\frac{x_{im}}{\lambda f}) = e^{j\frac{k}{2f}x_{im}^2}\mathcal{F}(U_3(x_3)) \tag{2.63}$$

Considering only the intensity in the image plane, the phase term preceding the integral is removed, and intensity in the image plane, *I* is found to be:

$$I = \left|\mathcal{F}(U_3(x_3))\right|^2 \tag{2.64}$$

Alternatively, the same result can be obtained using the Fraunhofer approximation, which is valid for $z >> \frac{k\Delta x_0^2}{2}$ [16]. In that case, the quadratic phase factor under the integral of the Fresnel equation $\exp(j\frac{kx_{1\max}^2}{2z})$ is approximated to be unity and equation (2.62) can be obtained. Since the field, behind the lens $U_2(x_1)$, is focused, the field can be considered to be propagating to z→∞ and the Fraunhofer approximation can be applied.

Numerical implementation of the propagator equation (2.64) needs to be evaluated to ensure the numerical accuracy. The propagation of the field is implemented with a single integral operation and that cause a scaling of the coordinate axis. Wigner functions W_0 and W_z [17] respectively of the field $U_3(x)$, and the field in the image plane $U_{im}(x)$, reveal that the later is a sheared version of the former one [18] The shearing of the function results an increase in x-axis width Δx. As a consequence, it can be shown that the aperture of the beam extends according to:

$$\Delta x_z = \Delta x_0 + \lambda z \Delta \xi_z \tag{2.65}$$

Sampling of the integral requires additional attention. Under-sampling of the function inside the integral has to be avoided. $U_3(x)$ is a nearly plane wave so the phase change across the plane is negligible. The phase change of the exponential term, between consecutive integration steps is the main source of concern for the evaluation of the numerical accuracy.[19] In order to sufficiently sample the function inside the integral, phase change $d\phi$ of the exponent term in two consecutive sampling (separated by δ), has to be smaller or equal to half the period of the function *exp(-jϕ)*; i.e., $d\phi$ should be smaller or equal to π:

$$d\phi = \frac{k}{z}[(x_0 + \delta)x_z - x_0 x_z] \leq \pi \tag{2.66}$$

where terms with x_0 cancels out. To consider the extreme case, by substituting extreme value of x_z (i.e., $\Delta x_z/2$) and using equation (2.59), one would get:

$$z \geq \frac{2\Delta x_z^{\ 2}}{\lambda N} \tag{2.67}$$

and equivalently, using the equation (2.65) the expression for minimum value of z for far-field propagation to be implemented free from sampling errors is found to be:

$$z \geq \frac{\Delta x_0^{\ 2}}{\lambda N} \tag{2.68}$$

2.4.2. Limits of the Fresnel Propagation

In the first propagation step, the beam is propagated through the MLAs. The beam is focused by the MLA1 to an array of spots on the MLA2 and then propagated to the MLA3. In section 2.3, the analysis of each three-microlens channel is carried out separately and the interaction (i.e. diffraction) between these beam segments is not considered. Now, a complete beam propagation using an array of microlens channels needs to be performed to illustrate the diffraction effects. For that purpose, direct implementation of the Fresnel propagation is investigated. For convenience, (2.10) is repeated here:

$$U_z(x_z) = \frac{e^{jkz}}{j\lambda z} e^{j\frac{k}{2z}(x_z^2)} \int_{-\infty}^{+\infty} U_0(x_0) e^{j\frac{k}{2z}x_0^2} e^{-j\frac{k}{z}(x_0 x_z)} dx_0 \qquad (2.69)$$

where $U_0(x_0)$ is the field after the MLA1 and composed of an array of lens phase functions. So, the simplification which appears in equation (2.15) does not appear here, and the quadratic phase function inside the integral does not cancel out.

Sampling of the integral requires additional care, such that the phase change, $d\phi$, of the exponent, between two consecutive integration steps, need to be smaller or equal to half the period of the exponential function inside the integral, defined as $exp(-j\phi)$:

$$d\phi = \frac{\pi}{\lambda z}[(x_0+\delta)^2 - x_0^2 - 2x_z(x_0+\delta) + 2x_z x_0] \le \pi \qquad (2.70)$$

Equivalently in a simpler form:

$$2x_z\delta - 2x_0\delta - \delta^2 \le \lambda z \qquad (2.71)$$

The term δ^2 is small and can be neglected. The equation has to be fulfilled for all x values. So, considering the extreme case, by substituting $\Delta x_z/2$ for x_z and $-\Delta x_0/2$ for x_0 the inequality becomes:

$$(\Delta x_z + \Delta x_0)\delta \le \lambda z \qquad (2.72)$$

And using equations (2.59) and (2.65) one would get:

$$z \geq \frac{2\Delta x_0^{\ 2}}{\lambda N} \tag{2.73}$$

Using the system definition given in the Table 2.1 and the equation (2.73) the minimum z distance for which the Fresnel propagation can be implemented free from sampling related numerical errors can be calculated to be 6.3 mm using the system parameters in Table 2.1. Thus, the minimum microlens $f_{\#}$, that can be simulated using Fresnel propagation, can be found to be 63; however we are interested in simulating lenses with $f_{\#}$ < 8 and f<800μm. Therefore, Fresnel propagation can not be numerically implemented for accurate simulation of such a system. Another method is needed for propagation through MLAs. For that purpose we evaluate numerical implementation of plane wave propagation method.

2.4.3. Plane Wave Propagation (PWP)

Plane wave propagation method, is based on decomposition of the beam into the plane wave components by a Fourier transform operation and free space propagation of each plane wave by a phase multiplication. Fourier transform operator is repeated here:

$$\mathcal{F}\left[U_2(\frac{x_2}{\lambda z})\right] = \int_{-\infty}^{+\infty} U_2(x_1) e^{-j\frac{k}{z}x_1 x_2} dx_1 \tag{2.74}$$

As discussed in [16] Fourier transformation of a beam is equivalent to separation of the beam into the plane waves propagating with direction cosines (α,β,γ). So the Fourier transformation equation can be expressed as:

$$A(\frac{\alpha}{\lambda},0) = \mathcal{F}\left[U(x,0)\right] = \int_{-\infty}^{+\infty} U(x,0) e^{-j2\pi\frac{\alpha}{\lambda}x} dx \tag{2.75}$$

After propagation of plane wave components, the beam is reconstructed by an inverse Fourier transformation, given by:

$$U(x,z) = \mathcal{F}^{-1}\left[A(\frac{\alpha}{\lambda}, z) \right] \tag{2.76}$$

$$= \int_{-\infty}^{+\infty} A(\frac{\alpha}{\lambda}, z) e^{+j2\pi\frac{\alpha}{\lambda}x} d\frac{\alpha}{\lambda} \tag{2.77}$$

The propagator phase function which needs to be multiplied with the plane waves can be found by substitution of (2.75) into the Helmholtz equation given by: [16]

$$\Delta^2 U + k^2 U = 0 \tag{2.78}$$

The propagator phase function can be found as: $\exp(jk\sqrt{1-\alpha^2}z)$.[16] So the equation for free space propagation of the decomposed plane waves can be expressed as

$$\mathcal{F}(\mathrm{U}(\mathrm{x}_z)) = \mathcal{F}(\mathrm{U}(\mathrm{x}_0))\exp(jk\sqrt{1-\alpha^2}z) \tag{2.79}$$

The square term can be approximated by the first two terms of binomial expansion, yielding $\sqrt{1-\alpha^2}$ = 1 - α^2 / 2. Using spatial frequency defined as $\xi=\alpha/\lambda$, instead of direction cosines α, (2.79) can be expressed equivalently as:

$$\mathcal{F}(\mathrm{U}(\mathrm{x}_z)) = \mathcal{F}(\mathrm{U}(\mathrm{x}_0))\exp(jkz)\exp(-j\pi\lambda z\xi^2) \tag{2.80}$$

Note that, alternatively, (2.80) can be obtained by Fourier transformation of the Fresnel equation in the convolution form, given in (2.7).

Finally the propagated plane waves are reconstructed by an inverse Fourier transform operation of $\mathcal{F}$(U(x_z)) given in (2.80) to obtain the field distribution at the z plane:

$$\mathrm{U}(\mathrm{x}_z) = \mathcal{F}^{-1}\left\{ \mathcal{F}\left[\mathrm{U}(\mathrm{x}_0)\exp(jkz) \right] \exp(-j\pi\lambda z\xi^2) \right\} \tag{2.81}$$

Evaluation of numerical implementation of (2.81) reveals similar constraints to the simulated system as in (2.73), but in a different way. The phase difference of the exponent term in (2.81), between two consecutive integration steps shouldn’t exceed π. Such that:

$$\pi\lambda z[\xi^2 - (\xi - d\xi/2)^2] \le \pi \tag{2.82}$$

Neglecting the $(d\xi)^2$ term, and using the relations in (2.59) the condition for accurate numerical implementation of the equation (2.81) is found to be:

$$z \leq \frac{2\Delta x_0^{\ 2}}{\lambda N} \tag{2.83}$$

The constraint for numerical accuracy of plane wave propagation method is similar to the constraint given in (2.73) for Fresnel propagation method. Both methods are bounded by the same critical distance $z_c = \frac{2\Delta x_0^{\ 2}}{\lambda N}$. The only difference is that the propagation distance z is bounded to be lower than z_c for plane wave propagation method and whereas for Fresnel propagation method z is bounded to be higher than z_c.

Using the system parameters given in Table 2.1 and (2.83) the maximum z distance for which the plane wave propagation can be implemented free from numerical errors is found to be 6.3 mm. So the microlens $f_{\#}$ is limited to be below 63. That fits with our interests. So, plane wave propagation method is used for simulation of beam propagation through the MLAs.

A last note on propagation methods, one might notice that angular beam propagation method is used for short distances and when the phase functions vary rapidly, and the far-field propagation is used for long distances and when the phase function vary slowly. This is why, propagation through an array of microlenses requires plane wave propagation method and far-field propagation method fits for focusing of the beam to the image plane by single lens.

2.4.4. Simulation Results

The system defined in the Table 2.1 is simulated using the simulation methods discussed above. Plane wave propagation method is used for propagation through the MLAs and far-field propagation method is used for propagation to the image plane after

MLAs. In this section, system simulations are reported in order to demonstrate the phase conditions given in Section 2.2.

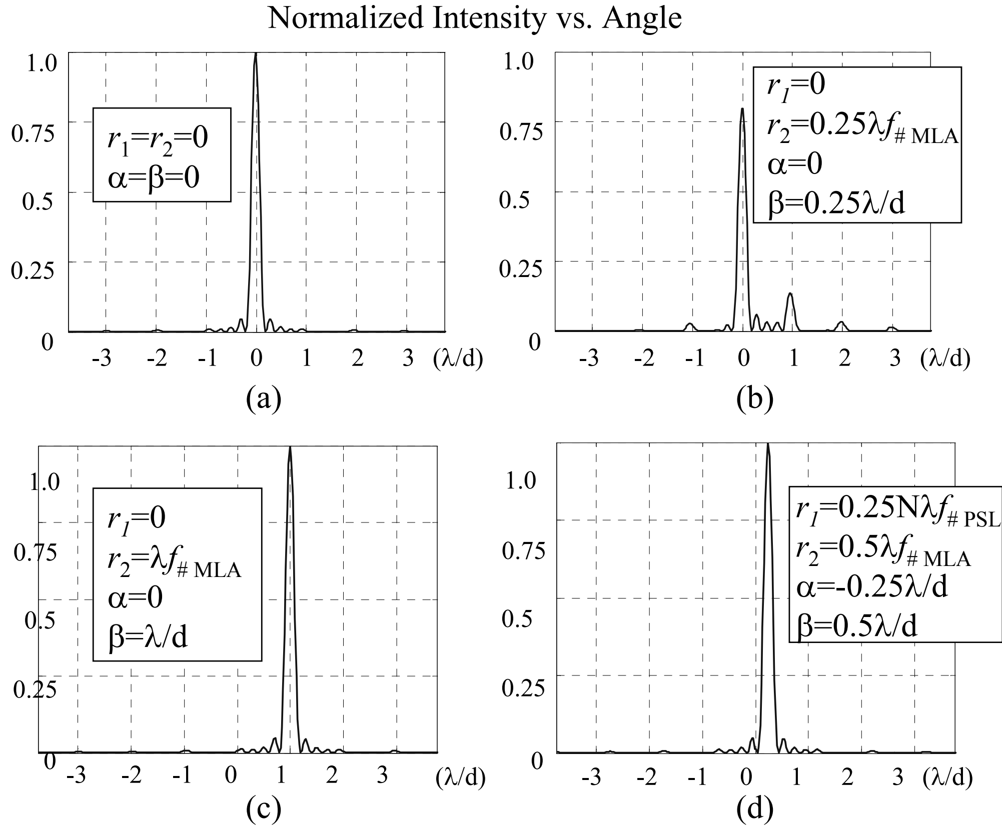

Figure 2.9: Simulated PSF for different amounts of the PSL and the MMLA displacements (r_1 and r_2) and the resultant beam tilt angles α and β. (a), (c), and (d) illustrate constructive beam interference (phase condition is met) and (b) illustrate destructive interference (phase condition is not met).

Figure 2.9 is simulation of the PSF in normalized angular coordinate system for plane-wave illumination. The MLAs in the simulated system are spherical, square-packed, and have 100% fill-factor. The anglar spacing between diffraction orders is λ/d, so the grid in the horizontal direction represents the diffraction order positions with no PSL displacement. As can be seen in the figure, addressing of a position between two diffraction

orders is not possible without the displacement of the PSL. The beam can be positioned at the diffraction order angles as in the Figure 2.9.a and Figure 2.9.c by displacement of MMLA alone. However, intermediate points can not be addressed by mere displacement of the MMLA as can be seen in Figure 2.9.b. Note that the centroid of the beam is at the desired intermediate location but the PSF is split into two parts as the phase condition is not met. A combined motion of the PSL and MMLA which fulfills the phase conditions given by (2.5), can address an intermediate position as seen in Figure 2.9.d.

Taking a closer look at the Figure 2.9, in the Figure 2.9.b, $\theta_T=0.25\lambda/d$ and OPD=0.25λ, therefore the phase condition is not met and the resultant PSF is split between two diffraction orders. Whereas in Figure 2.9.d when α and β are properly selected to meet the phase condition, a constructive PSF at an intermediate angle $\theta_T=0.25\lambda/d$ is obtained. Note that the position of the intensity center is determined by the θ_T and the deflection of the intensity peak from the intensity center position is determined by the ϕ_T.

2.5. Experimental verification

The PSF of the system for selected values of the PSL and the MMLA's displacements is shown in Figure 2.10. It demonstrates the addressing of positions between discrete diffraction orders. This figure also illustrates the relation between the PSF and the phase condition given in (2.5), e.g., a single peak appears wherever the phase condition is fulfilled. As it was illustrated in Figure 2.9.b and Figure 2.9.d, the scan angles that are not addressable by the MMLA motion alone can be addressed with the combined motion of the MMLA and the PSL. Experimental results verify that the PSL's motion scans both the entire diffraction grid and the centroid of the PSF by the same amount but in opposite directions, which can be verified using (2.2) and (2.3). Whereas the MMLA motion moves only the centroid of the intensity pattern while the diffraction grid stays stationary.

In summary, the results derived by physical intuition in Section 2.1 and 2.2 are successfully proven in latter sections by using Fourier optics theory, numerical simulations, and experimental results. Optical system design and system level demonstrations are the focus of the next chapter.

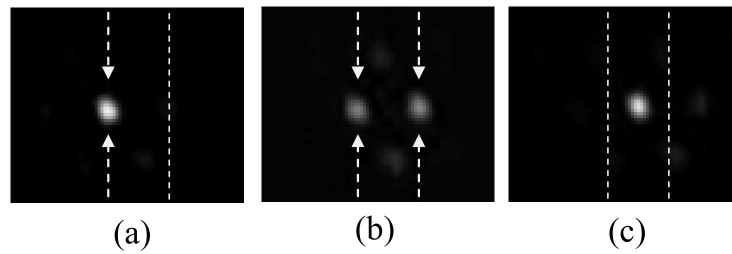

Figure 2.10: Experimental results for the MMLA and the PSL's motion. (a) All lenses on-axis, (b) Only the MMLA is moved to steer beam by half diffraction angle (phase condition not met); (c) Both the PSL and the MMLA is moved to steer the beam by half diffraction angle (phase condition met);

CHAPTER 3

OPTICAL SYSTEM DESIGN

3.1. Introduction

In designing an imaging system, generally speaking, resolution of the system is the uttermost important system performance criterion. Resolution of a system is defined as the number of resolvable spots at the image plane, and can be determined by the ratio of the maximum scan angle and the angular spot size. When detector limitations or the image quality are considered, resolution of a system has to be considered as a function of contrast level. A more encompassing performance criterion for assessing resolving power of an imaging system is the modulation transfer function (MTF). MTF describes the ability of a system to transfer object contrast to the image as a function of spatial frequency, i.e. as a function of system resolution.

As discussed in Chapter 2 the PSF of the system is composed of a main lobe and side lobes positioned at neighboring diffraction order positions. In determination of the system resolution merely angular spot size of the main lobe can be used. However side lobes have to be considered as well, as they degrade the image contrast. For assessing the imaging performance of the MLA scanners MTF is used as the criterion.

MTF of the system is mainly dependent on the maximum resolution of the system and fraction of the energy at the main lobe. The optical intensity outside the main lobe degrades the contrast of the imaging and degrades the MTF. The amount of energy in the sidelobes is related to aberrations in the system and the fill-factor obtained on the MLA3. MTF of the system can be shown to be Fourier transform of the PSF of the system. [21] The maximum resolution of the system is a function of the system parameters such as beam diameter, $f_{\#, MLA}$ and wavelength of operation. [22] In the imaging system attainable contrast levels (i.e.

MTF) is determined by the aberrations in the system and the low fill-factor. Fill-factor can be defined as the ratio of the beam size at an aperture and the aperture size.

In this chapter performance of the MLA scanning system is evaluated. For evaluation a built in house physical optics propagation simulator and a commercial ray tracing tool ZEMAX™ is utilized. Using these tools, an optimization scheme which considers both diffraction of the beamlets and aberrations in the system is developed.

In this chapter for the imaging performance analysis of the system, simulation and optimization results obtained by physical and ray optics simulators are reported. In Section 3.2, the maximum aberration free resolution of the system is given. In Section 3.3, imaging performance related to MLA fill-factor and profile. In Section 3.4, optimization of the system is reported. In Section 3.5, performance of the experimental system is reported. Methods for MLA fabrication are discussed in Section 3.6.

Note that through the analysis, operation wavelength is 632nm and microlens size is 100µm and if not otherwise specified number of lenses in the MLAs is four.

3.2. Resolution analysis

For a converging Gaussian beam that goes through a system aperture of width D and focused at a distance f from the aperture, the diffraction-limited (i.e., aberrations neglected) angular spot size s_θ in the paraxial regime can be expressed as:

$$s_\theta = K\lambda / D \tag{3.1}$$

where K is a beam constant that incorporates the beam profile and Gaussian beam clipping effects and the assumptions related to the system design such as amount of overlap between adjacent pixels. [24] The maximum scan angle measured from the optical axis, θ_{max}, is equal to $D/2f$ so, the number-of resolvable spots (N_R) that can be obtained by this scanning system can be expressed as:

$$N_R = \frac{2\theta_{\max}}{s_\theta} = \frac{2D\theta_{\max}}{K\lambda} = \frac{D}{K\, f_{\#MLA}\,\lambda} \tag{3.2}$$

Note that the resolution is independent of the focus distance and the same result can be obtained by taking the ratio of the produced scan line length to the spot size.

Table 3.1 shows the system resolution as a function of system parameters assuming diffraction limited performance. Note that, in the calculation uniform beam illumination is assumed that is truncation ratio, *T*, defined by the ratio of beam and aperture sizes, is assumed to approach infinity, i.e., T→∞. The K factor in (3.2) is calculated to be 1.036 using the following equation: [24]

$$K_{FWHM} = 1.036 - \frac{0.058}{T} + \frac{0.156}{T^2} \tag{3.3}$$

Maximum resolution of 2300 pixels in each axis can be achieved with 3mm clear aperture and *f/2* microlenses using the assumptions and the formulas in Reference [26].

D (mm)	$f_{\#,MLA}$	*d* (mm)	*# of μlenses*	$r_{1,\max}$ (μm)	$\theta_{\max}$ (mrad)	N_R
2	4	0.1	20	± 19	± 125	768×768
2	2	0.1	20	± 19	± 250	1536×1536
2	4	0.2	10	± 9.5	± 125	768×768
3	4	0.1	30	± 28.5	± 125	1152×1152
3	4	0.2	15	± 14	± 125	1152×1152
3	3	0.1	30	± 28.5	± 167	1536×1536
3	2	0.1	30	± 28.5	± 250	2304×2304

* Assumptions: uniform laser beam illumination (T→∞); λ=632nm HeNe laser illumination; Adjacent spots overlap at full-width half-maximum; $f_{\#,PSL}$ =3

Table 3.1: MLA beam steering system parameters and the system resolution.*

3.3. Array fill-factor and diffraction analysis

The MLA scanning system consists of a periodic array of microlenses. After propagation through the MLAs the beam is segmented into an array of beamlets and mainly the interference of these beamlets determine the shape of the PSF. In this section physical optics simulation of the system with different unit cells are reported. The performed simulations are implemented as discussed in Section 2.5.

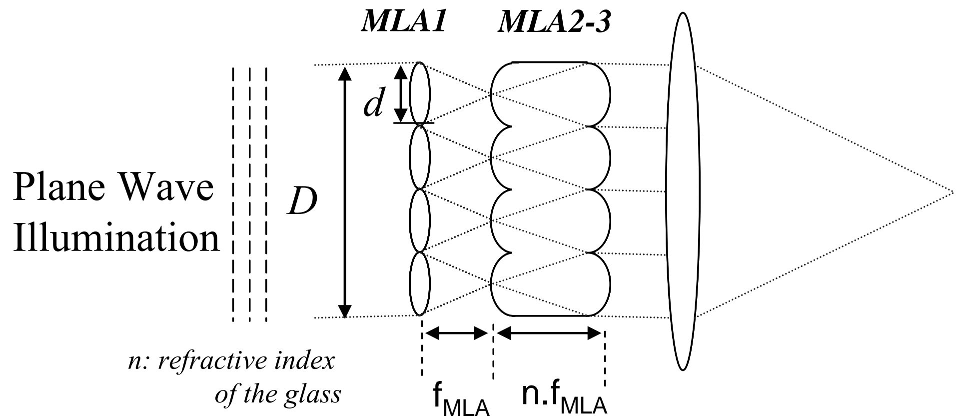

Figure 3.1: Simulated laser beam steering system for diffractive performance evaluation (MLAs are identical and the focusing lens is an ideal Fourier lens)

In the simulated system all the microlenses have square shape and spherical profile and the number of microlenses is limited to 4x4 arrays. Beam width (D) is 400μm and microlens pitch d=100μm. In the analysis that follows, the Strehl ratio (*V*) is often used as a figure of merit for evaluation of the imaging performance. *V* is defined as the ratio of the peak intensity of an image to that of an aberration free image and a system is typically considered diffraction-limited if the $V > 0.8$.

As explained in Figure 3.2 caption, four different types of refractive MLAs are simulated in the beam steering system and the corresponding PSFs are compared. Note that, the intensity is normalized with respect to the peak intensity of case (i) where microlenses are omitted from the system and only the diffraction limited imaging lens is

present. Notice that secondary peaks (or side lobes) appear and the peak intensity degrades for different types of microlenses analyzed. As it is seen in the Figure 3.2, magnitude of the peak intensity degrades, when low fill factor MLAs in case (iii) are employed rather than high fill-factor MLAs in case (ii). Also the relative intensity of the secondary peak compare to the primary intensity peak in low fill-factor in case (iii) is nearly one-fourth of that of the high fill-factor MLAs in case (ii). Notice that in case (iv), spacing between microlenses is introduced to mimic the microlenses fabricated by the photoresist reflow method, which is discussed in Section 3.6.3. The PSF of a system utilizing this kind of MLAs has more energy in higher diffraction orders, and hence the peak intensity diminishes.

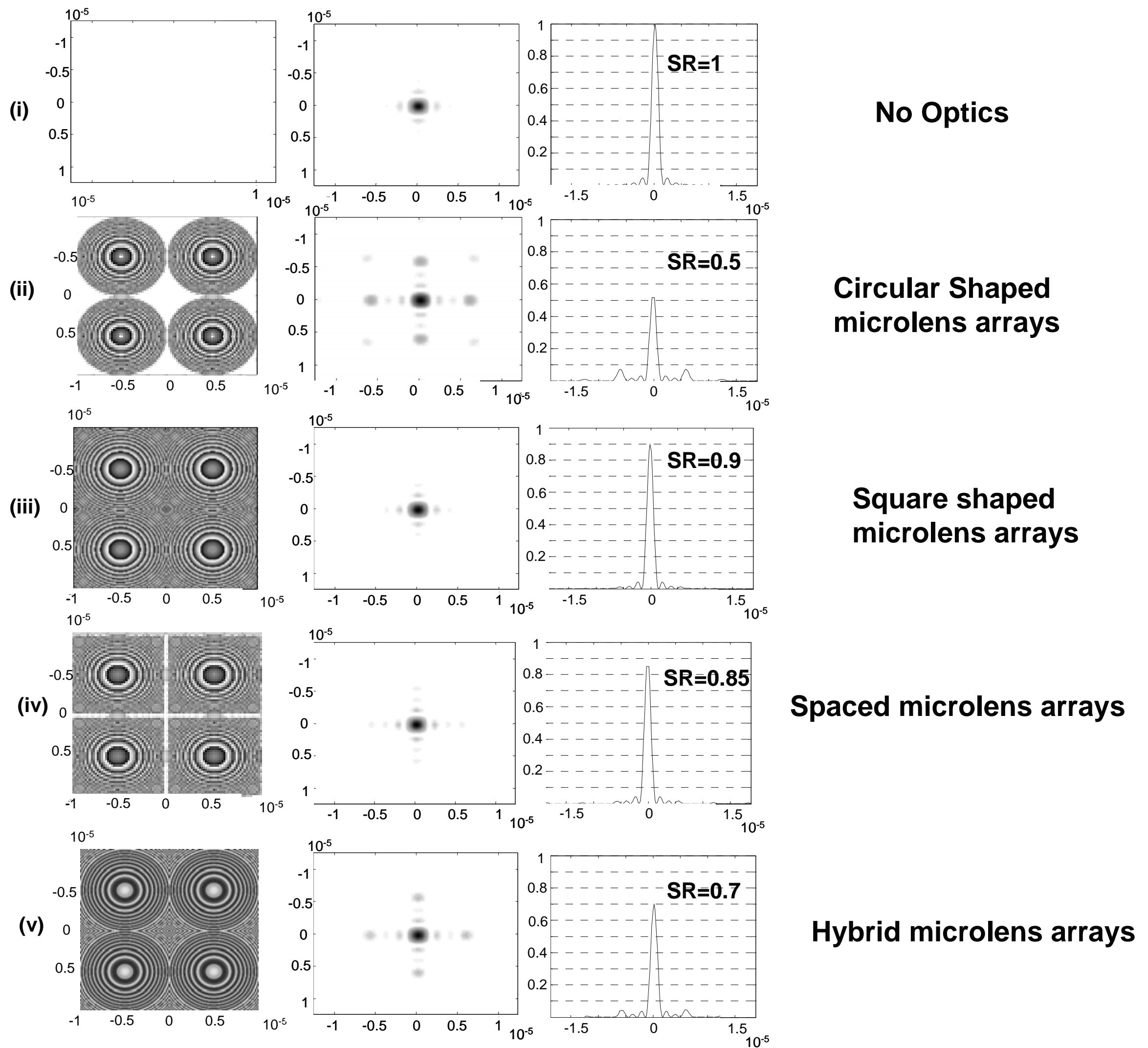

Figure 3.2: Lens Phase functions and corresponding PSF figures of refractive lenses with (i) no-optical elements (ii) circular shaped MLAs (%78 fill-factor), (iii) perfect fill-factor (%100), (iv) spaced (%93 fill-factor), (v) hybrid-diffractive (%100) [f : 6]

Performance degradation is related to the focusing efficiency of the MLAs and low efficiency MLAs cause greater inter-channel coupling (i.e., beam strays to a neighboring microlens after propagation through three-microlens in the MLA system).

In addition to refractive microlenses with continuous phase profiles, there are also diffractive-type microlenses, which are implemented by several photolithography steps and have stair-step like discontinuous phase profiles. Various fabrication methods for both types of microlenses and a third hybrid approach will be discussed in Section 3.6.

For the diffractive MLA case, the beam is highly scattered and overfills the aperture of the last lens surface, which results in inter-channel cross-talk.

In Figure 3.3 Strehl ratios (V) of refractive andwd diffractive lenses with 100% fill-factor are compared. Four types of diffractive lens phase functions are simulated: (i), (ii) Ideal 16-level and 8-level MLAs (iii) 16-level MLA (with a critical dimension (CD) of 1μm), and (iv) Hybrid-diffractive MLA (with a CD of 1 μm). As discussed in Section 3.6.2, the minimum resolvable feature size or the CD imposes a limitation on the number of resolvable phase levels. Hence, in some regions of the lenses the number of phase levels decreases. Refractive lenses perform diffraction limited (V>0.8) for at $f_{\#}$ >4. The Strehl ratio is below 0.8 for low $f_{\#}$ lenses due to spherical aberrations. The 16-level and 8-level diffractive lenses perform as good as the refractive lenses with only 2% and 6% decrease in the Strehl ratio. The performance degradation is due to the low diffraction efficiencies of diffractive lenses which are theoretically 99% for 16-level and 97.4% for 8-level lens. [23] Hybrid lenses, which have a refractive lens profile at the center area and diffractive lens profile in the corners, perform better than fully-diffractive lenses because of their higher diffraction efficiency that is related to their refractive dominant structure.

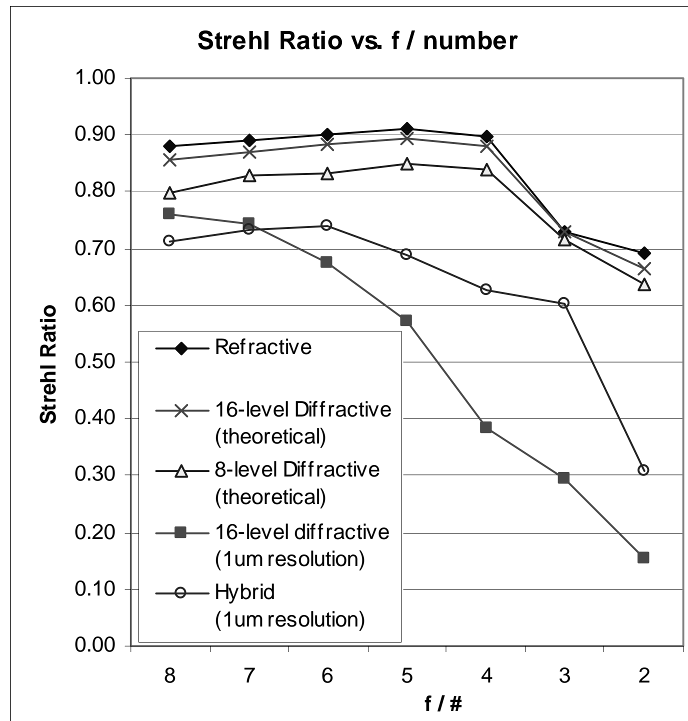

Figure 3.3: Imaging performances of the lenses are compared

As illustrated in Figure 3.4, alignment tolerances and resolution of the lithography limit the number of phase levels that can be fabricated. Particularly at the edges of low $f_{\#}$ lenses, number of resolvable levels decreases down to 2. Because of the limited resolution of the fabrication process and decrease in the number of resolvables phase levels as a function of $f_{\#}$, the diffraction efficiencies of low $f_{\#}$ lenses are fairly low, as illustrated in Figure 3.5. Furthermore, at the corners of low $f_{\#}$ lenses, no phase steps can be fabricated. In Figure 3.5, diffraction efficiency as function of $f_{\#}$ is plotted for a single 16-level diffractive lens. This limitation results with nearly 50% degradation in the Strehl ratio of the lenses as previously illustrated in Figure 3.3.

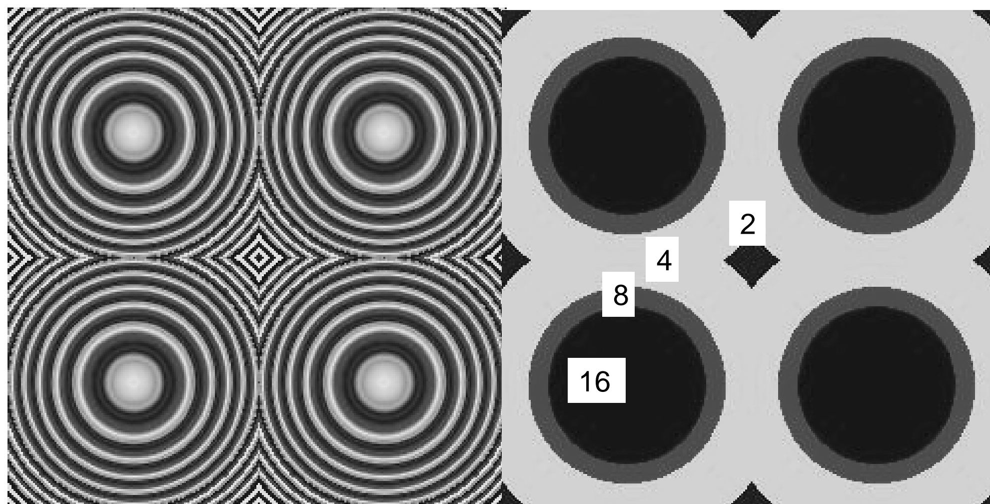

Figure 3.4: Sections of an f / 6 lens designed in 16-8-4-2 phase levels by considering 1 m resolution limited fabrication process

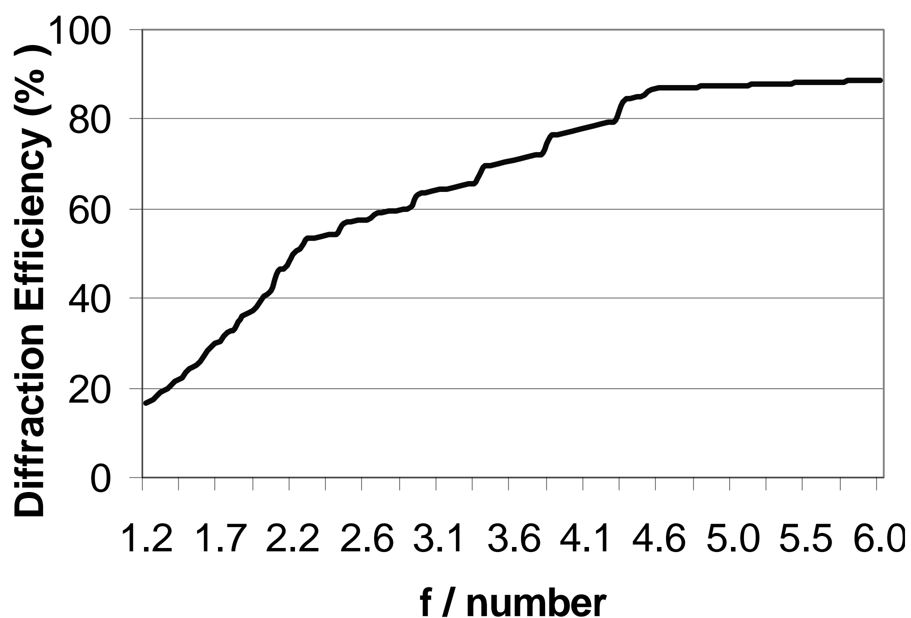

Figure 3.5: Diffraction efficiency vs. f# for circular 16-phase-level diffractive lenses

Generally speaking, diffractive lenses are designed for a single wavelength operation, however, due to variations in the etch-depth during fabrication; the fabricated parts could

be slightly sub-optimal for the design wavelength. The focusing performance degrades greatly when diffractive lenses are operated at a wavelength other than the design wavelength or when there is a mismatch between the design and the fabricated parts. As demonstrated in Figure 3.6, the Strehl ratio degrades by 60% when operated at a 3% shifted wavelength. Whereas, when hybrid lenses is employed in the system, the Strehl ratio degrades at most by 45% and fluctuates as a function of wavelength. This is mainly due to distribution of optical focusing power, and refractive dominant nature of the combined structure. Therefore, hybrid microlenses show some promise compared to diffractive lenses to fabrication tolerances and shifts in the operation wavelength.

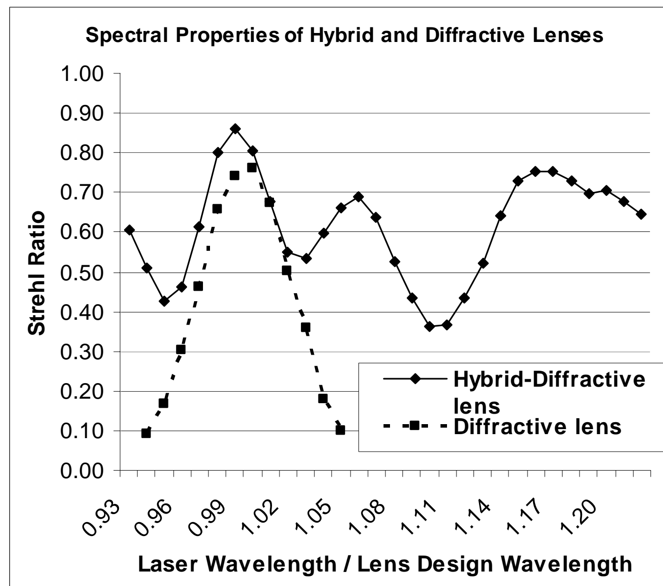

Figure 3.6: Wavelength depended performances of fully- and hybrid-diffractive MLAs in beam steering system

3.4. Optimization of the optical system

3.4.1. The PSF of the aberrated system

MLA beam steering systems are telescopic systems, and array of collimated beamlets are output from an array of microlenses. The far-field pattern is the result of interference of these beamlets. Scanning is obtained by tilting of the individual beamlets and satisfying the phase condition between the beamlets by utilizing a pre-tilting lens prior to the telescope system.

The telescopic system can be analyzed as identical channels which are composed of a train of three microlenses. For the convenience of the analysis without loss of generality we analyze the system in one dimension. Extension of the analysis into two dimensions is straightforward. The transmission function of the system can be shown to be a periodical phase function given as:

$$t(x) = \left[\exp\left(-ik\mu(x)\right)\mathrm{rect}\left(x/a\right)\right] * \left[\left(1/d\right)\mathrm{comb}\left(x/d\right)\mathrm{rect}\left(x/D\right)\right] \quad (3.4)$$

the parameters and mathematical functions in the equation are defined in Figure 1 and the Appendix.

The field distribution -i.e. the point spread function (PSF), at the image plane is the Fourier transform of the *t(x)*. PSF can be expressed as:

$$I(\theta) = \left(Nad\right)^2 \left[\mathcal{F}\left[\exp\left(-ik\mu(x)\right)\mathrm{rect}\left(x/a\right)\right] \times \left[\mathrm{comb}\left(d\sin\theta/\lambda\right) * \mathrm{sinc}\left(D\sin\theta/\lambda\right)\right]\right]^2 \quad (3.5)$$

The first part of the equation forms an envelope (I_1) and the second part is a train of Sinc functions (I_2), as shown in Figure 3.7. If there is no aberrations (i.e. $\mu(x)$=0), and the intensity distribution is uniform, the Fourier transform simplifies to $\mathrm{sinc}\left[\left(d/\lambda\right)\sin\theta\right]$, and the zeros of the I_1 overlaps with the higher order diffraction peaks of I_2 and cancels. In case of aberrations and/or non-uniform intensity distribution the envelope Sinc function denoted by I_1 widens and higher order diffraction peaks appears in the PSF, as illustrated in

Figure 3.7. Of interest is the systems that are moderately suffering from aberrations; for such systems most of the optical energy is inside the main lobe and distributed between the 0th and 1st order diffraction lobes. Optical energy in the higher diffraction order (>1) lobes can be neglected.

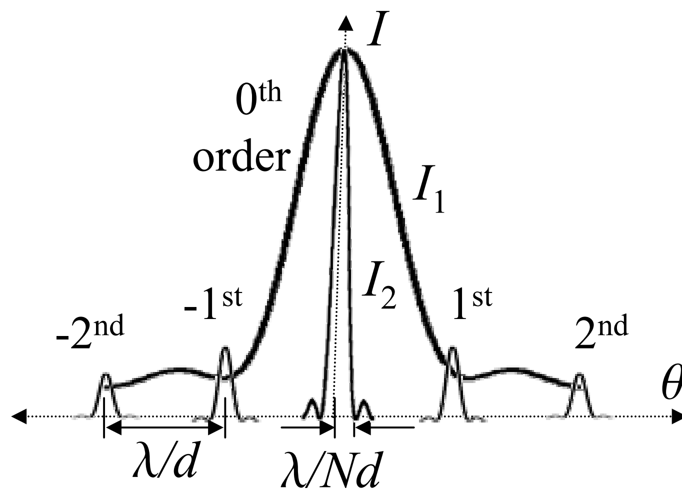

Figure 3.7: Illustration of the PSF formulated by periodical Sinc functions (I_2) multiplied by an envelope function (I_1)

Through the analysis it is assumed that the beamlets uniformly fills the last microlens apertures. Wave aberrations -denoted by $\mu(x)$, are analyzed as wavefront errors as a deviation from the reference wavefront at the output plane.

Resolution of the optical system can be determined by the total scan angle divided by the minimum angular spot size which is defined by the I_2 and approximately equal to $\sim\lambda/D$. Note that the spot size is independent of the aberrations and the fill-factor. Appearing aberrations and non-uniform intensity distribution cause a reshaping of the envelope function (I_1) and modifies the distribution of the optical energy between the diffraction orders. The field distribution pattern at a single diffraction order is simply the scaled far-field pattern of a full aperture beam ($\mathrm{sinc}(D\sin\theta/\lambda)$), and always size-wise diffraction

limited and magnitude-wise dependent on the aberration performance of the system. When the PSF is composed of a number of separated diffraction orders, resolution can not be simply determined by using the minimum angular spot size of the field in a single diffraction peak.

3.4.2. Optical performance analysis

MTF which is a quantitative measure of image quality in imaging systems, is far superior to any resolution criteria. It describes the ability of a system, to transfer object contrast to the image. MTF plots are handy in assessing the amount of spurious light (i.e. high order diffraction lobes) in MLA scanner systems.

MTF of a system is equivalent to autocorrelation of system transmission function t(x). Hence, for best system performance a perfectly uniform field is desired at the output. Deviations from the perfect uniform field can be analyzed separately as amplitude and phase deviations. In the cases of interest, the amplitude distribution is uniform so in the analysis only phase aberrations are considered.

Phase aberrations cause an increase in the contrast ratio which can be defined by the ratio of the magnitudes of the side and main lobe intensities. In an aberration suffering system the ratio of the magnitude of the central order and that of in aberration free system, is defined as the Strehl ratio (V). The lower the Strehl ratio the more optical power is distributed to the spurious lobes. Hence the Strehl ratio can be utilized as a measure for evaluation of the ratio of the optical energy distribution between the diffraction lobes. Furthermore there exists a simple relation between the RMS wavefront aberration and the Strehl ratio. The magnitude of the zeroth Fourier component of the optical field gives the Strehl ratio. Hence V can be expressed as:

$$V = \frac{1}{d^2}\left|\iint_A \exp(2\pi i\,\Delta W(x,y))\exp(-2\pi i(v_x x + v_y y))dxdy\right|^2 = \frac{1}{d^2}\left|\iint_A \exp(2\pi i\,\Delta W(x,y))dxdy\right|^2 \quad (3.6)$$

Using Taylor series expansion and neglecting third-order and higher-order powers of wave aberration ΔW, the equation simplifies to:

$$\begin{aligned} V &= \frac{1}{d^2}\left|\iint_A \left(1 + 2\pi i\,\Delta W + \frac{1}{2}(2\pi i\,\Delta W)^2 + ...\right)dxdy\right|^2 \\ &= \frac{1}{d^2}\left|\iint_A \left(1 + 2\pi i\,\Delta W + \frac{1}{2}(2\pi i\,\Delta W)^2 + ...\right)dxdy\right|^2 \\ &= \left|1 + 2\pi i\,\overline{\Delta W} - \frac{1}{2}(2\pi)^2\,\overline{\Delta W^2}\right|^2 \\ &= 1 - (2\pi)^2\left[\overline{\Delta W^2} - \left(\overline{\Delta W}\right)^2\right] \\ &= 1 - (2\pi\sigma)^2 \end{aligned} \quad (3.7)$$

where σ is the RMS wavefront error in units of waves and

$$\overline{\Delta W^n} = \frac{1}{d^2}\iint_A \Delta W^n dxdy \quad (3.8)$$

RMS wavefront error σ, is available as a simulation parameter in ray tracing optical design tools such as ZEMAX^{TM}. Hence, the Strehl ratio is very handy as a design parameter in optical system design and optimization.

3.4.3. Simulation and optimization of the system

Ray optics propagation is used for the analysis of beamlets' propagation through the train of three microlenses. In the propagation through the MLAs, diffraction and

interference can be safely neglected for the systems of interest (e.g., $f_{\#} \geq 2$). Assuming identical channels of microlenses and uniform illumination on the first MLA one can reduce the simulation of the system to simulation of a single channel of microlenses. The optimization merit function is formulated by using the Strehl ratio as the main design parameter. A commercial ray tracing tool ZEMAX™ is used for simulation and optimization of the wavefront phase error. Then, using the wavefront error data, a physical field is constructed. The system PSF is the Fraunhofer diffraction pattern of the field and can be simulated by a Fourier transform operation. In Figure 3.8 schematic view is given.

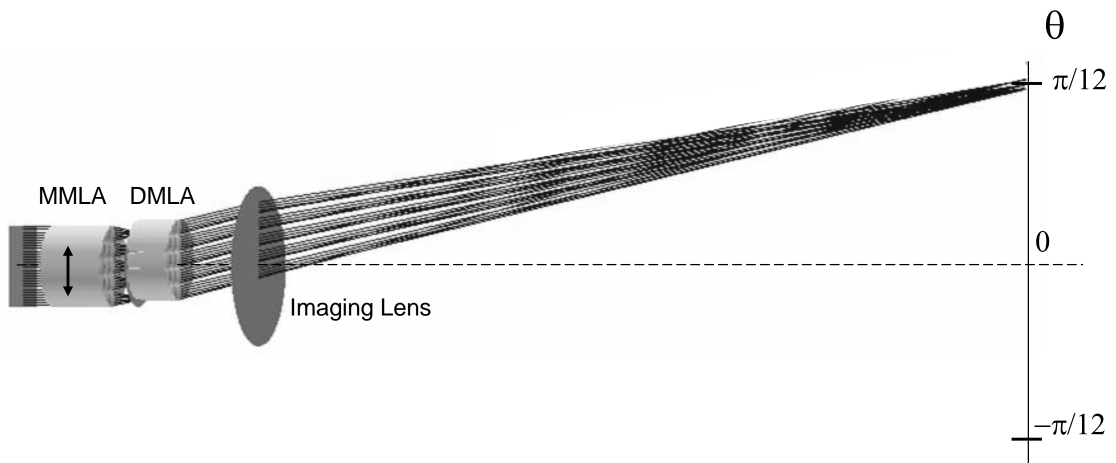

Figure 3.8: 3D schematic view of the simulated system utilizing f/2 MLAs.

Optimization of the optical system is carried out for f/2 and f/5; ashperical and spherical profile MLAs. The wavefront error, the PSF and the MTF plots are given in Figure 3.9, Figure 3.10, and Figure 3.11 , respectively. The resolution of the system at an acceptable contrast level can be determined by the spatial frequency corresponding to an MTF of 0.5, multiplied by the number of diffraction orders, $2d/\lambda f\#$. When the MTF is nearly diffraction limited then the realizable spatial frequency at the MTF of 0.5 is equal to the half the number of microlenses (N/2). As expected the multiplication is equal to the theoretical predicted resolution as formulated in (3.2). The simulated system utilizes 4×4

MLAs, since the resolution of the system is proportional to the array size, the simulation results can be scaled for any array size and can be used for demonstration of the resolution results given in Table 3.1. Note that, however, in theory, the resolution is directly proportional to the array size, in a practical point of view, uniformity and alignment of MLAs might be an issue, and limit the realizable resolution. We expect systems utilizing 30×30 MLAs are practical.

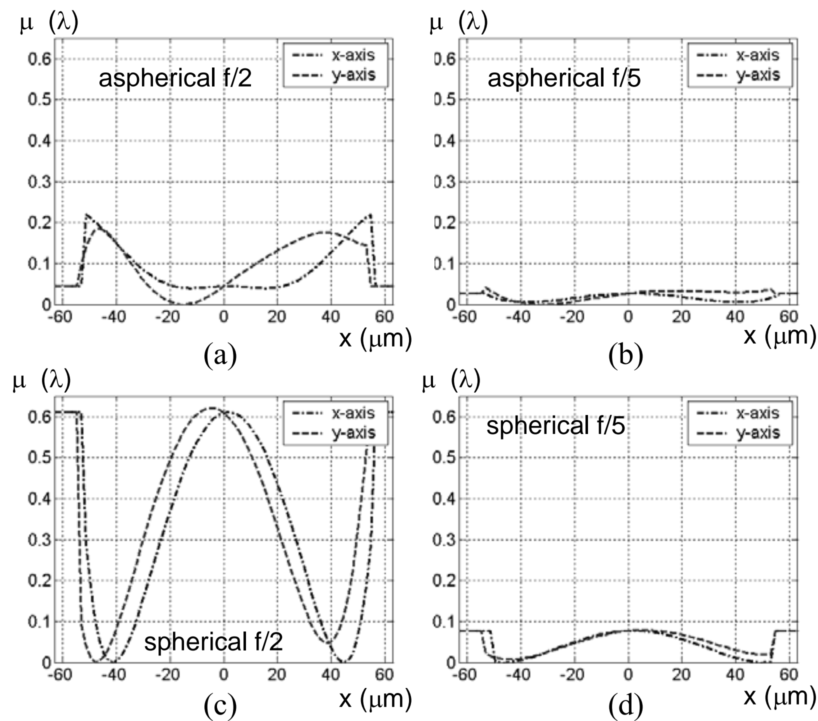

Figure 3.9: Wavefront aberrations plotted in x and y directions for the systems utilizing 100 μm pitched (a) aspherical f/2 (b) aspherical f/5 (c) spherical f/2 (d) spherical f/5 MLAs.

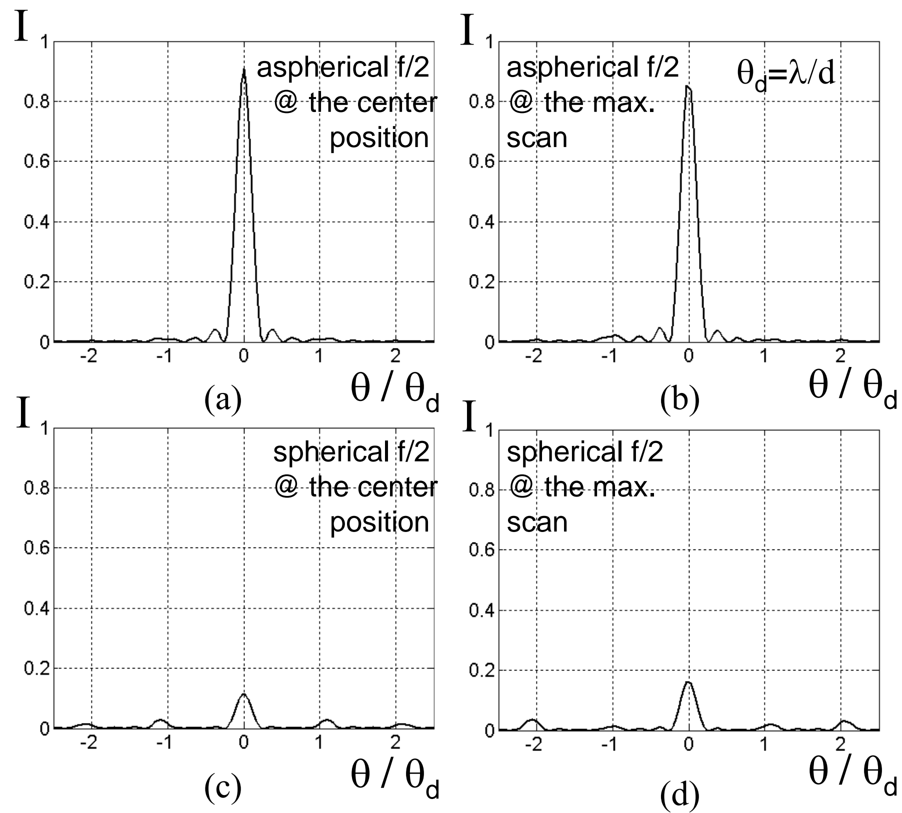

Figure 3.10: PSF cross-sections of the systems for (a) aspherical f/2 at the center position (b) aspherical f/2 at the max. scan angle position (c) spherical f/2 at the center position (d) spherical f/2 at the center position ($\theta_d=\lambda/d$)

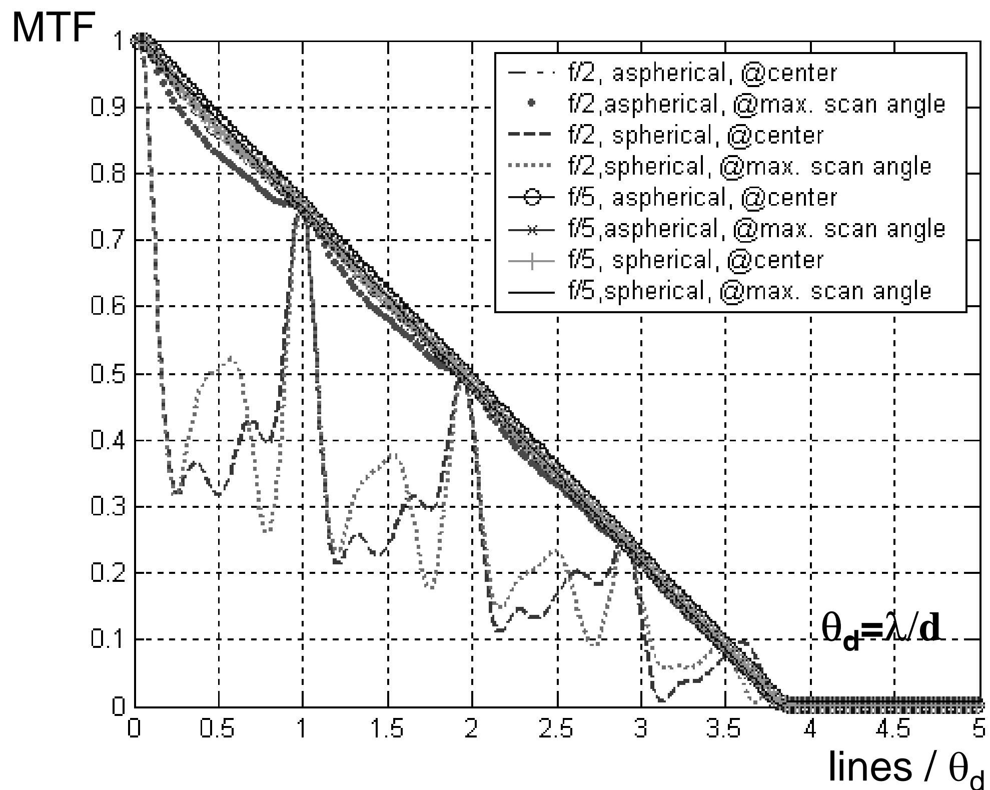

Figure 3.11: MTF plots for the systems of various configurations

3.5. The experimental setup

As discussed in Section 3.3, in order to get close to the theoretical diffraction limited resolution with low $f_{\#}$ microlens, lens profiles needs to be optimized for elimination/compensation of optical aberrations. However, one would achieve a resolution very close to the theoretical maximum, using high $f_{\#}$ spherical microlenses (e.g., $f_{\#}$ above 5). In this section, resolution of the system which employs *f*/5 spherical profile MLAs is evaluated experimentally. The MLA samples used in the experiment (Figure 3.12) are *f*/5, fabricated using isotropic etching and UV-casting method at Microvision Inc., and have

nearly 100% fill-factor and 200μm pitch. A green laser is used in the experiments (λ=0.532μm) and the beam size is around 600μm.

A full-system similar to shown in the schematic Figure 1.2 was built as shown in Figure 3.13 by placing both the PSL and the MMLA on moving magnetic actuator stages (Figure 3.14) which are taken out from a CD read/write head.

In the experimental setup MLA2 and MLA3 are bonded to each other. Alignment of these two MLAs requires precise positioning of one with respect to the other with very tight tolerances in all 6 degrees-of-freedom. UV-curable epoxy is placed between the MLAs and once the alignment is achieved the UV is cured. The right alignment of the MLAs is determined by observing the far-field pattern by shining a laser on the MLAs. The technique was developed by Urey and explained in Ref. [20]. The far-field pattern of one focal distance separated perfectly aligned MLAs is simulated in Figure 3.15. For verification of the method one can use the formulation in reference 8. The number of diffraction orders in one dimension (i.e., spots) N_{order} should be equal to:

$$N_{order}(\lambda)=d/\lambda f_{\#,MLA} \tag{3.9}$$

For λ=0.632μm d=100μm and $f_{\#,MLA}$=4, N_{order} is calculated to be 39.5 and matches the number of diffraction orders along the line in the Figure 3.15.

In the setup two magnetic actuators are used for actuation of MMLA and PSL. (Figure 3.14). The actuators are controlled by a computer through a DAQ card. A five-axis positioning stage is used for manual alignment of the MMLA and DMLA. The beam from green semiconductor laser of wavelength 0.532 μm is used for illumination. In order to obtain a clean and large beam, the laser beam is passed through a spatial filter pinhole in a telescope setup. The beam is then illuminated onto the PSL on an actuator and passed through a diaphragm for adjusting the size of the beam. After passing through the three-MLA system the beam is focused onto a CCD plane by an objective.

Precise alignment of the MLAs is critical, requires 6-axis alignment of the MMLA with respect to DMLA and rotational alignment of the MMLA with respect to beam direction.

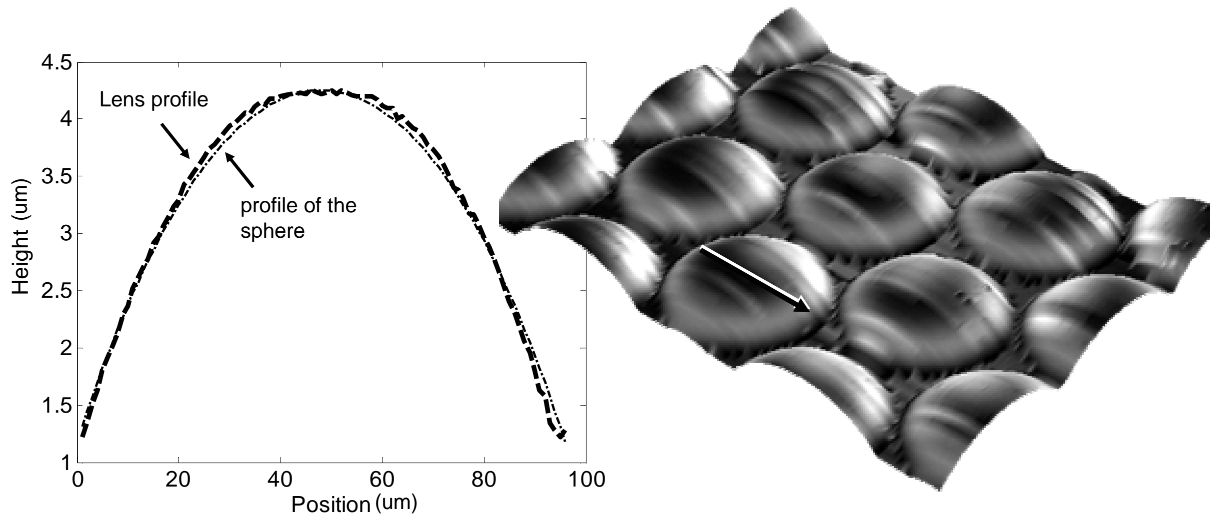

Figure 3.12: Profile of the MLAs used in the experiments. Plot of surface profile compared with the spherical profile and 3-D surface profile graph

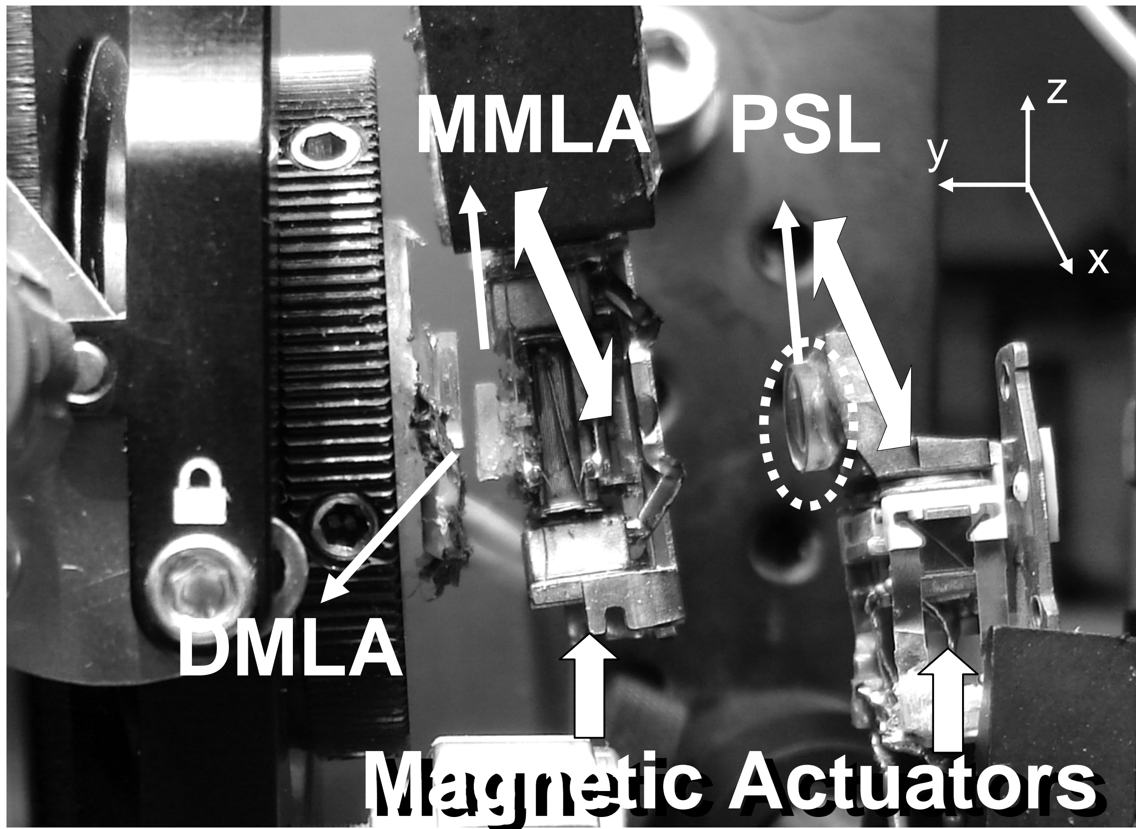

Figure 3.13: MLA laser scanning setup

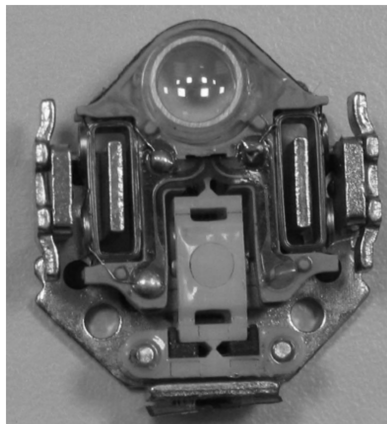

Figure 3.14: The CD-ROM optical pick-up assembly that is modified and used in the setup.

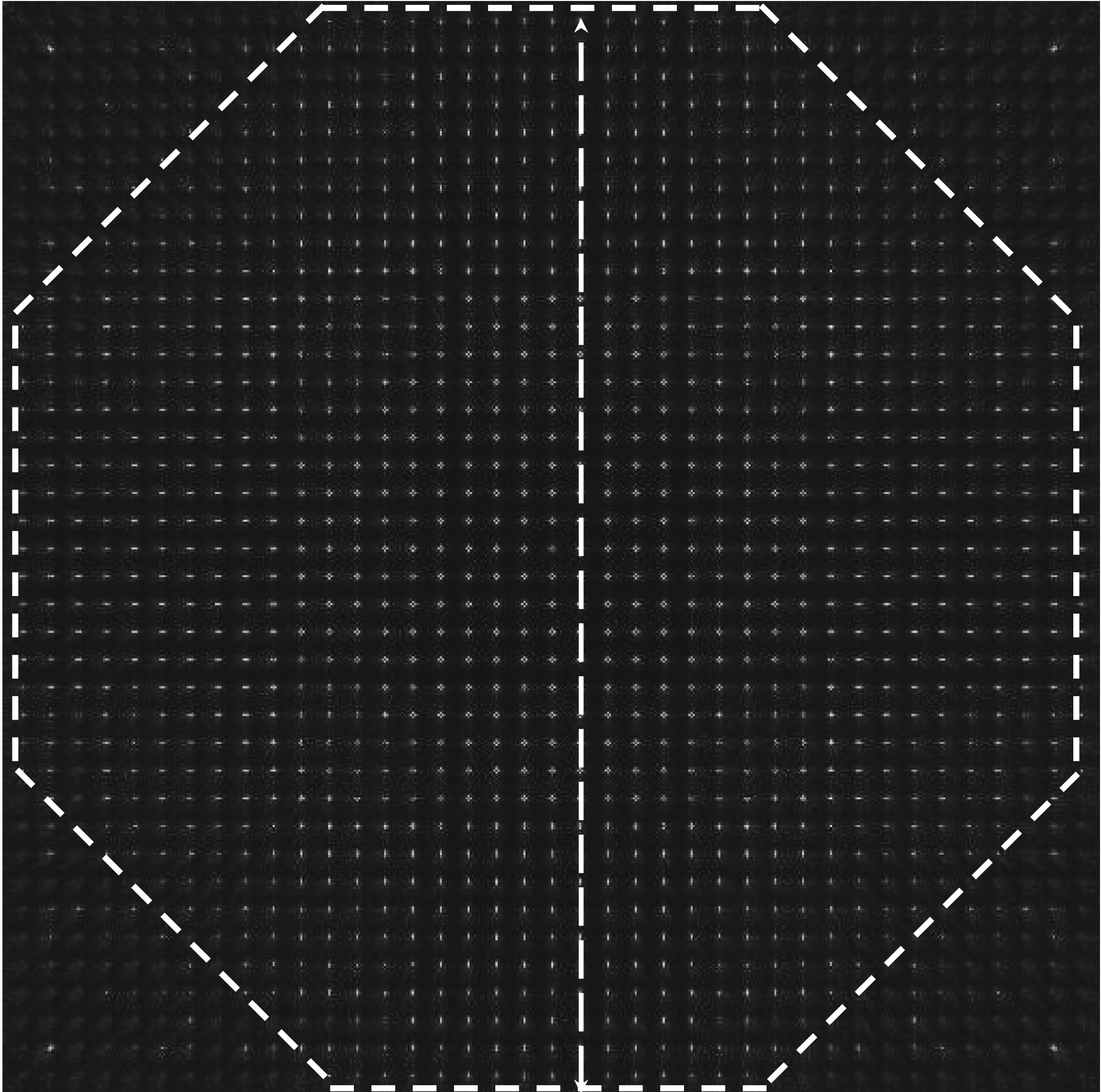

Figure 3.15: Simulated reference pattern used for alignment of the two MLAs which constitute the DMLA, i.e., far-field pattern after the DMLA. The sharpness and distribution of the diffraction orders (i.e. spots) are measures for evaluation of 6-axis alignment of two identical MLAs separated at a focal distance

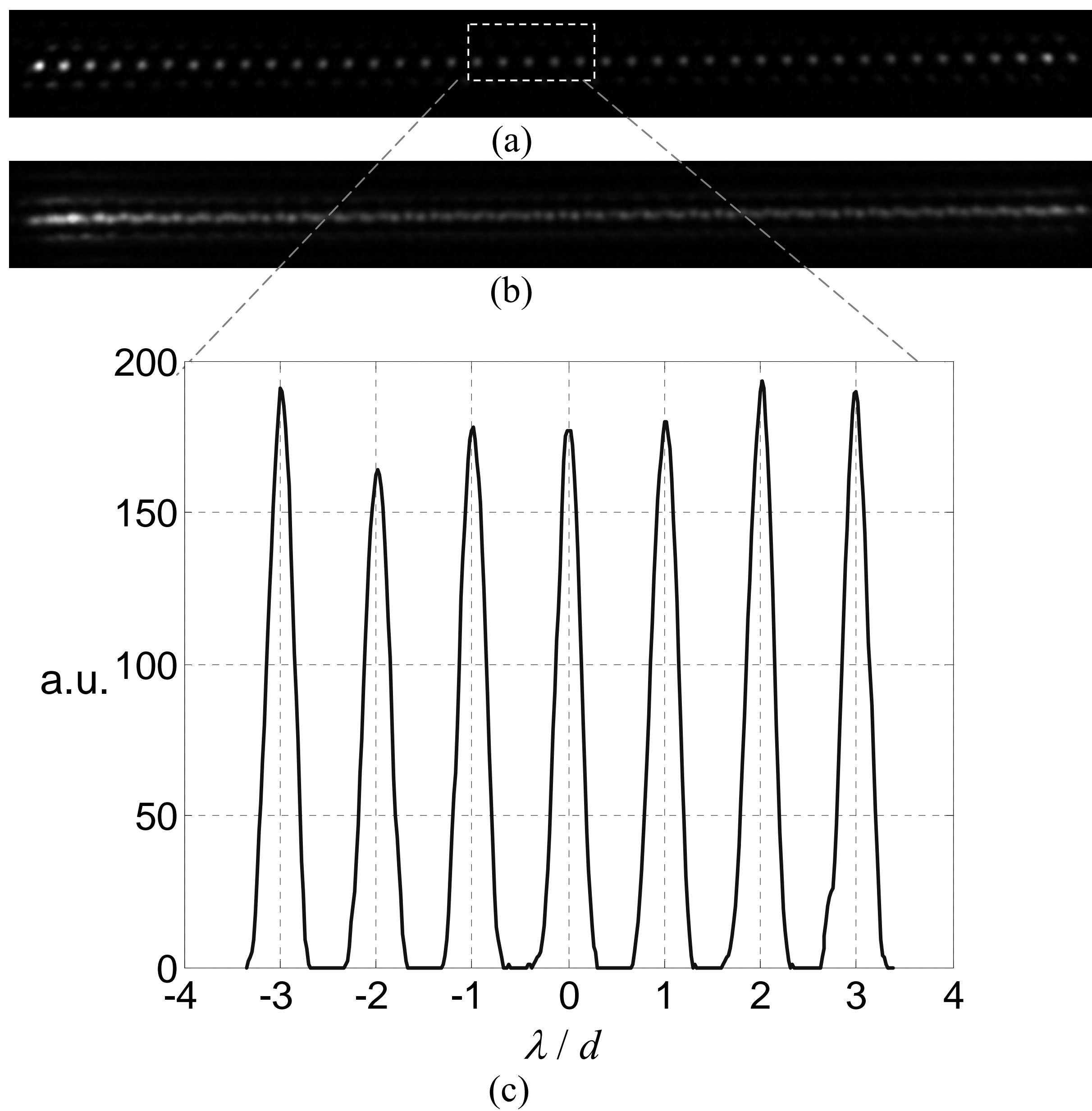

Figure 3.16: Experimental results of the line scans. (a) The MMLA motion only produces discrete addressing; (b) The PSL and the MMLA move synchronously and phase condition

is met at all times and continuous addressing is achieved (c) PSFs at five consecutive diffraction orders

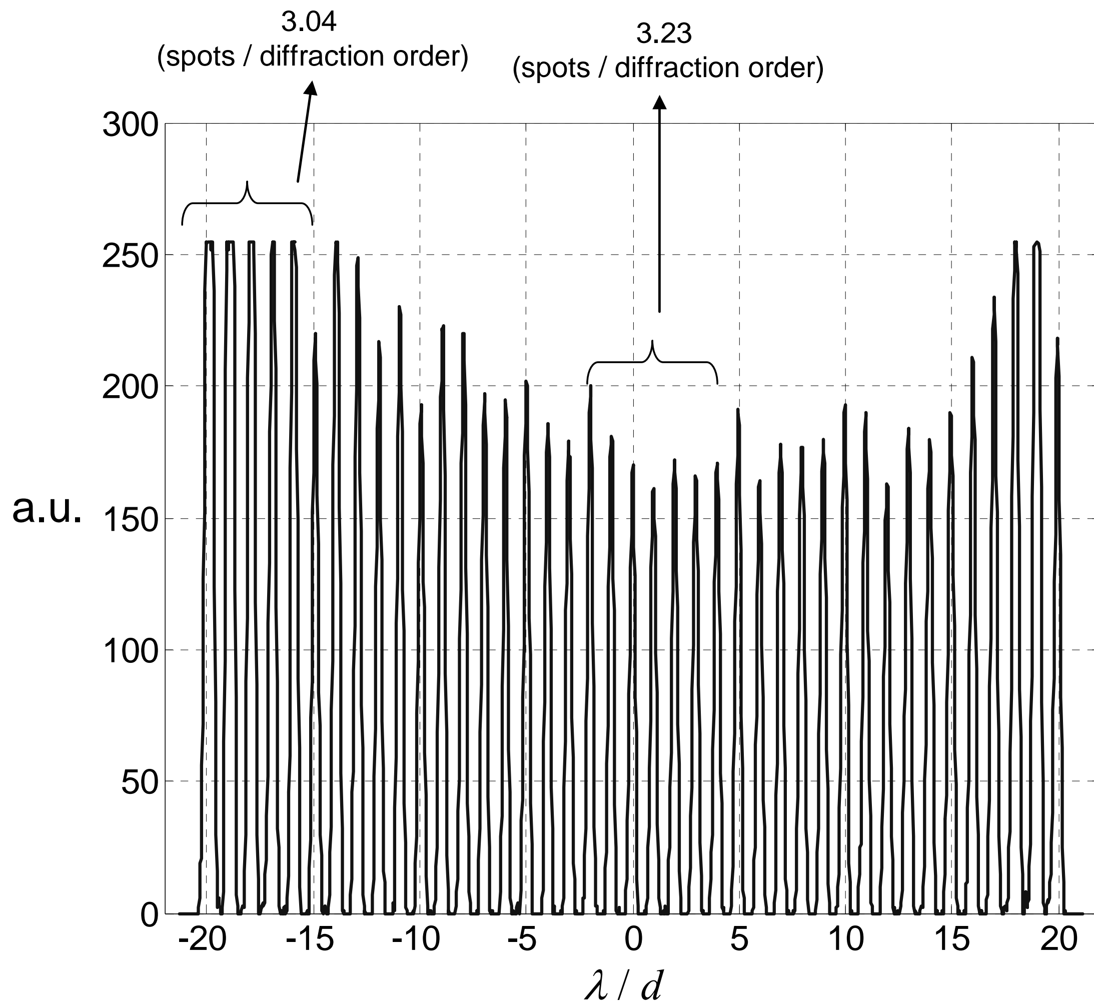

Figure 3.17: PSFs at different scan positions. Illustrates resolution of the system. Different magnitudes of the peaks are due to sinusoidally varying scanning speed across the scan line

Figure 3.16.a demonstrates 41 discrete addressable spots achieved by moving the MMLA and Figure 3.16.b demonstrates a continuous line scan obtained by combined synchronous actuation of the PSL and the MMLA. Figure 3.16.c plots the intensity profile of the

consecutive diffraction spots taken from the center of the scan line. Figure 3.17 plots the diffraction orders in the 2/3 part of the scan line, limited by the aperture size of the 5-axis positioning stage. The PSF at the off-axis scan positions broadens about 7% that is mainly due to comatic aberration. As illustrated on the figure and considering the FWHM spot size, at least three spots fit between two diffraction peaks. Hence the number of resolvable spots is in excess of 120 as shown in the Figure. Hence the unclipped full scan line is expected to have 180 resolvable spots in a line. Note that, the theoretical resolution prediction (N_R) of the experimental system is 189.

Note that, *f*/5 refractive MLAs has a simulated Strehl ratio of 0.9 (Figure 3.2), i.e., the performance should be diffraction limited. We can conclude that the experimental system worked quite well and optical performance close to the theoretical predictions is obtained.

180 resolvable spots on a line with rudimentary actuators and slow $f_{\#}$ microlenses is an important achievement. For instance, the commercial endoscope system from Olympus and several similar systems reported in the literature [47] have resolution limited to less than 100 spots.

3.6. Microlens array fabrication

Technologies for MLA fabrication, recently has improved greatly in parallel with up-growing interest in applications using MLAs. In addition to laser scanning, microlens arrays are used for a number of other applications such as: parallel optical communication, [23] video cameras, [28] beam shaping, [29] laser pulse shaping, [30] 3-D imaging [31], etc. For each application, different types of fabrication methods are favorable. In evaluation of efficiency of a microlens array fabrication method for a typical application a number of points has to be considered such as: material of the lens, integration to the system, throughput and lens shape/profile requirements. In this work, we concern applications

operating with a visible laser source. So, in this section, polymer and glass materials are considered.

As discussed in Section 3.3 and 3.4, shape of the microlenses is tremendously important for beam scanning applications. [32] For MLA beam steering applications the MLAs has to be square packed and nearly 100% fill factor.[34] The following fabrication technologies are reviewed in this section: (i) isotropic etching technique for mold making and replication on polymer by UV casting; (ii) multi-level diffraction lenses; (iii) Reflow method for refractive lenses; (iv) a hybrid method that combines methods (i) and (ii) and lastly (v) laser writing method.

Each of these methods has different advantages. For the beam steering application, the best performance can be obtained with refractive microlenses with aspherical profile, which requires laser writing technology. [33] However, isotropic etching method is low-cost, provides excellent spherical profile and packing density, and the performance is moderately good. In our experiments, we used microlenses fabricated with the isotropic etching method. We also fabricated and characterized hybrid microlenses as a novel micro-optical component.

3.6.1. Isotropic etching method

Isotropic etching of a substrate, for fabrication of a lens mold is studied previously. [35] Using that method a mold structure for fabrication of spherical lenses can be obtained. Hence, polymer lenses can be casted from the mold structure. (Figure 3.18)

The profile of the casted structure is an inverse replica to the profile of the mold structure. (Figure 3.19) So as long as a mold structure is fabricated the replication is straightforward. [35] The idea of fabricating exact spherical molds by etching lies on the fact that isotropic etching through a hole would etch the substrate at equal amount in each direction. Using an array of holes, one would create an MLA mold. Precise timing of the

etching process and ensuring that the process continues until the etching of the corners, one would obtain 100% fill-factor MLAs with sharp corners.

The fabrication of the mold structure is highly depended on the chemical process. The etching process has to be isotropic. The right isotropic etching mixture for a mold material has to be experimentally determined. For isotropic etching of Silicon the etchant to be suggested is a mixture of hydrofluoric, nitric and acetic acids (HNA) with a ratio of 2:3:3. [37] Acetic acid is used instead of water as a diluent. The overall reaction is given by [38]:

$$Si + HNO_3 + 6HF \rightarrow H_2SiF_6 + HNO_2 + H_2O + H_2 \quad (3.10)$$

In the process, temperature is critical since the etch rates of the etchants in the mixture are a function of temperature. The process is diffusion depended, i.e. the etch rate and shape of the structures are determined by the flow of reactants to the surface rather than the etch rate of the different crystal planes. In order to obtain smooth, mirror-like surfaces the slow etching process is desirable. Agitation is required to ensure uniformity through the wafer and to obtain higher yields. For agitation of the sample throughout the process, the sample tube is placed in an ultrasonic bath.

The wafer to be etched is masked with gold layer patterned with an array of holes. Chrome is used for sticking of the gold layer onto the silicon layer. The gold layer has to be thick enough to bear under etching without lifting off until the end of the etching process.

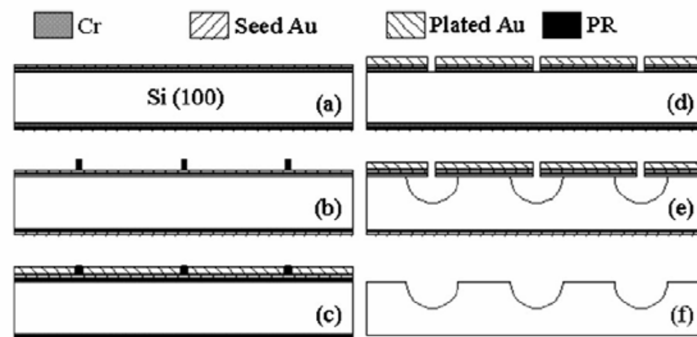

Figure 3.18: Fabrication process of the silicon mold structure

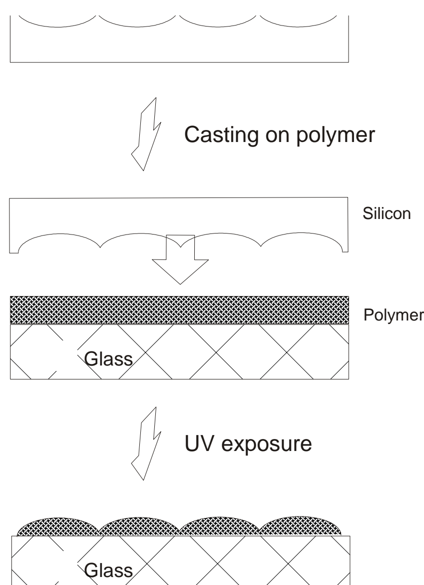

Figure 3.19: Process flow of casting from the mold structure

We have tested isotropic etching of glass, however optical quality surface roughness can not obtained. Currently in Optical Microoptics Laboratory of Koc University, a process is going on for fabrication of optical quality, perfectly isotropic etched silicon mold structures to be used in casting of MLAs. Initial lithography results are shown in Figure 3.20.

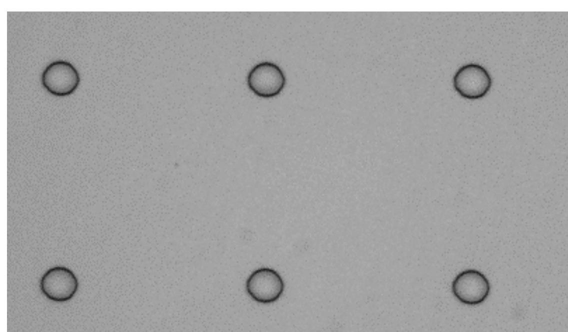

Figure 3.20: Photoresist masked gold plated silicon structure for etching of silicon though an array of holes on a masking gold layer

3.6.2. Diffractive lens fabrication method

Diffractive lenses are planar optical elements and a well-known technology. It is reviewed here as the lithographic technique is utilized to make our hybrid microlenses and to assess the performance limits of diffractive MLAs in the beam scanning system. Diffractive lenses are lighter and system integration is easier. Diffractive lens fabrication is a standard method for fabrication of lenses of any shape. So, square shaped microlenses and 100% fill-factor MLAs can be fabricated. There are a number of drawbacks of diffractive lenses e.g., low diffraction efficiency and single wavelength operation. Multilevel diffractive lenses are designed in order to improve the diffraction efficiency. A simple way of designing diffractive lenses is based on the idea that the phase function of a diffractive and refractive lens has to be equivalent, so as diffractive lens can be considered as 2π modulo of a refractive lens phase function. (Figure 3.21). As sketched in Figure 3.22, multilevel diffractive lenses can be fabricated through repeated photolithography and etching steps. Figure 3.14 illustrates that at the edges of low f# lenses, number of resolvable levels decreases down to 2. The figure plots the radius up to which a number of resolvable diffraction levels can be fabricated as a function of f# of the lens.

The fabrication process of diffractive elements is highly repeatable and controllable. In that way, conventional interferometric zone plates (IZP) can be constructed. [40] In an m-mask process, the 2π modulo profile can be approximated by 2^m staircase phase levels. Diffraction efficiency of a multilevel diffractive lens is given by: [41]

$$\text{sinc}^2(\pi \cdot 2^{-m}), \quad \text{m: \# of masks} \tag{3.11}$$

4 phase level lenses of diffraction efficiency 81% can be fabricated in a two mask process. Likewise 8- and 16-level diffractive lenses can be fabricated using three and four masks and diffraction efficiency is 97.4% and 99%, respectively.

For IZP lenses the radius of the mth plate is given by: $r_m^2 = 2m\lambda f + (m\lambda)^2$. The IZP phase distribution is given by:

$$\text{IZP Phase Distribution:}\ \phi(r) = (2\pi/\lambda)(f - \sqrt{f^2 + r^2}) - \phi_0 \qquad (3.12)$$

Diffraction efficiency of an IZP lens can be slightly improved by optimization of ϕ_0.

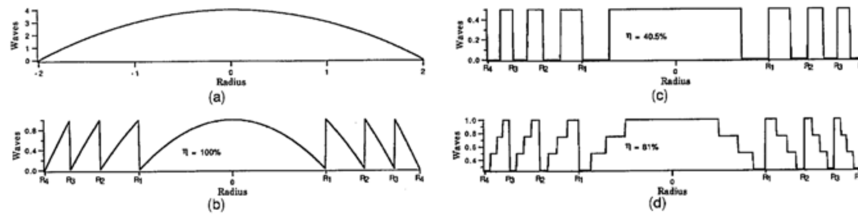

Figure 3.21: Design of multi-level diffractive lenses [39]

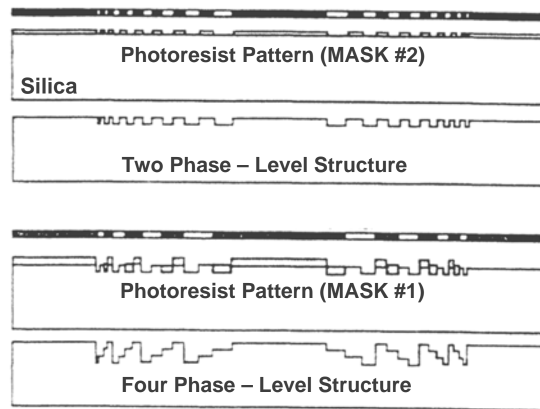

Figure 3.22: Two mask fabrication process of a 4-level diffractive lens

3.6.3. Reflow method

The reflow fabrication method is a standard method for fabrication of circular shape, spherical profile lenses by using surface tension effect in a melting process. [42] That method is recently applied for the fabrication of microlens arrays. [43] In this subsection the reflow method is discussed and later the technique is applied to make hybrid microlenses.

In the reflow method, columns of transparent photoresist (PR) are melted on a wafer and due to the surface tension, the melted PR shapes into a spherical profile. Rectangular and hexagonal arranged lenses reflowed from circular shaped columns have maximum fill-factors of 78% and 90%, respectively. In standard lens reflow method, the PR columns have to be separated at a safe distance in order to avoid merging of lenses while melting. That also limits the fill-factors of reflowed MLA. [42]

A recent modified reflow method is studied for fabrication of nearly 100% fill-factor MLAs. [43], [44] In order to improve fill-factors of the reflows MLAs, square-shaped columns are melted rather than circular-shaped columns. The process is rigorous, needs critical timing and direct observation.

The fabrication process is summarized in Figure 3.23. The negative PR is under-exposed by UV to form islands of PR columns spaced at the desired array pitch. The PR is under-developed, so that the PR in between the square columns is not completely removed, i.e., a thin layer of PR is kept between columns. That thin layer of PR in between the columns is pivotal for filling the spaces between the columns. PR columns expand their basis on the wafer, while reflowing. Timing of the melting process is critical and direct observation of the melting progress is required to avoid merging of adjacent columns. The reflowing process has to be terminated immediately after the melting PR columns fill the most of the space in between them, and before merging with each other. Uniform spherical lens profile can be obtained all through the wafer by ensuring uniform heat distribution on the wafer in the reflowing process.

MLAs of pitch 55 μm are reflowed from 40 μm square photoresist columns by following the process flow given in Figure 3.23. The profile of the lenses is compared to the exact spherical profile in Figure 3.24. Microscope image and image of spots of an MLA is given in Figure 3.25. As one might notice there exist a spacing in between the

microlenses, which cause a degradation in the diffraction performance of MLA beam scanning system as discussed in Section 3.3.

The reflow method can be used to fabricate lenses of $f_{\#}$ as low as 2. Focal length of the lenses can be calculated from the thickness of the columns and refractive index of the PR. The desired focal length can be obtained by adjusting the PR thickness while spinning it on the substrate. A spacing in-between two neighboring microlenses appears in MLAs fabricated by the reflow method. The spacing is necessary otherwise the microlenses may merge each other in the reflow process.

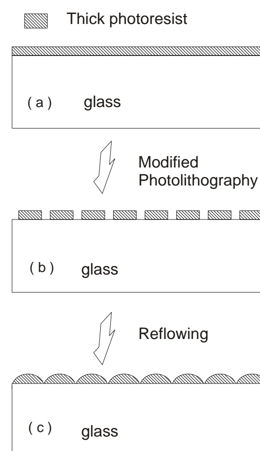

Figure 3.23: Process flow for reflow fabrication method

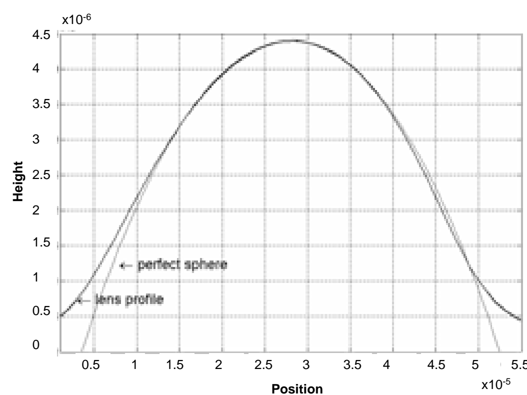

Figure 3.24: Profile of the reflowed lenses compared to the perfect spherical profile

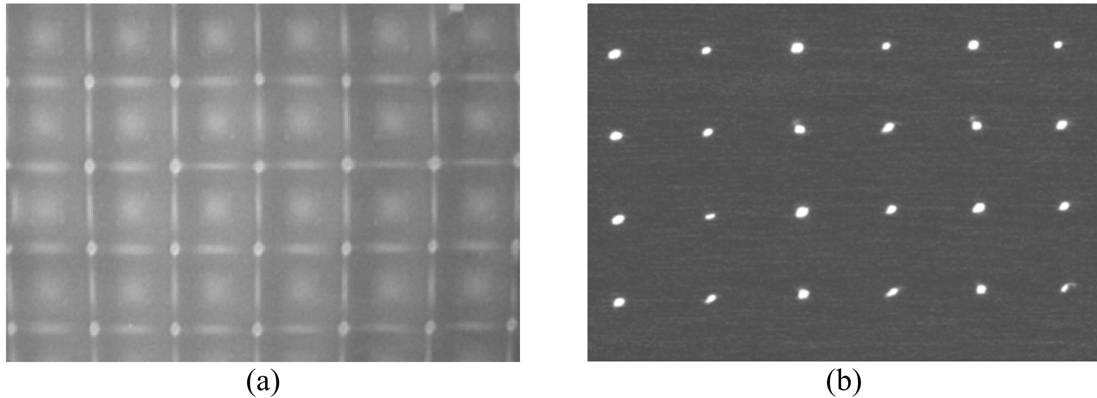

Figure 3.25: Microscope image of the reflowed square-shaped MLAs and focused spot image of that MLA

3.6.4. Hybrid method

Alternatively, one would combine two standard MLA fabrication methods, e.g., diffractive and reflow methods to obtain MLAs of 100% fill-factor and easy to fabricate. This method is introduced and tried for the first time during author's visit to Heriot-Watt University, U.K. under the guidance of Prof. Mo Taghizadeh. As called the "hybrid method" is based on the fabrication of circular reflow lenses on top of diffractive lenses or diffractive frames at the corners. (Figure 3.26) The method, however, requires two step fabrication, is simple as no precise timing and direct observation of the reflow process is requires. Two combined lenses (i.e., diffractive and reflow) has to have a common focal length, hence the thickness of the PR column has to be adjusted and that way focal distance match can be ensured. Figure 3.27 shows a through focus graph of a hybrid lens, i.e., peak intensity of the beam in a plane scanned around at the focus distance is measured and plotted. If the focal distances of the refractive and the diffractive lenses do not match, then a double peak would be observed in the through focus plot.

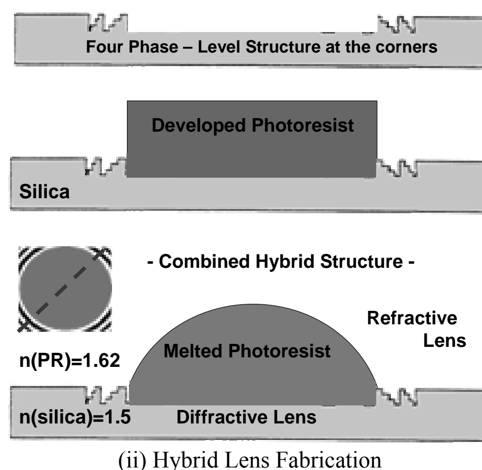

(ii) Hybrid Lens Fabrication

Figure 3.26: Fabrication of the diffractive lenses and hybrid lenses

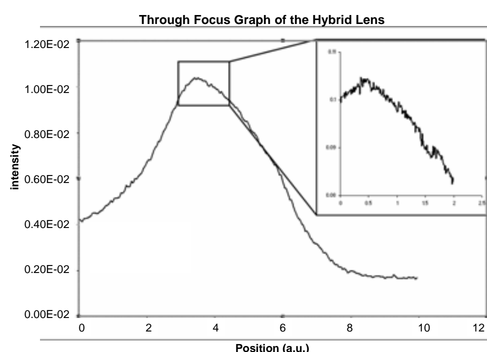

Figure 3.27:Through focus plot of the hybrid lens. Demonstrates focal distance match of diffractive and refractive lenses

3.6.5. Laser writing method

A laser writing system can fabricate continuous microstructures without using any masks. Masks are expensive and fabrication of masks introduces delays in a fabrication process. Also fabrication of arbitrarily surface-relief profile requires a number of masks or expensive gray-scale masks, and the fabrication cost increases even more. Direct laser writing is a method for fabrication of arbitrary surface-relief profile microstructures. The technique is an alternative to and has advantages over electron-beam writing. It requires

neither a vacuum system nor a conductive film on the substrate and has a large writing field.

The operation of the laser writing system and a typical lithography process are alike. In lithography process a UV sensitive material is exposed to UV and then developed to selectively remove unexposed or exposed material. Similarly, in laser writing operation mostly a UV source is used for exposure and the exposed areas are removed in some degree selectively (e.g. positive PR) by a following a PR development process. The differences to a typical lithography process are those: (i) a focused laser source is used and scanned to expose the areas to be removed instead of flood illumination by UV lamp, Figure 3.28 (ii) dose of exposure determines the amount of the material to be removed. By modifying the exposure intensity or scanning speed throughout the scanning of the surface, amount of the material (i.e., the thickness of the removed material) can be adjusted, and that way a continuous arbitrary surface profile can be written on the substrate. [45]

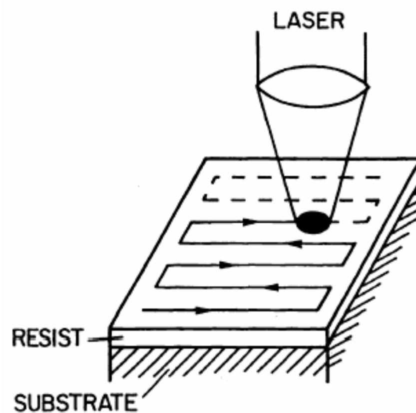

Figure 3.28: Scanning of the laser spot across the PR spinned substrate [45]

Laser writing process requires modeling of the PR response (i.e., degree of developing) as a function of the exposure. The size of the focused laser beam determines the minimum feature fabricatable. Laser writing process requires scanning of the focused laser beam all throughout the substrate and modifying the intensity. Thereby, a fast and precise laser

scanning system or positioning system laser modulation system is required. A computer controlled system is suggested for direct laser writing which uses a scanned UV objective and fiber for transmission of the UV light into the objective. (Figure 3.29)

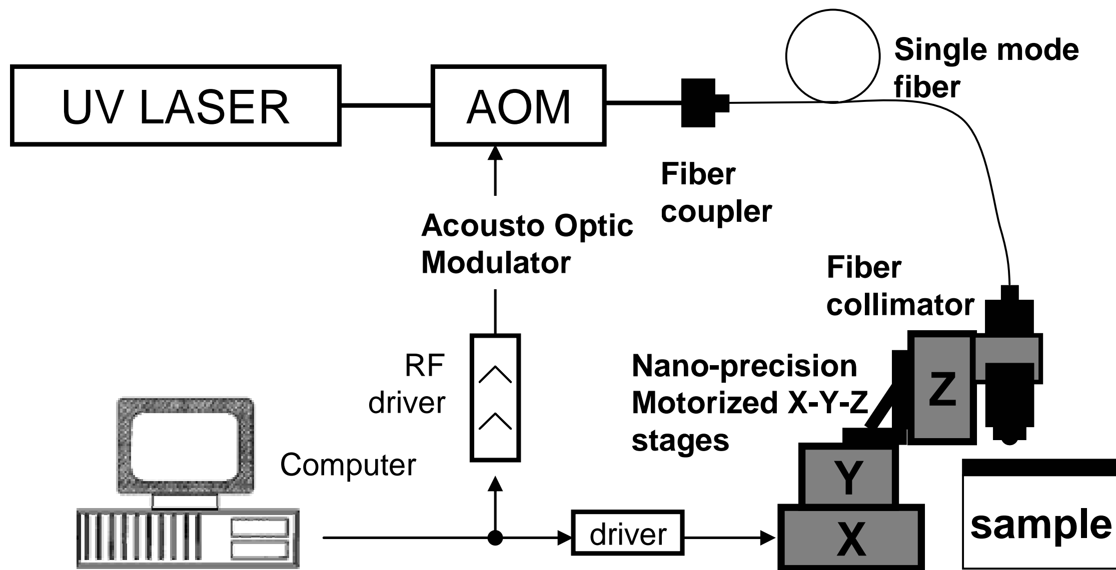

Figure 3.29: Maskless laser scanning writing setup for fabrication of MLAs

Using laser writing technique fabrication of 100% fill-factor MLAs with arbitrary aspherical profiles is possible. Aspherical profiled MLAs can be designed to perform better than spherical MLAs. So, the method is highly valuable for fabrication of MLAs for laser beam scanning system. The fabricated MLAs can be used to fabricate a replica mold structure to be used for replication of a series of copies by casting. In another project the system illustrated in the figure will be realized by a colleague in Optical Microoptics Laboratory through a grant received from Tubitak starting Sep. 2006.

CHAPTER 4

SYSTEM IMPLEMENTATION AND OPERATION

This chapter issues system implementation and operation. As the MLA scanning system is an uncommon exceptional system in which mechanical displacements and diffraction of beamlets plays a concurrent role in scanning of a beam, it has unique operation modes and the implementation of the actuators for the system requires special attention.

4.1. Continuous addressing

As discussed in Chapter 2, continuous addressing requires full filling the phase conditions. Phase conditions are shown to be satisfied by pre-scanning before the MLA scanning system. In this section pre-scan is implemented in two ways: (i) by a PSL and (ii) by an LC scanner.

4.1.1. PSL implementation

Continuous scanning can be obtained synchronized actuation of the PSL and MMLA as discussed in Chapter 2. Figure 4.1 shows the required deflections of the PSL and MMLA. PSL is actuated in resonance for fast operation whereas MMLA actuation can be obtained by combining a sinusoidal and a stair-step-like actuation. Note that during the “scan” cycle a continuous scan is achieved, during the “step” cycle the PSL is retraced back into starting position while the laser spot remain parked at a particular diffraction order. The laser should be turned off during this time. Only 50% of the time is utilized for scanning while

the remaining time is used for retrace. This ratio can be improved if a non-resonant scanning approach is utilized.

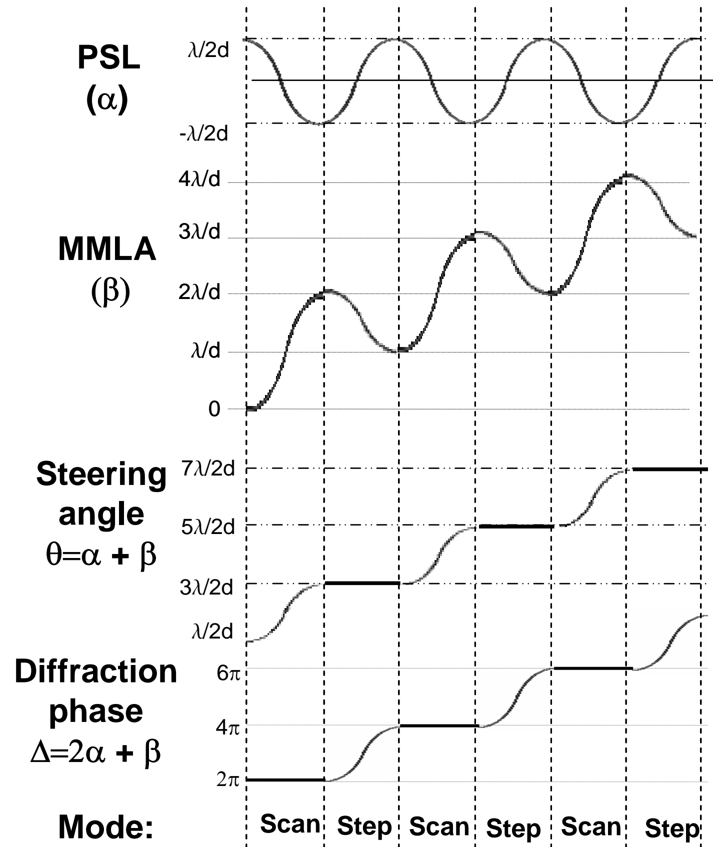

Figure 4.1: Driving scheme for continuous addressing. Plots show PSL and MMLA displacement values in terms of introduced steering angles α and β.

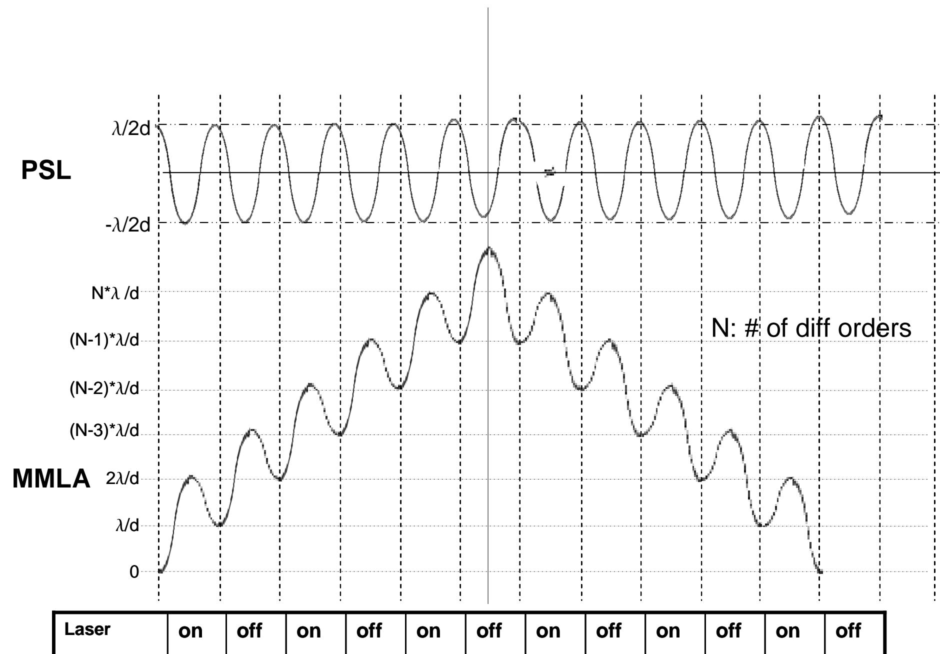

Figure 4.2: Actuation of the PSL and MMLA for scanning a full line

Figure 4.2 plots driving scheme for MMLA, showing the complete cycle. The same scanning scheme can be applied in both scan directions to obtain 2D scanning. In a scanning system the data rate DR can be calculated in terms of resonant frequency R (in Hz), and number of line scans L, such that: DR=2R/L. However, note that for the given driving scheme, the data scan rates has to be scaled by the number of oscillations N, required to scan a line. So the data rate for the plotted driving scheme can be calculated as: DR=2R/L/N.

4.1.2. Liquid crystal (LC) implementation

An alternative pre-scanning approach is by employing a liquid-crystal (LC) phase shifter in place of the PSL, where each LC pixel is coupled with a microlens in the MMLA. In that case MMLA can be actuated in resonance. The tilt angle α introduced by the LC

module can be determined by considering the constructive phase function conditions given in the Chapter 2. The tilt angle introduced by the LC phase shifter can be calculated as:

$$\alpha = -\frac{\beta}{2} \quad \mathrm{mod}(\frac{\lambda}{2}) \tag{4.1}$$

where θ is equal to sin(2πf·t), and f denotes the frequency of actuation. Figure 4.3 plots the α and β angle. The scan angle θ, is than computed as sum of α and β and plotted in Figure 4.4. Note that, in a single period scan, discrete segments of the line is scanned and for scanning of a whole line, two cycle scanning of the system is required.

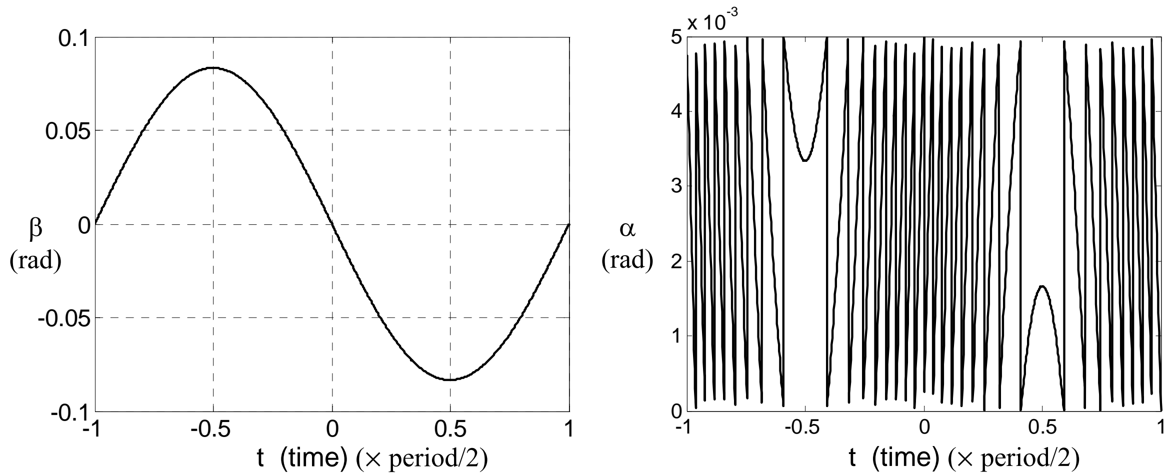

Figure 4.3: Driving scheme for continuous addressing. Plots show LC implemented PSL and MMLA displacement values in terms of introduced steering angles α and β.

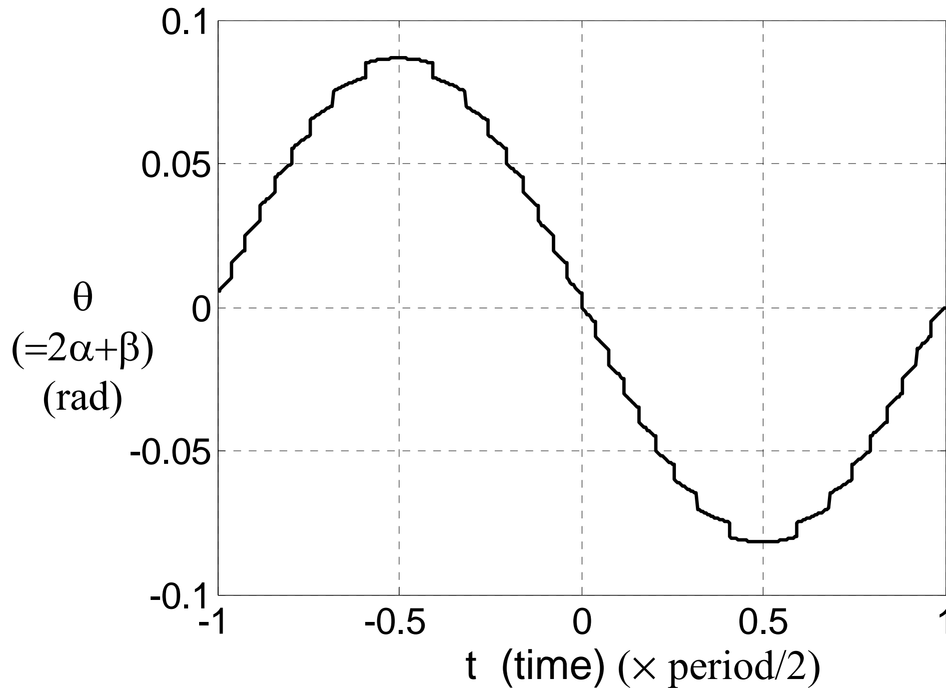

Figure 4.4: The resulted scan angle θ when the actuation given in Figure 4.3 is applied

Note that, in that driving scheme the data rate is not scaled and can be computed as: DR=2R/L.

4.2. Monochromatic imaging

Imaging through the MLA scanner is subject to diffraction effects as in scanning a laser beam. The PSF of the imaging system (PSF_{im}), is dependent on the PSL, MMLA displacements and the spectral distribution of the imaged beam. In this section imaging of a monochromatic beam is investigated.

As analyzed previously, PSL and MMLA displacements tilt the beam at angles α and β. Addressing of a single position is possible mostly at a single wavelength at a time, by satisfying the phase conditions. When the system is conditioned to scan at a

wavelength, λ_{sc} and a monochromatic beam at other than the λ_{sc} is imaged, the PSF_{im} splits into multiple lobes because of the diffraction effects. As discussed in Chapter 2, a phase function ϕ_T, is used is used for evaluation of the PSF of the scanning system (PSF_{sc}). Likewise in this section two phase functions, ϕ_{sc} and ϕ_{im}, are defined for evaluation of the scanning and imaging PSF functions, respectively:

$$\phi_{sc} = 2\alpha + \beta - m_{sc}\frac{\lambda_{sc}}{d} \tag{4.2}$$

And,

$$\phi_{im} = 2\alpha + \beta - m_{im}\frac{\lambda_{im}}{d} \tag{4.3}$$

where λ_{im} denotes wavelength of imaging and m_{im} is an integer. When the system is conditioned for scanning a laser beam, ϕ_{sc} is ensured to be equal to zero, then ϕ_{im} is most likely to be non-zero, such that:

$$\begin{aligned}\phi_{im} &= m_{sc}\frac{\lambda_{sc}}{d} - m_{im}\frac{\lambda_{im}}{d} \\ &= m_{sc}\frac{\lambda_{sc}}{d} \quad \mathrm{mod}(\frac{\lambda_{im}}{d})\end{aligned} \tag{4.4}$$

For the most likely case where ϕ_{im} is not equal to zero, the PSF splits into two in one axis. Note that the phase analysis so far is considered in one dimension, and application of the results obtained for 1-D to a 2-D system is trivial. For example one can define two phase functions $\phi_{im,x}$ and $\phi_{im,y}$ for x and y axes, and when these two phase functions are not equal to zero, the PSF spits into four diffraction lobes, the case $\phi_{im,x} \neq 0$ is shown in Figure 4.5.

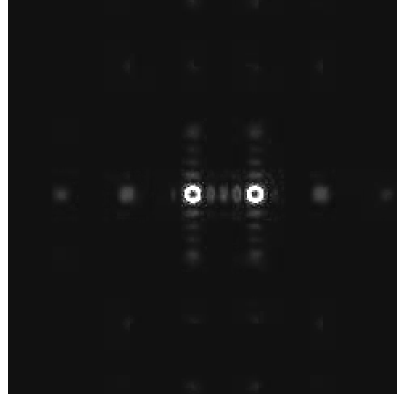

Figure 4.5: 2-D spot of the system for $\phi_{im,x}\neq0$, $\phi_{im,y}=0$

As discussed in Chapter 2 one can determine ϕ_{im} by evaluation of the PSF_{im} e.g., by measuring the positions of or intensity on the split diffraction lobes. We claim that, given the λ_{sc}, α and β, one can determine λ_{im}. In the rest of the section the early PSF analysis are further developed to obtain a quantitative relation between the PSF and ϕ_{im}.

As studied in Section 2.3 the PSF_{sc} of the scanning system is composed of periodic and envelope Sinc functions. In the same way the PSF_{im} is determined by the two Sinc functions. Periodic Sinc function corresponds to the far-field diffraction pattern of the whole beam of size D, and envelope Sinc function corresponds to far-field pattern of a single beamlet output from a three-microlens channel. Size of the beamlet is approximately equal to the pitch of the MLAs, and denoted by d. The far-field distributions of the beamlets constitute the envelope Sinc function. The envelope Sinc function has λ/d distance between the zero and peak positions as illustrated in Figure 4.6. Similarly the period of the periodic Sinc functions is λ/d. Whenever, the ϕ_T is equal to zero, peaks of the periodic Sinc functions, other than the center peak, overlaps zero positions of the envelope Sinc function. When ϕ_T is not equal to zero, the positions of the diffraction peaks are shifted and cease corresponding to zero positions of the envelope Sinc function and appears in the PSF as illustrated in Figure 4.6.

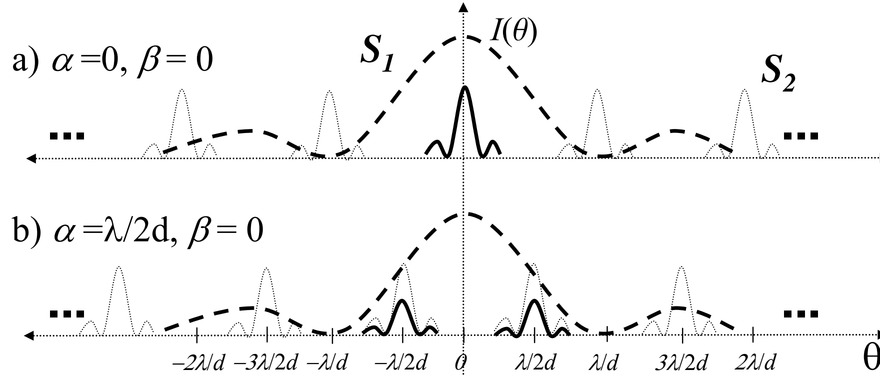

Figure 4.6 Illustration of the Sinc functions used for PSF analysis

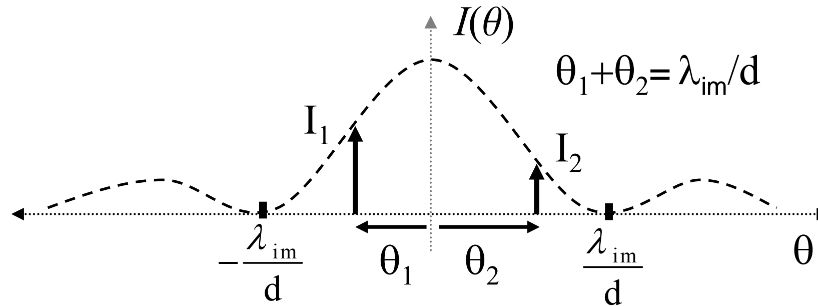

Figure 4.7 Representation of diffraction lobes appear in the PSF

Figure 4.7 defines the positions and amplitudes of the diffraction lobes. The PSF_{im} can be determined by following the scheme given in Figure 4.8.a. in accordance with the analysis in Section 2.3. Then one can obtain the following relations, regarding the distribution of diffraction lobes appear in PSF_{im}:

$$\theta_1 = \phi_{im} = m_{sc}\frac{\lambda_{sc}}{d} \quad \mathrm{mod}(\frac{\lambda_{im}}{d}), \qquad m_{im} \approx m_{sc}\frac{\lambda_{sc}}{\lambda_{im}}$$
$$\theta_2 = \frac{\lambda_{im}}{d} - \theta_1 = \frac{\lambda_{im}}{d} - \phi_{im} \tag{4.5}$$

$$A_1 = \mathrm{Sinc}(\theta_1 \cdot \mathrm{d}/\lambda_{\mathrm{im}}) \tag{4.6}$$

$$A_2 = \mathrm{Sinc}(\theta_2 \cdot d/\lambda_{im})$$

Center of the PSF (θ_{center}) of the PSF_{im} can be defined as:

$$\theta_{center} = \frac{\theta_1 A_1 + \theta_2 A_2}{2} \tag{4.7}$$

Using the simple formulas given above, it is trivial to determine the wavelength of the monochromatic source, in any position in the image plane. The spectroscopic imaging scheme outlined here is constrained to imaging a monochromatic source. However in most imaging applications imaging of a narrowband and/or spatially extended sources are of interest. The analysis of this section constitutes a basis for the following sections, where imaging of a temporally incoherent (i.e., narrowband) or an extended source is analyzed.

4.3. Temporally incoherent imaging

In Section 4.2, imaging of a monochromatic source is analyzed and monochromatic point spread function, i.e., spectral impulse response of the system is formulated. The system is modeled as shown in Figure 4.8.a. In this section, the analysis is extended to narrowband imaging, where the source has a spectral distribution defined by $A(\lambda)$ of width $\Delta\lambda_{im}$ and centered at λ_{im}.

Of interest is determination of the spectral distribution of the source from the PSF_{im} distribution. For that purpose, establishment of a linear shift invariant (LSI) system model for mapping between the PSF_{im} distribution and spectral distribution of the beam is desired. However, as shown in Section 4.2 positions, θ_1 and θ_2, of the diffraction lobes, and widths of the S_1 and S_2 functions are linearly-dependent on the wavelength λ_{im}. If the spectrum of the beam is sufficiently narrow e.g., $\Delta\lambda_{im} << \lambda_{im}$, and $m_{im}=1$ one can neglect the wavelength dependence of widths of S_1 and S_2. In that case the system can be treated a LSI system and

narrowband PSF of the imaging system can be formulated by simple mathematical operations e.g., convolution and multiplication.

The narrowband PSF_{im} can be determined by superposition or integration of the spectral impulse response of the system over spectrum range. Accordingly, using impulse response of the system given in Chapter 2, the narrowband PSF_{im} can be expressed as:

$$I(\theta) \propto \int_{-\infty}^{\infty} \left\{ \begin{array}{l} \mathrm{A}(\lambda)\mathrm{sinc}^2\left[(d/\lambda)\theta\right] \\ \times \left[\begin{array}{l} \mathrm{comb}\left((d/\lambda)\left(\theta - (\theta_1 + \lambda - \lambda_{im})\right)\right) \\ * \ \mathrm{sinc}^2\left((Nd/\lambda)\theta\right) \end{array} \right] \end{array} \right\} d\lambda \qquad (4.8)$$

For convenience of the analysis the equation can be simplified by considering only two peaks of the comb function, which are chosen to be inside the main lobe of the first Sinc function. Then the equation becomes:

$$I(\theta) \propto \int_{-\infty}^{\infty} \left\{ \begin{array}{l} \mathrm{sinc}^2\left[(d/\lambda)\theta\right] \\ \times \left[\begin{array}{l} \mathrm{A}(\lambda) \times \left(\begin{array}{l} \delta\left(\theta - \theta_1 - (\lambda - \lambda_{im})/d\right) \\ + \ \delta\left(\theta - \theta_1 - (\lambda - 2\lambda_{im})/d\right) \end{array} \right) \\ * \ \mathrm{sinc}^2\left((Nd/\lambda)\theta\right) \end{array} \right] \end{array} \right\} d\lambda \qquad (4.9)$$

Modeling of the system with the above equation is linear shift non-invariant. However, it is desired to obtain a linear shift invariant (LSI) system modeling, so that the PSF can be formulized by simple convolution instead of an integration operation. Using such a formulation, spectral distribution of the imaged beam can be determined very precisely from the detected PSF_{im} distribution. For that purpose, i.e., to obtain LSI system modeling, the spectral width of the imaged beam is assumed to be such that $\Delta\lambda_{im} \ll \lambda_{im}$. In that case, the width of the Sinc functions can be assumed to be independent of the λ. Then (4.9) becomes:

$$I(\theta) \propto \left\{ \begin{array}{l} \mathrm{sinc}^2\left[(d/\lambda_{im})\theta\right] \\ \times \int\limits_{-\infty}^{\infty} \left\{ \left[\begin{array}{l} \mathrm{A}(\lambda)\times\left(\begin{array}{l} \delta\left(\theta-\theta_1-(\lambda-\lambda_{im})/d\right) \\ +\ \delta\left(\theta-\theta_1-(\lambda-2\lambda_{im})/d\right) \end{array} \right) \\ *\ \mathrm{sinc}^2\left((Nd/\lambda_{im})\theta\right) \end{array} \right] \right\} d\lambda \end{array} \right\} \tag{4.10}$$

Further simplification of the equation is follows the relation given below:

$$\begin{aligned} T(x) &= \int\limits_{-\infty}^{\infty} u(\xi)\left[v(x-\xi)*y(x)\right]d\xi \\ &\approx \left[\int\limits_{-\infty}^{\infty} u(\xi)v(x-\xi)d\xi\right]*y(x), \qquad if\ \ y(x)\approx\delta(x) \end{aligned} \tag{4.11}$$

For N>>1, one can show that, $\mathrm{sinc}^2\left((Nd/\lambda_{im})\theta\right)\approx\delta(\theta)$ and using (4.11), (4.10) can be rewritten as:

$$I(\theta) \propto \left\{ \begin{array}{l} \mathrm{sinc}^2\left[(d/\lambda_{im})\theta\right] \\ \times \int\limits_{-\infty}^{\infty} \left[\mathrm{A}(\lambda)\times\left(\begin{array}{l} \delta\left(\theta-\theta_1-(\lambda-\lambda_{im})/d\right) \\ +\ \delta\left(\theta-\theta_1-(\lambda-2\lambda_{im})/d\right) \end{array} \right) \right] d\lambda \\ *\ \mathrm{sinc}^2\left((Nd/\lambda_{im})\theta\right) \end{array} \right\} \tag{4.12}$$

Note that the integral equation is a convolution operation, and the (4.12) can be expressed as:

$$I(\theta) \propto \left\{ \begin{array}{l} \quad \mathrm{sinc}^2\left[(d/\lambda_{im})\theta\right]\times\mathrm{A}'(\theta) \\ *\left(\begin{array}{l} \delta(\theta-\theta_1) \\ +\ \delta(\theta-\theta_1+\lambda_{im}/d) \end{array} \right) *\ \mathrm{sinc}^2\left((Nd/\lambda_{im})\theta\right) \end{array} \right\} \tag{4.13}$$

$$\text{where, } \mathrm{A}'(\theta)=\mathrm{A}'\left(\frac{\lambda-\lambda_{im}}{d}\right)=\mathrm{A}(\lambda-\lambda_{im})$$

Figure 4.8.b illustrates the PSF analysis of the system for narrowband imaging. The single modification to the monochromatic formulation given in Figure 4.8.a, is convolution of the diffraction peaks (*P(θ)*) with the spectral distribution function *A(θ)*. In the analysis $\Delta\lambda_{im} = 0.1\lambda_{im}$, $\lambda_{sc}=1.2\lambda_{im}$ and $m_{im}=1$.

Note that in the analysis that results with the formulation given in Figure 4.8.b, *m* is equal to one e.g. first order diffraction positions are scanned. The relation between the scan angle θ and m_{im} can be established as:

$$\theta = m_{sc}\lambda + \phi_{sc}/2 \text{ where } \phi_{sc} < \lambda/d \quad \text{and} \quad m_{im} \approx m_{sc}\frac{\lambda_{sc}}{\lambda_{im}} \tag{4.14}$$

For m=1; the scan angle is constrained such that: $0.5\lambda/d<|\theta|<1.5\lambda/d$. Using (4.5) one would observe that for higher values of *m*, and larger scan angles, the lobes PSF_{im} broadens such that width of lobes are equal to broadening product (BP) given by $m\Delta\lambda_{im}$. Hence for the analysis to be valid at large scan angles one should care:

$$BP = m_{im}\Delta\lambda_{im} << \lambda_{im} \tag{4.15}$$

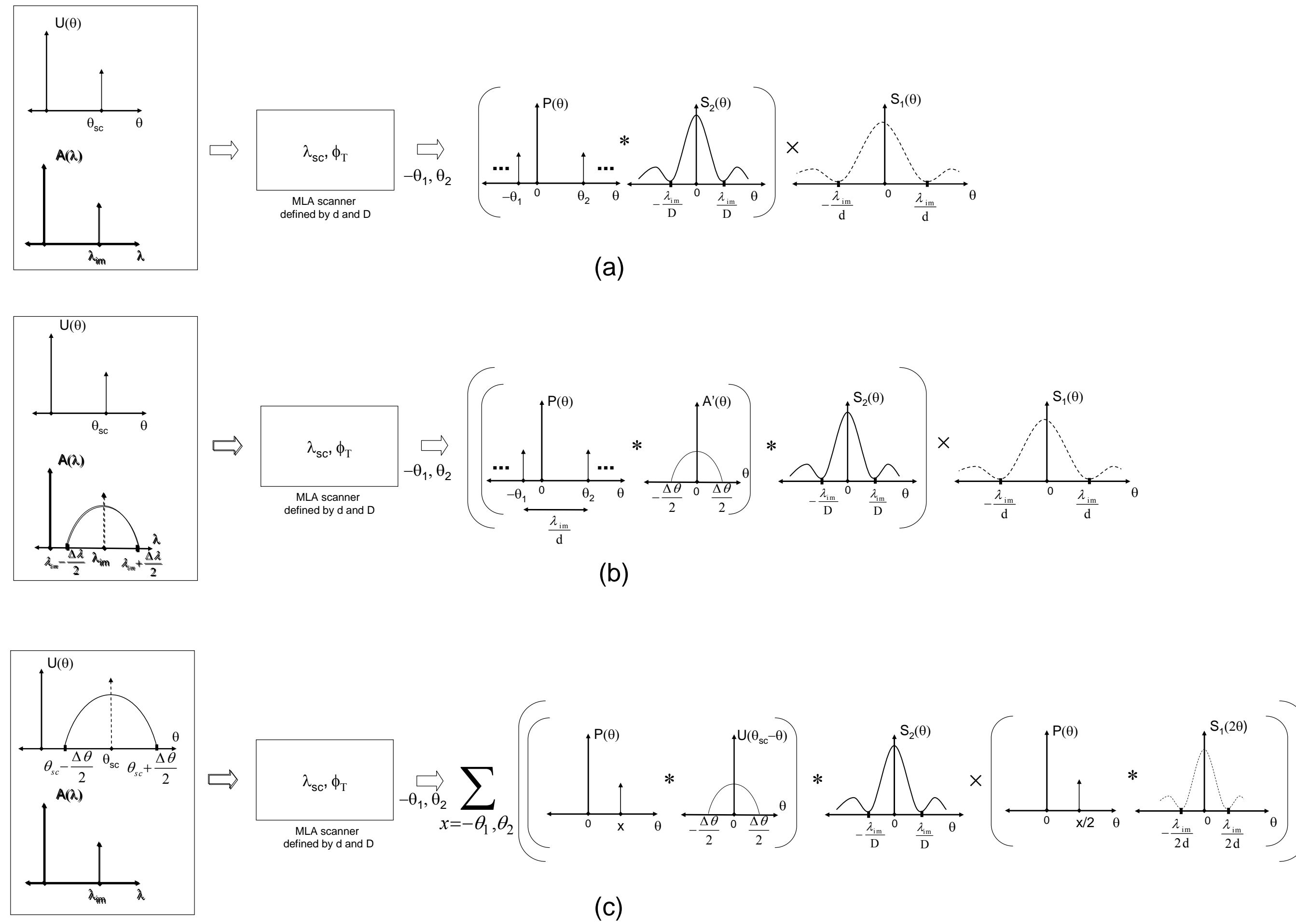

Figure 4.8: Modeling of the narrowband imaging system ($m_{im}\Delta\lambda_{im} << \lambda_{im}$)

As analyzed and illustrated using the MLA scanner, a sufficiently narrowband source can be imaged and spectroscopic distribution of the source can be determined.

For any value of spectral width of the source ($\Delta\lambda_{im}$) and the scanning angle (θ), width of the PSF is limited by the maximum spectral component λ_{max} e.g., $\theta < \lambda_{max}/d$. Figure 4.9 plots the position (θ_1) of the spectral components of an imaged broadband source. Note that, Figure 4.9 plots position of one of the two diffraction lobes appearing in the PSF, and the position of the other lobe (θ_2) is at a distance λ/d, such that $|\theta_1-\theta_2|=\lambda/d$. All the optical intensity imaged from a broadband source is distributed in an angular area of width smaller than $2\lambda/d$.

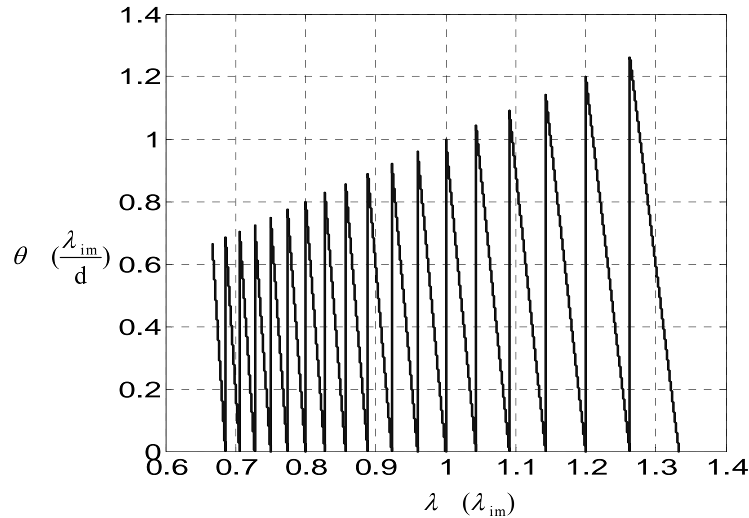

Figure 4.9: Positions of spectral components on the imaging plane. Illustrates folding of the spectrum according to (4.5) (λ_{sc}=1.2λ_{im}, m_{sc}=20)

4.4. Spatially incoherent imaging

The distribution and shape of the diffraction lobes in the PSF_{im} also related to the degree of spatial extension of the source. In this section, results of the Section 4.2 are extended for analysis of spatially incoherent imaging of an extended source of width $\Delta\theta$.

In imaging of an extended source, diffraction lobes in the PSF_{im} broaden. Furthermore the intensity center of the PSF_{im} is related to the angular distribution of the source relative to the scan position (θ_{scan}).

For the analysis of imaging of an extended source the same approximations applied in Section 4.3 can be used, by constraining the extension of the source such that $\Delta\theta << \lambda_{im}/d$. As in most of the imaging optical systems, the PSF_{im} of an extended source can be determined by convolution of the PSF of the point source (i.e. impulse response of the system) and source distribution. There are also system specific considerations needs to be taken care of. For the analysis of the extended source imaging one can use the results obtained in Chapter 2. This is because the PSF is reshaped by imaging an off-axis point is exactly in the same way as in scanning a beam by displacing the PSL. Accordingly, the distribution of the beam $U(\theta)$ has to be reversed such that $U(-\theta)$ in the convolution operation as discussed in Section 2.3. Furthermore, the Sinc envelope has to be modified in order to take care of the twofold shift resulted by an imaging of a shifted (off-axis) point. Reader may refer to Chapter 2 for formulation of the PSF for a tilted beam which equivalently applies to imaging of an off-axis position. Using the results in Chapter 2 and approximations following the assumption that $\Delta\theta << \lambda_{im}/d$, the system can be modeled as in Figure 4.8.c.

The modeling outlined in Figure 4.8 is used for various system input beam configurations and the results are illustrated in Figure 4.10. PSF of the system broadens as either the imaged source is extended or the spectrum is broadened.

Figure 4.10.c,d,e plots the PSF for the imaging of an extended and off-axis source. When the source is not centered, i.e., $\theta_{scan} \neq \theta_{source}$, center of the PSF ($\theta_{center}$) deviates from the center, as expected. Also the phase ϕ_{im} which determines the positions of the diffraction lobes inside the envelope Sinc function S_1 is altered when an off-axis point is imaged.

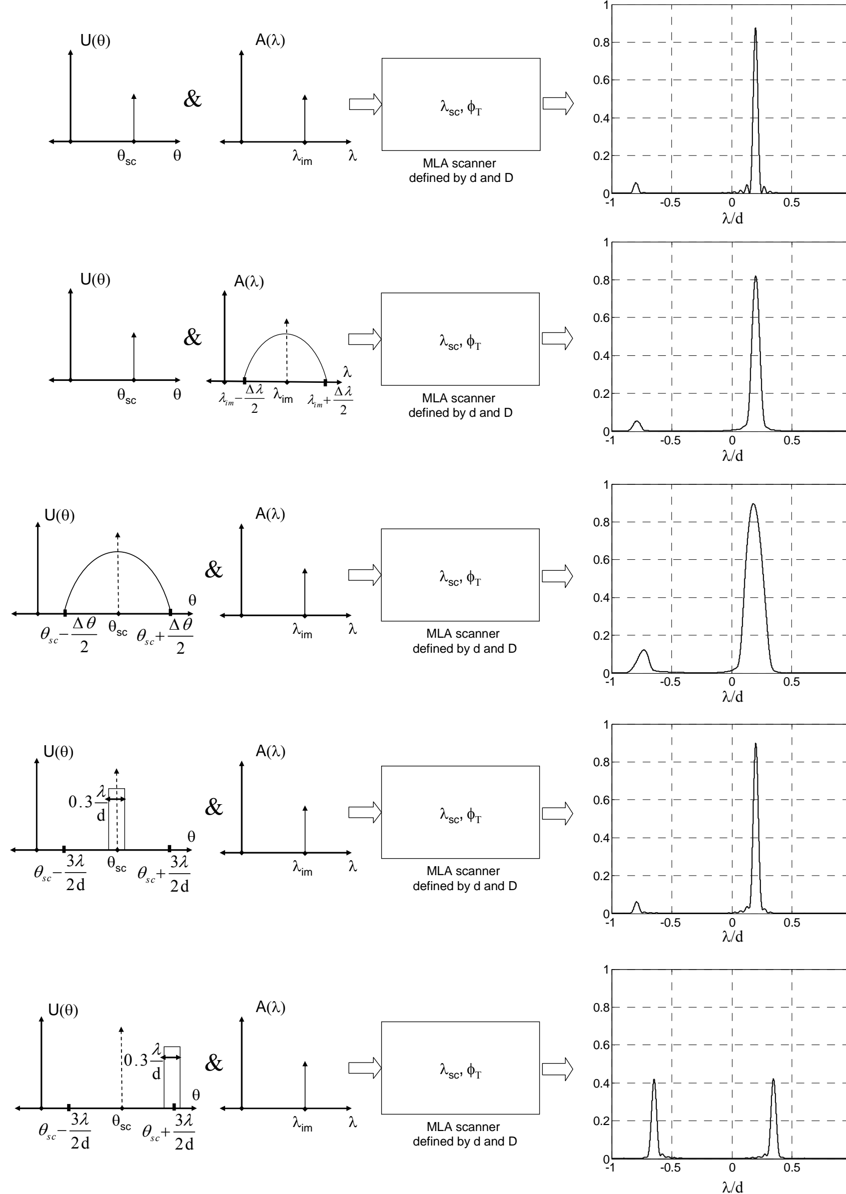

Figure 4.10: PSF_{im} of the imaging system for (a) spatially and temporally coherent sources (i.e., lasers); (b) spatially coherent; temporally incoherent (narrowband) sources i.e., laser diodes); (c) spatially incoherent (extended) and temporally coherent sources (e.g., filtered LED or narrowband fluorescence); (d) - (e) on-axis and off-axis fluorescence or LED ($m_{im}\Delta\lambda_{im} << \lambda_{im}$)

CHAPTER 5

COMPARATIVE ANALYSIS AND APPLICATIONS OF MLA SCANNERS

In this chapter a brief introduction to laser scanners is followed by a comparison of MLA scanners to mechanical and phased array scanners. Then several applications for MLA scanners are discussed.

5.1. Comparative analysis of MLA scanners

Laser scanners can be classified into two types:

(i) Phased scanners

(ii) Mechanical scanners

Phased scanners introduce phase variations to the beam and reshape a new wavefront. Since the electrically induced phase shift is limited, a diffractive phase profile where modulo 2π differences are eliminated is employed. The diffraction (i.e., interference of phase-shifted beamlets) plays an important role in this type of scanning systems. A phase modulating element introduces phase shift to different regions of a beam to resphape a new wavefront as illustrated in Figure 5.1. Electro-optical (EO) [3] and acousto-optical (AO) scanners [54] are two most common phased scanners which use two different types of phase modulating element. Among the phase modulating elements, electro-optical LC scanners have greater importance because of their higher diffraction efficiency and their relatively compact structure.

Mechanical scanners, on the other hand, illustrated in Figure 4.6, operate by displacement or rotation of an optical element [55] such as a lens [10], a mirror [57] or an optical source (e.g., fiber scanners) [58].

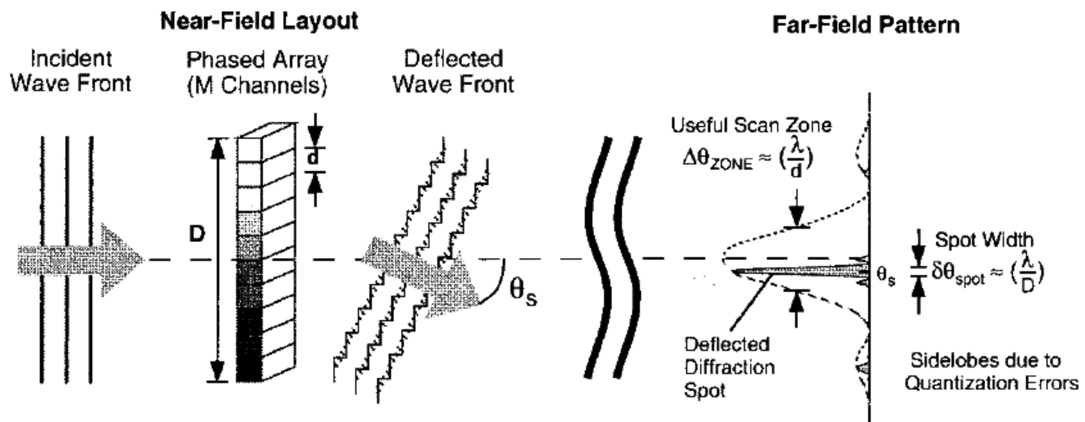

Figure 5.1: Illustrated scanning by an LC scanner [63]

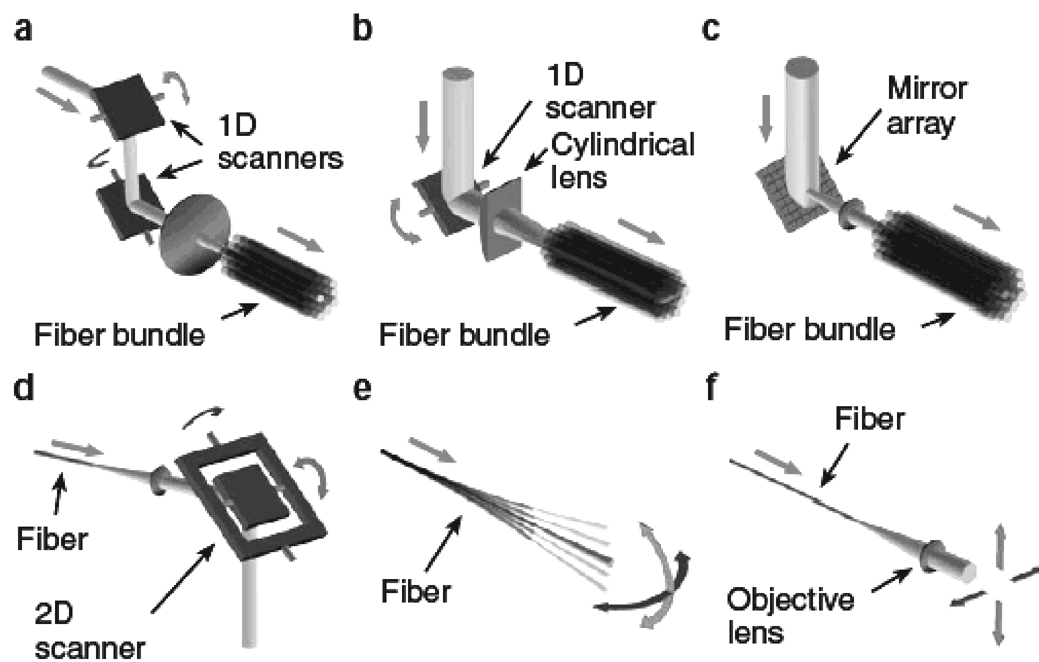

Figure 5.2: Various types of mechanical scanners [55]

Mechanical scanners achieve large deflections at high-frequencies as demonstrated by demanding applications such as wearable displays [59] that use 2D MEMS scanners and

laser printers that employ polygon scanners. For high performance, gimbal-mounted mechanical scanners are typically operated in resonance to take advantage of the high mechanical quality-factor of the device.[60] Most of the mechanical scanners such as comb driven microscanners, do not respond to DC [61] Those are not suitable for region-of-interest (ROI) scanning applications (e.g. tracking of a target) as the off-resonance or DC operation of resonant scanners yield much smaller scan angles or no scan angle, They typically suffer from large inertia, are not suitable for vector scanning (i.e., rapid scanning between two random distant positions) at very high speed.[62] Therefore, most mechanical scanners operate by raster-scanning in which the image plane is scanned line-by-line in a raster fashion. Micro-electro-mechanical system (MEMS) technology is typically employed for miniaturization and to achieve compact systems.

5.1.1. Scanning by liquid crystal (LC) phased arrays

LC beam steerers are composed of array phase shifters. An LC scanner introduces phase retardation by way of electrically-induced polarization rotation and refractive index change using the orientation of the LC molecules. The electro-optic effect is relatively weak, thus the material need to be sufficiently thick to introduce large phase differences. However, the thicker the LC material, the slower the response. Hence, most of the LC scanners are fabricated to introduce phase retardation equal to 2π (i.e., one wavelength of optical path difference).

If the angle of a plane wave transmitted through an LC element is to be tilted by a large angle θ from the normal, a phase variation greater than 2π across the beam is needed. The tilted wavefront can be approximated by subtracting integer multiples of 2π phase, e.g., $m \cdot 2\pi$, from the required phase of each pixel without changing the beam characteristics. The pixel phase levels can then be represented by a multi-level diffraction grating and

programmed into LC pixels as illustrated in Figure 5.3. The major limitation of the scheme is that it works only in one wavelength.

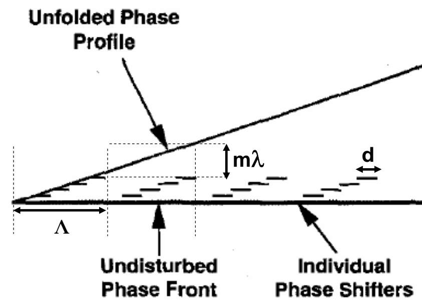

Figure 5.3: Multi-level diffraction grating approximation to a linear phase function programmed on the LC element pixels.

2π-modulo phase profile forms periodic phase ramps of pitch, Λ, such that $\tan\theta = \lambda/\Lambda$, and where m=1. Note that, the maximum steering angle, θ is limited by the pixel size δ such that $\theta_{max}=\lambda/\delta$. θ_{max} corresponds to the width of an envelope Sinc function, as illustrated in Figure 5.1. The envelope Sinc function limits the peak intensity of the beam in the image plane, and hence diffraction efficiency decreases for large scan angles.[63]

In LC beam scanning, fast switching between two scan positions (i.e. vector scanning) is possible since there is no large mechanical motion and inertia. ROI scanning is possible without reducing the data rates, which effectively increases the frame rate of the ROI imaging. Unless a complicated broadband compensation system is used, [64] phase conditions for constructive intereference can be fulfilled only at a single wavelength at a time. Hence, LC scanners can hardly be operated in broadband imaging. Many broadband and nonlinear microscopy techniques such as multi-photon imaging, optical coherence tomography where short pulses of laser needs to be delievered and spectroscopic applications such as LADAR, where broadband laser sources are utilized, are not suited for LC scanners.

At increasing scan angles, the pitch, Λ gets smaller and the fringing fields between the LC pixel cells increase. The fringing fields spoil the phase function introduced by the LC, especially where rapid phase variation appears, -i.e. at the phase jump or reset points as illustrated in Figure 5.4. The figure compares the desired phase function and the LC phase function, which suffers fringing fields at the reset position. Around the reset position, the beam is spuriously steered to a direction opposite to the desired direction. The higher the scan angle, the more optical energy is steered to undesired angles. [3], [65] At large angles LC scanners have a problem of slower switching. Also it is reported that pixelation and quantization of the field cause diffraction sidelobes [63]. There appears a trade off for the pixel size. High resolution phased array scanner systems require large number of pixels and since the pixel size has to be sufficiently large to avoid fringing fields, the high resolution LC scanner systems can not be miniaturized.

When the two beam scanning methods are compared, MLA scanning method has a number of important advantages over the LC beam scanning method:

- Higher diffraction efficiency
- Larger scanning angles
- Polarization independent scanning
- Compact design

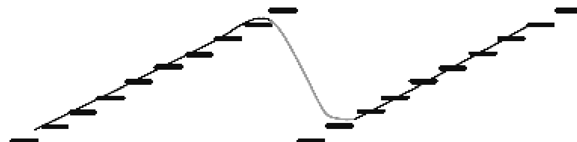

Figure 5.4: Illustrated comparison of the desired phase function and the LC phase function which suffers fringing fields at the reset position [63]

The phase profile after both the MLA and the LC systems resembles that of a blazed grating as shown in Figure 5.5. However, note that, in the MLA system the pitch of the

grating (Λ) is static and equal to the microlens size (d), i.e., $\Lambda = d$. In the LC scanning system Λ and the blaze angle, γ, are dynamic, while in the MLA system only blaze angle, γ, is dynamic. Therefore constructive diffraction conditions are not satisfied for all scanning angles and one should introduce a phase differences between microlens channels. Figure 5.6 illustrates the phase profiles for fulfilling the constructive interference condititions (i.e. continuous wavefront conditions).

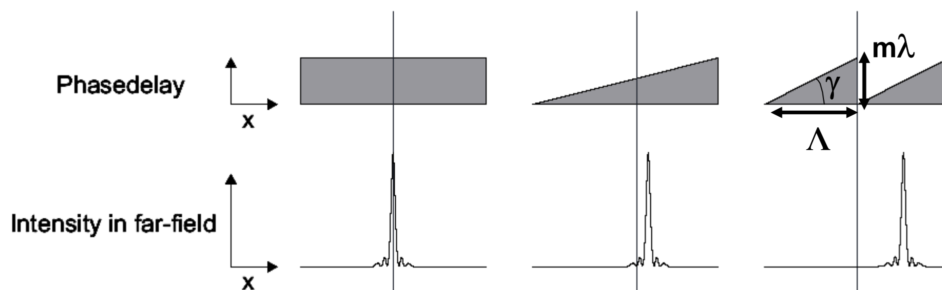

Figure 5.5: Illustration of blazed angle beam steering

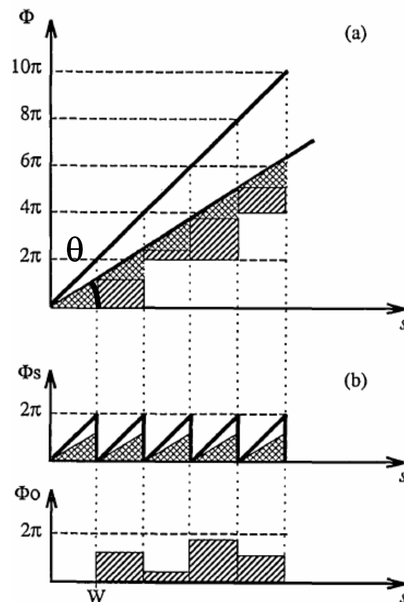

Figure 5.6: Phase profile for two steering angles. Illustrates that the phase profile can be obtained by superimposing a blazed and an offset phase function

5.1.2. Continuous Line Addressing with MLA Scanners

An alternative to using the PSL for continuous scanning with MLAs is to use an LC phase shifter as illustrated in Figure 5.7. [9] But in that case the LC element would need to be imaged on to the MMLA. As MMLA is the moving component in our system, either the LC would need to move together with the MMLA or DMLA would need to be made movable. Either way, this would slow down the system and introduce artifacts due to LC element limitations.

An alternative and intuitive method for continuous scanning using MLA scanners is reported previously. [69] The method steers the beam after MLA system and provide full-line scanning without altering the phase of the beamlets output from microlens channels. It merely re-scan the beam after the MLA scanning system as shown in Figure 5.8. However the scheme needs folding of the beam and the working distance, which is defined as the distance between the last optical element and the focal plane, is significantly reduced.

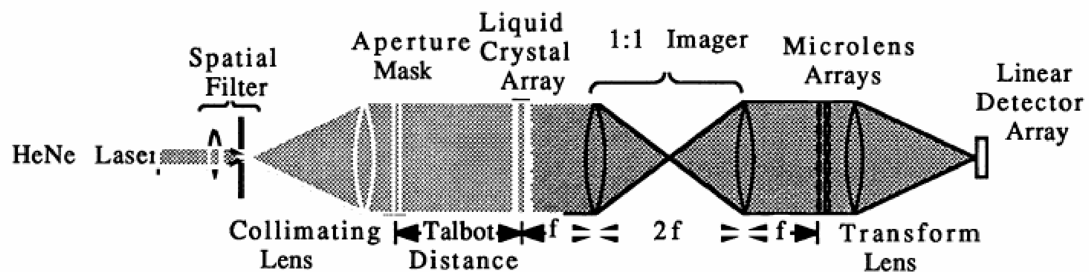

Figure 5.7: Schematic representation of the continuous beam steering using LC phase shifters [9]

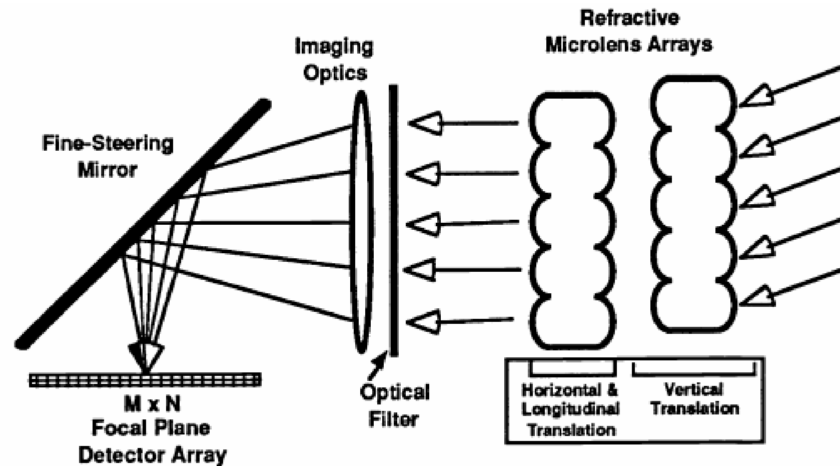

Figure 5.8: Schematic representation of the continuous beam steering using a scanning mirror after the MLA scanning system [69]

5.1.3. MLA Scanning System Comparison with Phased-Array and Mechanical Scanners

MLA scanners differ greatly from other laser scanners. In MLA scanning systems, beam scanning is obtained by scanning of beamlets by lens displacement and diffraction of these beamlets. MLA scanners are similar to LC scanners in output phase profile, however, the main difference is the mechanical actuation, , which slows down the system, In contrast to pixellated LC structures, the MLA scanners can be miniaturized and without suffering from degradations in diffraction efficiency and scan angle.

On the other hand, with their unique nature, which enables large scan angles to be obtained at small lateral deflections and low inertia design, they have a number of advantages over other mechanical scanners such as micromirror scanners and fiber scanners.

In the MLA scanner system the MMLA is laterally actuated for beam steering, while the micromirror scanners steer beam by torsinal actuation. Figure 5.9 illustrates different natural vibration modes of a flexure mounted scanner. Lateral actuation can be obtained by

using electrostatic comb structures. In Figure 5.10 a comb-driven lateral actuated system is represented. In torsional actuation the structure rotates around anchored beams. Figure 5.11 is a torsinal actuated MEMS design for micromirror scanning. [70] Lateral actuation approach has a number of advantages over the torsional actuation:

- there exists a linear relationship between applied voltages and the generated electrostatic forces/torque
- at atmospheric pressure, higher quality factor (Q) can be achieved, because of lower damping, that is related to reduced cross section in lateral direction
- complicated system geometries can be designed without adding processing steps

Another limitation of micromirror scanners is that the switching times is >100µsec, making them not suitable for vector scanning. [71]

A system related advantage of MLA scanning approach is that optical beam is not folded. Beam folding is not desired in cases where miniaturization of the system and forward-looking scanning is desired, e.g., in most endoscopic applications. MLA scanning system is a forward-looking scanning system, whereas in micromirror scanning the beam is folded. Evenif, there is at least one forward-looking system using a special micromirror scanner designed by well-known company Olympus, they suffer from small field-of-view and low pixel count.[52]

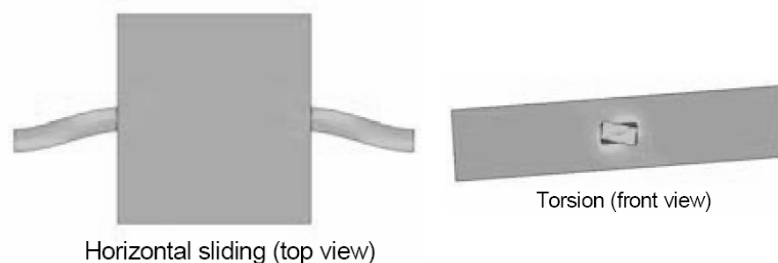

Figure 5.9: Lateral sliding and torsional vibration modes of a flexure mounted scanner [72]

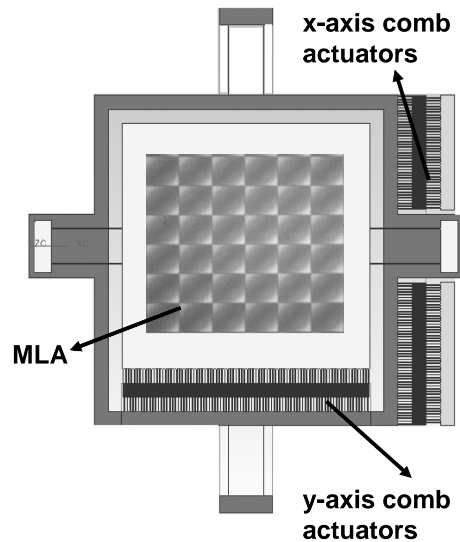

Figure 5.10: Representation of lateral MEMS actuation for MLA beam scanners

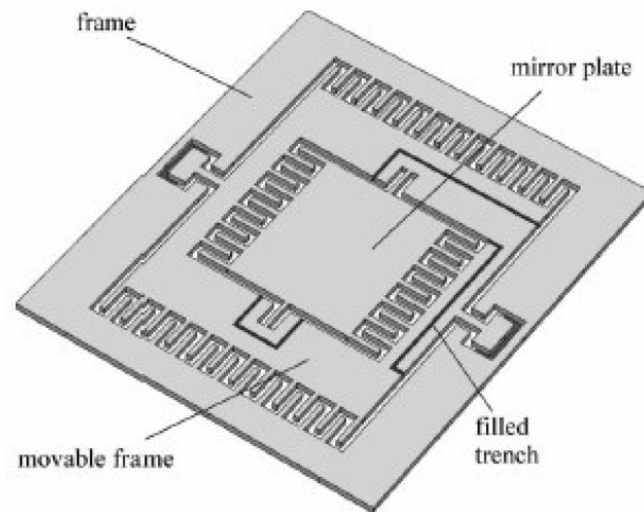

Figure 5.11: A torsional MEMS actuation for micromirror scanner [70]

The maximum scan angle, θ_{max}, of an MLA system is dependent on the ratio of the focal length and the size of the microlenses in DMLA, -i.e., $f_{\#}$ of the DMLA ($f_{\#,\mathrm{MLA}}$).

$$\theta_{\max} = \frac{1}{2 f_{\#,MLA}} \tag{5.1}$$

The amount of displacement required for achieving a given θ_{max} can be shown to be independent of the beam size in case of MLA scanners, however, the mirror tip displacement increase linearly with the mirror size in mirror scanners. Furthermore, displacement direction in micromirror scanners is perpendicular to the structure being scanned, whereas in MLA scanners the displacement and the structure are in the same plane. Micromirror scanners need to be reinforced and sufficiently thick to avoid dynamic mirror deformation. Increased thickness also require larger actuation forces, wehereas in MLA scanners, the substrate can be much thinner as dynamic deformation is not an issue, reducing the actuation force requirements. PSF of an optical scanning system is reported to be highly vulnerable to mechanical deformations as shown in Figure 5.12. [73]

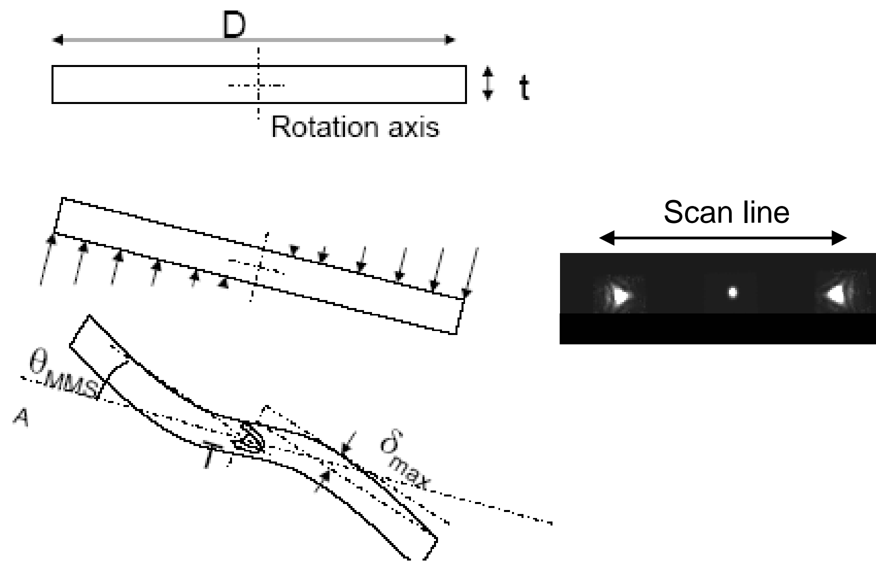

Figure 5.12: Deformation of micromirror scanner and the degration of the PSF at large scan angles due to large acceleration forces at the extremities of the scan.

Diffraction limited resolution of a scanning system is highly dependent on the size of the beam, -i.e., clear aperture of the scanning structure. As stated before, MLA scanners can steer very large beams with very small displacements regardless of the beam size. This would let MLA scanners to be used in large beam scanning (> 1 cm) applications where motors might be used for actuation of the MLA. In such a case, torsional scanning is not efficient because of increasing acceleration at the tip of the scanning mirror and the resulting dynamic deformation.

5.2. MLA scanner applications

Due to different performance trades, the best laser scanner technology is application specific. MLA scanners have a unique structure which combines both scanning by lateral displacement and the diffraction of the beamlets. They suit better to applications that demand high resolution/large field of view, large beam, vector, or ROI scanning, or when a compact system is desired. However, their use is mostly limited to coherent laser sources. Although the requirements are quite different, the following applications seem to be the best suited for implementation with MLA scanners: biomedical endoscopic imaging [52]; infrared countermeasure applications (IRCM) [8] and scanning laser Doppler vibrometry (SLDV).

5.2.1. Endoscopic imaging

In certain endoscopic imaging applications, a forward looking and large field of view scanning is desired. The scanning system is also needed to fit into a tiny tube (e.g., $\phi <$ 5mm). In Laser scanning microscopy, the images are reconstructed by scanning a focused laser spot on the surface or subsurface of a tissue. Confocal laser scanning microscopy illuminates and collects light from a single position at a time. This type of imaging greatly

improves the image quality compare to flood illumination approach where whole the image plane is illuminated and inter-pixel coupling of the light degrades the image quality. However, in confocal laser scanning microscopy light collection efficiency is very low [74]

MLA scanner system is a dispersive system as the phase condition is valid only for one wavelength at a time. Dispersion compensation is not possible since the laser is scanned through many diffraction orders.[9] Thus the MLA scanning system can not be used for confocal imaging with broadband sources and emitters. Furthermore, ultra-short pulse imaging techniques (i.e., short coherence length) such as optical coherence tomography and multi-photon microscopy is not possible with MLA scanners because of the dispersive nature. However, dispersive nature of the MLA scanner can be utilized for spectral analysis of the fluorescence light. Also the system can be used for confocal imaging of the backscattered light, which is at the same wavelength as the excitation.

In imaging systems where biomarkers such as fluorescence molecules, [75] resonant metallic nanoshperes, [76] are used the back emitted light from a tissue can be collected by the MLA scanning system and focused on the detector plane which is at the focus of the PSL. Alternatively the back emitted light can be collected by multi-mode fibers positioned nearby the imaging lens. Figure 5.13 and Figure 5.14 illustrates a similar system which uses multi-mode fibers for collection of the light.[77]

The PSF of the system in the detector plane, for back emitted light depends on the fluorescence wavelength and on the system parameters such as: excitation wavelength, the displacements in the system (e.g., of PSL and MMLA). The PSF analysis is reported in Chapter 2 and shown that the PSF is composed of four diffraction lobes. Spectroscopic information regarding the collected light can be obtained by using the system displacement values and the distribution of the PSF at the detector plane e.g., positions of or the ratio of optical power on the diffraction lobes. For measuring PSF distribution position sensing

detectors or a quadrant photo diode for measuring the intensity on each diffraction lobe can be utilized.

Alternatively for efficient collection of light, in expense of spectroscopic information, a single large detector such as avalanche photo detector or photo-multiplier tube, can be used in the detector plane. To further improve light collection efficiency additional detectors or fibers positioned nearby the scanning system can be employed.

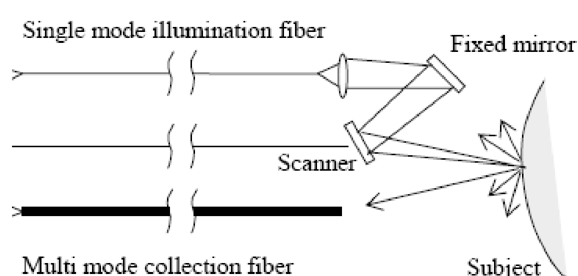

Figure 5.13: Schematic representation of an endoscobic system where multi-mode fibers employed [77]

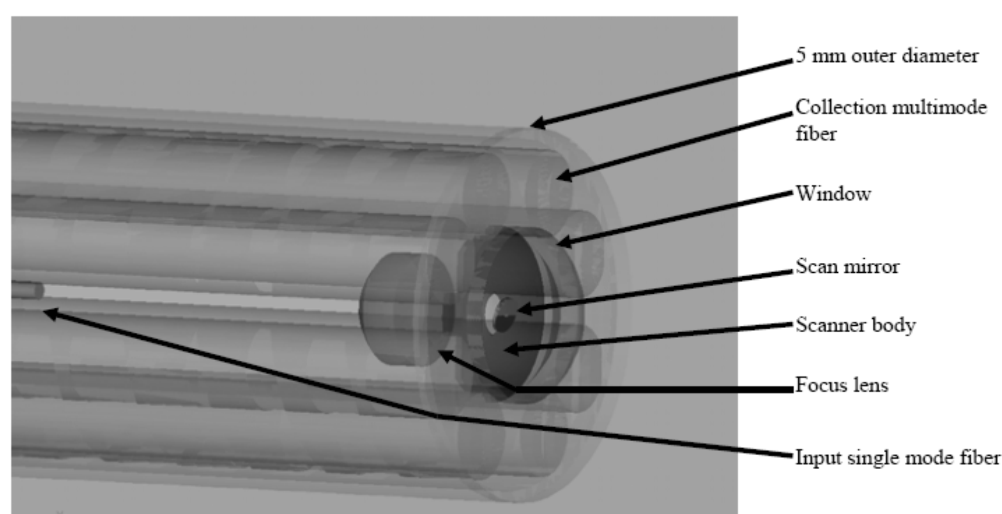

Figure 5.14: Endoscopic imaging system using multi-mode fiber nearby the scanning elements for collection of light [77]

5.2.2. Infrared countermeasure (IRCM)

Infrared countermeasure (IRCM) systems are designed to detect and jam surface-to-air and air-to-air missile threates. [78] Initially large mechanical beam-steering devices; e.g., dual-axis gimbaled mirror systems were used for this application. A recent interest was in designing a highly accurate and rapid random pointing system. [8] In a recent study [8] by Air Force Research Laboratory, three-lens system shown in Figure 2.1 was used instead of the three-MLA system. They mentioned that the MLA scanning system steers light to multiple orders and suffers undesired diffraction of light into spurious directions at the output. The PSL scanning proposed in this thesis solves the mentioned problems of the MLA scanning system and makes the system eligible for that application as well.

IRCM applications require random steering of a large beam precisely over wide angles, i.e., vector scanning. As discussed above MLA scanning systems can be designed for high-resolution vector scanning. High precision required in IRCM might require closed loop control and position sensor for the scanning stages.

IRCM systems use single line laser source for jamming the missile tracking system and detect broadband sources. As discussed and analyzed MLA scanning system can steer the narrowband, jamming laser signal and track the missile.

Rough broadband detection of a target radiating in MWIR is needed for IRCM. Detection of the target is followed by precise positioning of the target and jamming. As analyzed in Chapter 4, MLA scanning system can detect a broadband signal and determine its spectral components by mere scanning of MMLA. Then, the system can precisely position the target by combined scanning of MMLA and PSL.

Figure 5.15 illustrates a scanning scheme for IRCM taken from a report which proposes the use of three-lens scanning system for IRCM. The report is prepared by a collaborative research team leaded by Kent University. The system in the figure uses LC beamsteerers cascaded with MLA scanner, however no other information is given related to system

design and performance. We believe that for IRCM MLA scanners are used with a cascaded low deflection scanning system e.g., LC scanner. As outlined above, the MLA scanning offer important advantages compared to LC scanners, thus can be a better choice for this application.

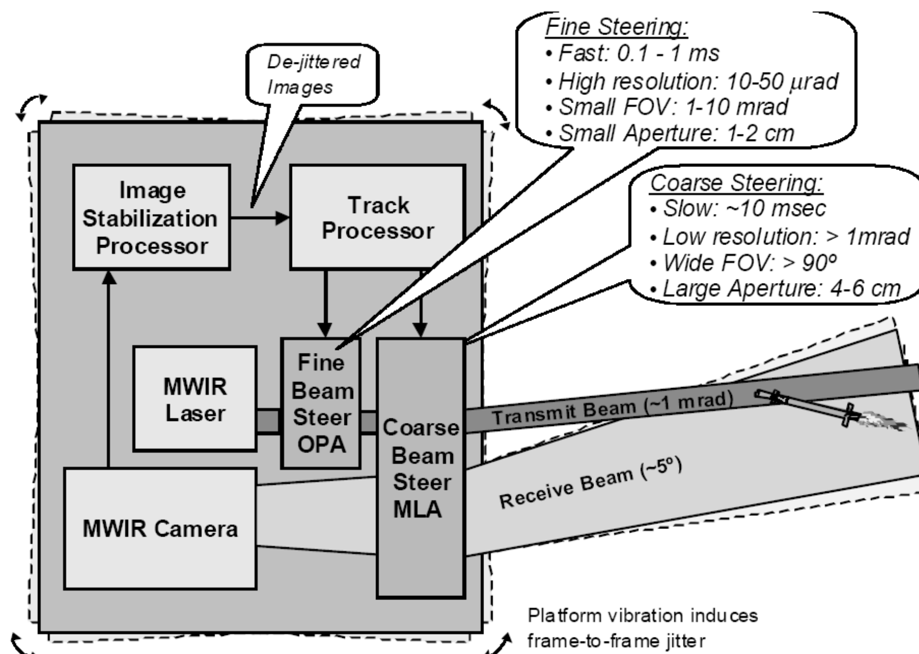

Figure 5.15: IRCM system for detection and jamming of missile [79]

5.2.3. Scanning laser Doppler vibrometer (SLDV)

MLAs can be utilized in applications where rapid discrete addressing is needed, such as the scanning laser Doppler vibrometer (SLDV). [80] The SLDVs are used for measuring of vibration of a system by scanning a laser onto some sample positions on a surface. MLA scanners can be employed for SLDV. For this particular application, discrete addressing is required, therefore, the PSL scanning is not needed and the system is much simpler. Figure 5.16 and Figure 5.17 illustrates a grid of scanned positions on the targer area and the scanning mechanism composed of gimbaled mirror scanners.

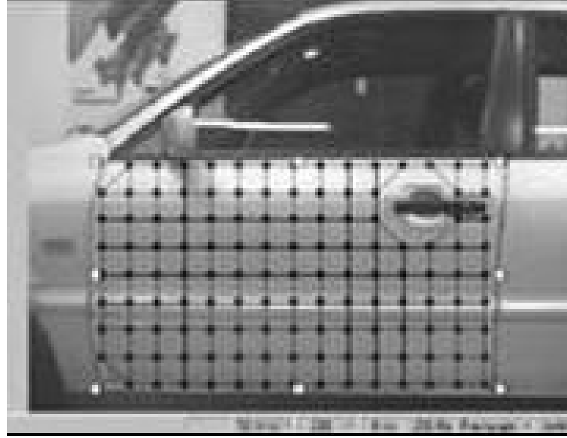

Figure 5.16: The scan head of an SLDV system contains an LDV sensor, a live color video-camera and xy deflection mirrors. [80]

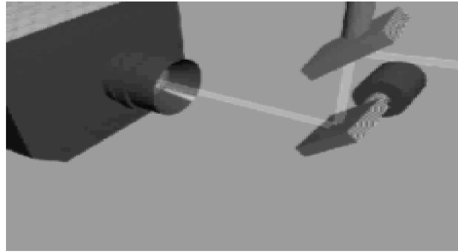

Figure 5.17: The deflection mirrors can automatically direct the laser beam to the desired positions on a user-defined area. [80]

The number of addressable points by mere scanning of MMLA is:

$$N_{discrete} = \frac{d}{\lambda f_{\#,MLA}} \tag{5.2}$$

For d=400µm, λ=0.632µm, and $f_{\#}$=5 the number of points $N_{discrete}$=126. In 2-D 126×126=15,876 spots can be addressed. The maximum scan angle is found to be 5.7^0. The maximum scan angle can be doubled independent of the resolution $N_{discrete}$, by doubling the $f_{\#,MLA}$ and d together.

CHAPTER 6

CONCLUSIONS

In this work, a new laser scanning system based on lateral displacements of microlens arrays (MLA) is designed and demonstrated. The main advantages of the proposed scheme are the compactness and the high-resolution offered by only small deflections of the mechanical actuator. The proposed scheme overcomes the diffraction related limitations of MLA scanning systems using a prescan lens (PSL) and demonstrates continuous addressability with MLAs for the first time. [81]

The proposed laser scanning system is presented to have novel imaging capabilities. The system can be utilized for concurrent detection spectral and spatial distribution of an imaged source. The system is presented to have potential applications in endoscopic imaging, target detection, and vector scanning.

Analytical and numerical results regarding the operation of the MLA scanning system and the use of the PSL in addressing positions between discrete diffraction positions are demonstrated experimentally.

A novel modeling and simulation method is suggested for simulation and optimization of the periodical optical structures and the method applied for optical performance optimization of the MLA laser scanners. It is concluded that system performance is dependent both on the aberration and diffraction performance of the system. For best system performance, aspherical MLAs having nearly perfect fill-factor have to be utilized, especially for designs employing low $f_{\#}$, (e.g. $f_{\#} < 5$) MLAs.

Different actuation mechanisms are suggested. For both the MEMS and the LC implementation, high speed scanning and data acquisition is possible.

The proposed scheme is particularly well-suited for forward-looking endoscopic imaging applications, where the optics and the actuator have to fit in a small tube of

diameter 5mm, scanning laser-Doppler-vibrometry, and for applications where a large clear aperture and fast actuation is needed such as target detection and tracking in infrared.

A comparison of the proposed system with a commercial forward-looking endoscopic imaging system [82] recently developed by Olympus is given in Table 6.1. As can be seen, our proposed system has the potential to provide region of interest imaging capability and higher resolution while maintaining the high data rates. The table assumes the system is actuated using MEMS. In another project, the actuator development is in progress in Optical Microvision Laboratories and funded by Tübitak.

System Features	**Olympus Corp. System**	**Koc Uni. System**
Resolution	200	**>1,000**
Spot size	0.5μm	**0.5μm**
Scan range	100x100 μm^2	**500x500 μm^2**
Scanning mechanism	MEMS scanning mirror	**MEMS integrated MLA**
Scanning Angle (Optical)	±6°	**±12° (with *f*/4 microlens arrays)**
MEMS scanner size	0.5 mm (mirror)	**2 mm (MLA)**
Frame rate	20	**Max. resolution: 1** **Region of interest: >30**
Data rate	800,000	**1,000,000**

Table 6.1: Comparison of the proposed system with a recent endoscope technology developed by Olympus

REFERENCES:

[1] H Miyajima, K Murakami, M Katashiro “MEMS Optical Scanners for Microscopes” IEEE, Selected Topics in Quantum Electronics, 10, 3 (2004) 514-527

[2] Caglar Ataman, Hakan Urey, “Modeling and characterization of comb actuated resonant microscanners,” J. Micromechanics and Microengineering, Vol. 16, (2006), 9-16

[3] D. P. Resler, D. S. Hobbs, R. C. Sharp, L. J. Friedman, and T. A. Dorschner, "High-efficiency liquid-crystal optical phased-array beam steering," Opt. Lett. 21, (1996), 689

[4] Steffen Glöckner, Rolf Göring, Torsten Possner."Micro-opto-mechanical beam deflectors", Opt. Eng. 36, (1997), 1339

[5] G. F. McDearmon, K. M. Flood, and J. M. Finlan, ‘‘Comparison of conventional and microlens-array agile beam steerers,’’ Proc. SPIE 2383, (1995), 167–178

[6] M He, X-C Yuan, N Q Ngo, J Bu and S H Tao, “Single-step fabrication of a microlens array in sol–gel material by direct laser writing and its application in optical coupling” J. Opt. A: Pure Appl. Opt. 6 (2004), 94-97

[7] E. A. Watson, ‘‘Analysis of beam steering with decentered microlens arrays,’’ Opt. Eng. 32, 11, (1993), 2665-2670

[8] JL Gibson, BD Duncan, EA Watson, JS Loomis, “Wide-angle decentered lens beam steering for infrared countermeasures applications”, Optical Eng., 43, 10, (2004), 2312-2321

[9] Kevin M. Flood, William J. Cassarly, Christina Sigg, and J. Michael Finlan “Continuous Wide-Angle Beam Steering Using Translation of Binary Microlens Arrays and a Liquid Crystal”, Proc. SPIE, Computer and Optically Formed Holographic Optics, Ivan Cindrich, Sing H. Lee, Editors, (1990), 296-304

[10] S. Kwon, and L. Lee, “Stacked Two Dimensional Microlens Scanner for Micro Confocal Imaging Array”, 15th Annual IEEE International MEMS 2002 Conference, 1/20-24/02, Las Vegas, (2002), 483-486

[11] Caglar Ataman, Yves Petremand, Wilfried Noell, Hakan Urey, Nico F. de Rooij, “A 2D MEMS Stage for Optical Applications,” in MEMS, MOEMS, and Micromaching, Proc. SPIE Vol. 6186, Strasbourg-France, April 2006.

[12] Jacques Duparré, Daniela Radtke, Peter Dannberg, “Implementation of Field Lens Arrays in Beam-Deflecting Microlens Array Telescopes” Applied Optics, 43, 25 (2004) 4854-4861

[13] E. A. Watson, “Analysis of beam steering with decentered microlens arrays,” Opt. Eng. 32, 2665–2670, (1993).

[14] A. Akatay, C. Ataman, and H. Urey, "High-resolution beam steering using microlens arrays," Opt. Lett. 31, 2861-2863 (2006)

[15] Computer-simulated Fresnel diffraction using the Fourier transform. Computing in Science and Engineering, 1(5):77-83, September/October 1999.

[16] J.W. Goodman *Introduction to Fourier Optics*, (McGraw-Hill, New York, 1996).

[17] Wigner, E., 1932, Phys. Rev., 40, 749.

[18] Image rotation, Wigner rotation, and the fractional Fourier transform - AW Lohmann - Image, 1993 – OSA

[19] D. Mendlovic, Z. Zalevsky, and N. Konforti, “Computation considerations and fast algorithms for calculating the diffraction integral” J. Mod. Opt. 44, (1997), 407.

[20] H. Urey, K. Powell, "Microlens-array-based exit-pupil expander for full-color displays," Appl. Opt. 44, (2005), 4930-4936

[21] S. K. Park, R. A. Schowengerdt, and M. -A. Kaczynski, "Modulation-transfer-function analysis for sampled image systems," Appl. Opt. 23, (1984), 2572

[22] A. Akatay, C. Ataman, and H. Urey, "High-resolution beam steering using microlens arrays," Opt. Lett. 31, (2006), 2861-2863

[23] D. Faklis and G. M. Morris, "Spectral properties of multiorder diffractive lenses," Appl. Opt. 34, (1995), 2462

[24] H. Urey, “Spot size, depth of focus, and diffraction ring intensity formulas for truncated Gaussian beams,” Appl. Opt., 43, (2004), 620

[25] Hakan Urey and Frederick B. McCormick, “Aberration accumulation for imaging through high resolution thick media” Algorithms, Devices, and Systems for Optical Information Processing, Bahram Javidi, Ed., Proc. SPIE, vol. 3159, San Diego, California, August 1997.

[26] H. Urey, “Retinal Scanning Displays”, in Encyclopedia of Optical Engineering, R. G. Driggers, ed. (Marcel Dekker, New York, 2003), pp. 2445-2457.

[27] Ko, Chih-Hsiang; Lin, Chun-Hsu; Tsai, Bor-Chen; Shih, His-Hsin; Wu, Chien-Tsung; Chao, Yu-Lin; Chou, Yu-Kon; Chu, Chun-Hsun; Chiou, Yii-Tay; Chen, Rax “Development of microlens arrays for high-speed optical communication” Proc. SPIE, 5454, Micro-Optics, VCSELs, and Photonic Interconnects. Edited by Thienpont, Hugo; Choquette, Kent D.; Taghizadeh, Mohammad R., (2004), 121-128.

[28] Lingbin Kong, Xinjian Yi, Ke Lian and Sihai Chen “Design and optical performance research of multi-phase diffractive microlens arrays”, J. Micromech. Microeng. 14, (2004), 1135-1139

[29] F. Nikolajeff, S. Hrd, and B. Curtis, "Diffractive microlenses replicated in fused silica for excimer laser-beam homogenizing," Appl. Opt. 36, (1997) 8481-8489

[30] K. M. Mahoney and A. M. Weiner, “Modified femtosecond pulse shaper using microlens arrays”, Opt. Lett. 21, (1996) 812-814

[31] Javidi, Bahram; Matoba, Osamu; Tajahuerce, Enrique, “Three-dimensional object recognition based on multiple-perspective imaging with microlens arrays”, Proc. SPIE, 4564, Optomechatronic Systems II, Hyung S. Cho; Ed., (2001) 1-12

[32] A. Akatay, A. Waddie, H. Suyal, and M. Taghizadeh, H. Urey “Comparative performance analysis of 100% fill-factor microlens arrays fabricated by various methods”

Proc. SPIE, 6185, Micro-Optics, VCSELs, and Photonic Interconnects II. Edited by Thienpont, Hugo; Taghizadeh, Mohammad R., (2006)

[33] M. He, X-C Yuan, N. Q. Ngo, J. Bu and S. H. Tao “Single-step fabrication of a microlens array in sol–gel material by direct laser writing and its application in optical coupling” J. Opt. A: Pure Appl. Opt. 6 (2004), 94-97

[34] A Akatay, A Waddie, H Suyal, M Taghizadeh, H Urey “Comparative performance analysis of 100% fill-factor microlens arrays fabricated by various methods” – Proc. of SPIE, Micro-Optics, VCSELs, and Photonic Interconnects II: Fabrication, Packaging, and Integration, H.Thienpont, M.Taghizadeh, PDaele, JMohr, Eds., (2006)

[35] Moon, Su-dong; Kang, Shinill; Bu, Jonguk, “Fabrication of polymeric microlens of hemispherical shape using micromolding” Optical Engineering 41(09), (2002), 2267-2270

[36] H. Hashimoto, S. Tanaka, K. Sato, I. Ishikawa, S. Kato, N. Chubachi. “Chemical Isotropic Etching of Single-Crystal Silicon for Acoustic Lens of Scanning Acoustic Microscope”, Japan J. Appl. Phys. 32, (1993), 2543-2546

[37] Hisayoshi Hashimoto, Shinji Tanaka, Kazuo Sato, Isao Ishikawa, Sigeo Kato and Noriyoshi Chubachi, “Chemical Isotropic Etching of Single-Crystal Silicon for Acoustic Lens of Scanning Acoustic Microscope” Jpn. J. Appl. Phys. Vol. 32 (1993) 2543-2546

[38] R. W. Tjerkstra. “Isotropic etching of silicon in fluoride containing solutions as a tool for micromachining” Univ. Twente, The Netherlands, 1999.

[39] D. Faklis and G. M. Morris, "Spectral properties of multiorder diffractive lenses," Appl. Opt. 34, (1995) 2462

[40] O. Yuzo, N. Nobuo, “Systematic design method for holographic zone plates with aberration corrections”, Applied Optics, 26, (1987), 1137-1141

[41] I. Kallioniemi, J. Saarinen, K. Blomstedt, and J. Turunen, “Polygon approximation of the fringes of diffractive elements”, Applied Optics. 36, 7217 1997

[42] D Daly, R F Stevens, M C Hutley, N Davies, “The manufacture of microlenses by melting photoresist ”. Meas. Sci. Technol. 1, (1990), 759-766

[43] Hsiharng Yang, “High fill-factor microlens array mold insert fabrication using a thermal reflow process” *J. Micromech. Microeng.* 14 (2004), 1197-1204

[44] K. Wei, I.-L. Su, M.-C. Jung, K.-W. Huang, "Real-time observation for the formation of microlens arrays using thermal reflow process", Tamkang Journal of Science and Engineering, 7, (2004), 81-86

[45] M. 1. Gale, M. Rossi, J. Pedersen, H. SchUtz. “Fabrication of continuous-relief micro-optical elements by direct laser writing in photoresists”, Opt. Eng. 33, (1994), 3556-3566.

[46] H. Urey, K. Powell, "Microlens-array-based exit-pupil expander for full-color displays," Appl. Opt. 44, (2005), 4930-4936

[47] H. Ra, W. Piyawattanametha, Y. Taguchi, and O. Solgaard, “Dual-Axes Confocal Fluorescence Microscopy with a Two-Dimensional MEMS Scanner” IEEE/LEOS International Conference on Optical MEMS, Aug (2006)

[48] http://www.telescope-optics.net/contrast2.htm

[49] H Miyajima, K Murakami, M Katashiro “MEMS Optical Scanners for Microscopes ” IEEE, Selected Topics in Quantum Electronics, 10, 3 (2004) 514-527

[50] Caglar Ataman, Hakan Urey, “Modeling and characterization of comb actuated resonant microscanners,” J. Micromechanics and Microengineering, Vol. 16, (2006), 9-16

[51] D. P. Resler, D. S. Hobbs, R. C. Sharp, L. J. Friedman, and T. A. Dorschner, "High-efficiency liquid-crystal optical phased-array beam steering," Opt. Lett. 21, 689- (1996)

[52] K. Murakami, “A miniature confocal optical scanning microscope for endoscope,” in MOEMS Display and Imaging Systems III, H. Urey and D. L. Dickensheets, eds., Proc. SPIE 5721, 119-131 (2005).

[53] JL Gibson, BD Duncan, EA Watson, JS Loomis, “Wide-angle decentered lens beam steering for infrared countermeasures applications”, Optical Eng., 43, 10, (2004), 2312-2321

[54] S. Zeng, X. Lv, C. Zhan, W. R. Chen, W. Xiong, S. L. Jacques, and Q. Luo, "Simultaneous compensation for spatial and temporal dispersion of acousto-optical deflectors for two-dimensional scanning with a single prism," Opt. Lett. 31, 1091-1093 (2006)

[55] B. A. Flusberg, E. D. Cocker, W. Piyawattanametha, J. C. Jung, E. L. M. Cheung, and M. J. Schnitzer,"Fiber-optic fluorescence imaging" Nat. Meth. 2, (2005), 941

[56] S. Kwon, and L. Lee, “Stacked Two Dimensional Microlens Scanner for Micro Confocal Imaging Array”, 15th Annual IEEE International MEMS 2002 Conference, 1/20-24/02, Las Vegas 483-486, (2002)

[57] H. Urey, “Retinal Scanning Displays”, in Encyclopedia of Optical Engineering, R. G. Driggers, ed. (Marcel Dekker, New York, 2003), 2445-2457.

[58] X. Liu, M. J. Cobb, Y. Chen, M. B. Kimmey, and X. Li, "Rapid-scanning forward-imaging miniature endoscope for real-time optical coherence tomography," Opt. Lett. 29, (2004), 1763-1765

[59] www.microvision.com

[60] A.D. Yalcinkaya, H. Urey, T. Montague, D. Brown, and R. Sprague "Two-axis Electromagnetic Microscanner for High Reslolution Displays ", IEEE/ASME Journal of Microelectromechanical Systems, Vol 15, Issue 4, August, 2006.

[61] Caglar Ataman, Hakan Urey, “Modeling and characterization of comb actuated resonant microscanners,” J. Micromechanics and Microengineering, Vol. 16, (2006) 9-16

[62] V. Milanovic, K. Castelino, “MEMS-Based High-Speed Low-Power Vector Display”Proc. of IEEE/LEOS Optical MEMS (2005)

[63] J. A. Thomas and Y. Fainman, "Optimal Cascade Operation of Optical Phased-Array Beam Deflectors" Appl. Opt. 37, (1998) 6196-6212

[64] McManamon, P.F.; Watson, E.A. “Design of optical phased array beam steering with limited dispersion” vol.3 (2001), 1583-1591

[65] Paul McManamon, “Solid-state phase shifters steer optical beams for laser communications and radar”, OE Magazine, April (2003) 15-17

[66] F. Vasey, F. -K. Reinhart, R. Houdre, and JM Stauffer, "Spatial optical beam steering with an AlGaAs integrated phased array," Appl. Opt. 32, (1993), 3220-

[67] E. A. Watson, ‘‘Analysis of beam steering with decentered microlens arrays,’’ Opt. Eng. 32, 11, (1993), 2665-2670

[68] Kevin M. Flood, William J. Cassarly, Christina Sigg, and J. Michael Finlan “Continuous Wide-Angle Beam Steering Using Translation of Binary Microlens Arrays and a Liquid Crystal”, Proc. SPIE, Computer and Optically Formed Holographic Optics, Ivan Cindrich, Sing H. Lee, Editors, (1990), 296-304

[69] Graham F. McDearmon, Kevin M. Flood, and J. Michael Finlan, “Comparison of conventional and microlens-array agile beam steerers” Micro-Optics/Micromechanics and Laser Scanning and Shaping, M. Edward Motamedi, Leo Beiser, Editors, (1995) 167-178

[70] H. Schenk, P. Dürr, D. Kunze, H. Lakner, H. Kück, “A resonantly excited 2D microscanning-mirror with large deflection,” Sensors and Actuators A, 89,
(2001), 104-111

[71] V. Milanovic, K. Castelino, “Sub 100 us Settling Time and Low Voltage Operation
for Gimbal-less Two-Axis Scanner” Proc. of IEEE/LEOS Optical MEMS (2004)

[72] Hakan Urey, Cihan Kan, Wyatt O. Davis, “Vibration mode frequency formulae for micromechanical scanners,” J. Micromechanics and Microengineering, 15, 2005, 1713-1721

[73] Hakan Urey, “High performance resonant MEMS scanners for display and imaging applications” in Optomechatronic micro/nano components, devices, and systems conference, Proc. SPIE, Vol. 5604, Philadelphia, Pennsylvania, (2004)

[74] Sheppard CJR (2003) Scanning confocal microscopy, in Encyclopedia of Optical Engineering, Dekker, New York, ISBN: 0-8247-4258-3, pp. 2525-2544

[75] Feng Wang, “Luminescent nanomaterials for biological” *Nanotechnology* 17 R1-R13 (2006),

[76] Schultz DA. “Plasmon resonant particles for biological detection.” Curr Opin Biotechnol., 14(1).(2003) 13-22

[77] John R. Lewis, Mark Holton, Martin Kykta, Amjad Malik, Frank Metting, Chris Ryerson, Chris Wiklof, and Jianhua Xu , “Scanned beam medical imager” Proc. of SPIE, MOEMS Display and Imaging Systems II, Hakan Urey, David L. Dickensheets, Editors, 5348, (2004), 40-51

[78] DP Forrai, JJ Maier, “Generic models in the advanced IRCM assessment model” IEEE, Proc. 33rd conf. on winter simulation (2001) 789-786

[79] Special Report. Kent-State-University, “Liquid Crystal Based Optical Phased Array for Steering Lasers”

[80] http://www.dipmec.unian.it/misure/strumenti/LDV/ldv_en.html

[81] A. Akatay, C. Ataman, and H. Urey, "High-resolution beam steering using microlens arrays," Opt. Lett. 31, (2006), 2861-2863

[82] K. Murakami, “A miniature confocal optical scanning microscope for endoscope,” in MOEMS Display and Imaging Systems III, H. Urey and D. L. Dickensheets, eds., Proc. SPIE 5721, (2005), 119-131